

Thesis

Modern classification theory of
superconducting gap nodes

Shuntaro Sumita

Department of Physics, Kyoto University

December, 2019

Abstract

Classification of a superconducting gap is one of the central subjects in the research field of unconventional superconductivity. The momentum dependence of the superconducting gap is closely related to the symmetry of superconductivity and the pairing mechanism. Since the superconducting gap structure can be identified by various experiments, combined studies of the superconducting gap by theory and experiment may clarify the characteristics of superconductivity. Most of the previous studies have been based on the classification of an order parameter by the crystal point group [1–3], which was summarized by Sigrist and Ueda [4]. Although their classification has been used for analyses of excitation spectrum, it may not provide a precise result of the superconducting gap, namely excitation energy in the Bogoliubov quasiparticle spectrum. Indeed, several studies have shown that nonsymmorphic crystalline symmetry induces unconventional gap structures which are not predicted by the classification of order parameter [5–17]. That is because nonsymmorphic symmetry is neglected by the above classification method based on the point group. Furthermore, the method does not take into account electrons beyond spin-1/2, which may appear in multi-orbital or multi-sublattice superconductors.

Stimulated by the above background, we develop the classification theory of superconducting gap nodes, by using the combination of group theory and topology. Summaries of the study are shown below.

1. *Complete gap classification on high-symmetry planes* [18–20]. — In this study, mirror- or glide-symmetric superconductors are considered. By using the group-theoretical approach, we completely clarify the condition for nontrivial line nodes or gap opening on the Brillouin zone boundary, which are protected by nonsymmorphic symmetry. Next, we show that such nonsymmorphic-symmetry-characterized gap structures appear only for a primitive or orthorhombic base-centered Bravais lattice; all space groups under the additional constraint are systematically classified. As an example, we demonstrate unusual gap structures in the model of Sr_2IrO_4 . Furthermore, we unify the topology of symmetry-protected line nodes and Majorana flat bands, using the knowledge of Clifford algebra extension method.

2. *Novel j_z -dependent gap structures by classification on high-symmetry lines* [20, 21]. — Multi-degree-of-freedom superconductors with crystalline rotation symmetry have potential to provide effectively higher-spin states. In this study, we classify all crystal symmetry-protected nodes on n -fold ($n = 2, 3, 4$, and 6) axes in the Brillouin zone, by using the combination of group theory

and K theory. Especially, we elucidate gap structures depending on the total angular momentum j_z of normal Bloch states on threefold and sixfold rotational-symmetric lines. Based on the obtained results, we also discuss gap structures in various candidate superconductors.

Contents

Abstract	i
List of publications	v
1 Introduction	1
1.1 Overview of the Sigrist-Ueda classification method	2
1.2 Recent progress in superconductors with multi-degrees of freedom	6
1.3 Organization of this thesis	8
2 Method: classification theory of superconducting gap	9
2.1 Preparation	9
2.2 Group-theoretical classification of superconducting gap	12
2.3 Topological classification of superconducting gap	15
2.4 Example: space group $P2_1/m$	16
3 Superconducting gap classification on high-symmetry planes	27
3.1 Group-theoretical classification of symmetry-protected line nodes	27
3.2 Topological classification of symmetry-protected line nodes and Majorana flat bands	37
3.3 Example: Sr_2IrO_4 in $- + + -$ state	41
4 Superconducting gap classification on high-symmetry lines	51
4.1 Group-theoretical classification	51
4.2 Topological classification	52
4.3 Point nodes: UPt_3 (Space group: $P6_3/mmc$)	57
4.4 Surface nodes: SrPtAs (Space group: $P6_3/mmc$)	69
4.5 Line nodes: CeCoIn_5 (Space group: $P4/mmm$)	75
4.6 Point nodes: UCoGe (Space group: $Pnma$)	76
4.7 MoS_2 (Space group: $P6_3/mmc$)	79
4.8 UBe_{13} (Space group: $Fm\bar{3}c$)	80
4.9 $\text{PrOs}_4\text{Sb}_{12}$ (Space group: $Im\bar{3}$)	82

5 Conclusion	83
A Representation theory	85
A.1 Wigner criterion	85
A.2 Orthogonality test	87
B Other remarks	89
B.1 Sr_2IrO_4	89
B.2 Effective orbital angular momentum due to site permutation	92
Bibliography	95
Acknowledgment	107

List of publications

Papers related to the thesis

1. Shuntaro Sumita, Takuya Nomoto, and Youichi Yanase,
Multipole Superconductivity in Nonsymmorphic Sr₂IrO₄,
Physical Review Letters **119**, 027001 (2017).
© 2017 American Physical Society
2. Shingo Kobayashi, Shuntaro Sumita, Youichi Yanase, and Masatoshi Sato,
Symmetry-protected line nodes and Majorana flat bands in nodal crystalline superconductors,
Physical Review B **97**, 180504(R) (2018).
© 2018 American Physical Society
3. Shuntaro Sumita and Youichi Yanase,
Unconventional superconducting gap structure protected by space group symmetry,
Physical Review B **97**, 134512 (2018).
© 2018 American Physical Society
4. Shuntaro Sumita, Takuya Nomoto, Ken Shiozaki, and Youichi Yanase,
Classification of topological crystalline superconducting nodes on high-symmetry lines: Point nodes, line nodes, and Bogoliubov Fermi surfaces,
Physical Review B **99**, 134513 (2019).
© 2019 American Physical Society

Published papers not included in the thesis

1. Shuntaro Sumita and Youichi Yanase,
Superconductivity in magnetic multipole states,
Physical Review B **93**, 224507 (2016).
2. Jun Ishizuka, Shuntaro Sumita, Akito Daido, and Youichi Yanase,
Insulator-Metal Transition and Topological Superconductivity in UTe₂

from a First-Principles Calculation,
Physical Review Letters **123**, 217001 (2019).

Chapter 1

Introduction

In most (conventional) superconductors, superconductivity is well described within the Bardeen-Cooper-Schrieffer (BCS) theory in 1957 [22], which gives the microscopic picture of superconducting state as a condensation of bounded pairs of two electrons (Cooper pairs) on the Fermi surface (FS). The BCS theory, in a narrow sense, has three assumptions about Cooper pairs: (i) zero center-of-mass momentum, (ii) zero total spin ($S = 0$; spin-singlet), and (iii) isotropic s -wave symmetry. Then, the resulting superconducting order parameter is represented as $\Delta(\mathbf{k}) = \Delta_0 i\sigma_y$, where σ_i is the Pauli matrix in a spin space. Here, Δ_0 is a \mathbf{k} -independent constant, which means that the order parameter opens a gap over the whole FS.

On the other hand, recent studies have suggested unconventional superconductivity, which do *not* satisfy all the assumptions (i)-(iii). If the assumption (i) is broken, for example, the resulting state is called Fulde-Ferrell-Larkin-Ovchinnikov (FFLO) superconductivity [23–25], where Cooper pairs have a finite center-of-mass momentum. Other examples are (spin-singlet) anisotropic superconductivity without the assumption (iii), and spin-triplet superconductivity without (ii) and (iii) [26]. In anisotropic and spin-triplet superconductors, the order parameter has a momentum dependence (*e.g.*, p -wave and d -wave symmetry), which may indicates the presence of gapless points in the superconducting state, called *superconducting nodes*. Such momentum dependence of the superconducting gap is closely related to the symmetry of superconductivity and the pairing mechanism. Since the superconducting gap structure can be identified by various experiments [27, 28], combined studies of the superconducting gap by theory and experiment may clarify the characteristics of superconductivity.

In this context, classification of a superconducting gap is one of the central subjects in theoretical researches of unconventional superconductivity. Most of the previous studies have been based on the classification of an *order parameter* by the crystal point group [1–3], which was summarized by Sigrist and Ueda (called the Sigrist-Ueda method in this thesis) [4]. However, their classification may not provide a precise result of the superconducting *gap*, namely an excitation energy in the Bogoliubov quasiparticle spectrum. Indeed, recent studies have discovered unusual gap structures incompatible with the Sigrist-Ueda classification [5–17, 29–36].

In the following, we briefly explain the Sigrist-Ueda method, and reveal inadequacies of the classification scheme (Sec. 1.1). Then we concretely show the examples of unconventional superconducting gap structures elucidated in the recent studies (Sec. 1.2). Finally the organization of this thesis is represented in Sec. 1.3.

1.1 Overview of the Sigrist-Ueda classification method

In this section, we overview the Sigrist-Ueda classification scheme of superconducting order parameters [1–4].

1.1.1 Classification scheme

In the discussion of the section, we assume the existence of spatial inversion symmetry (IS) and time-reversal symmetry (TRS) in the normal state. Thus, the normal-state band structure has a twofold (Kramers) degeneracy for any momentum \mathbf{k} . Let us consider a BCS mean-field Hamiltonian,

$$H_{\text{BCS}} = \sum_{\mathbf{k}, s} \xi(\mathbf{k}) a_s^\dagger(\mathbf{k}) a_s(\mathbf{k}) + \frac{1}{2} \sum_{\mathbf{k}, s_1, s_2} [\Delta_{s_1 s_2}(\mathbf{k}) a_{s_1}^\dagger(\mathbf{k}) a_{s_2}^\dagger(-\mathbf{k}) + \text{H.c.}], \quad (1.1.1)$$

where $\xi(\mathbf{k})$ is the band energy measured relative to the chemical potential, and $\Delta(\mathbf{k})$ is the superconducting order parameter. Since this Hamiltonian includes no spin-orbit coupling term, the Hamiltonian has a certain symmetry represented by a group $P \times \text{SU}(2)$, where P is the point group of the crystal lattice symmetry and $\text{SU}(2)$ is the spin-rotation symmetry group.

The behavior of $\Delta(\mathbf{k})$ under a symmetry operation in $P \times \text{SU}(2)$ is determined by the invariance condition of H_{BCS} . A point group operation $p \in P$ acts only on the momentum \mathbf{k} ,

$$p a_s^\dagger(\mathbf{k}) p^{-1} = a_s^\dagger(p\mathbf{k}), \quad (1.1.2)$$

$$\Rightarrow p : \Delta_{s_1 s_2}(\mathbf{k}) \rightarrow \Delta_{s_1 s_2}(p^{-1}\mathbf{k}). \quad (1.1.3)$$

On the other hand, the spin-rotation symmetry $g \in \text{SU}(2)$ transforms the matrix space of $\Delta(\mathbf{k})$ as

$$g a_s^\dagger(\mathbf{k}) g^{-1} = \sum_{s'} a_{s'}^\dagger(\mathbf{k}) [D_{(1/2)}(g)]_{s' s}, \quad (1.1.4)$$

$$\Rightarrow g : \Delta_{s_1 s_2}(\mathbf{k}) \rightarrow [D_{(1/2)}(g) \Delta(\mathbf{k}) D_{(1/2)}(g)^T]_{s_1 s_2}, \quad (1.1.5)$$

where the 2×2 matrix $D_{(1/2)}$ is the representation of $\text{SU}(2)$ in the *pure spin-1/2* space. In the presence of spin-orbit coupling, however, the point-group transformation and the spin transformation can no longer be treated independently; the spin-rotation group $\text{SU}(2)$ is absorbed by the point group P . Although the Bloch states cannot be eigenstates of the *pure-spin* operator anymore, they can

be labeled by *pseudospin* bases; we dub the new Bloch basis as $c_\sigma^\dagger(\mathbf{k})$. Thus, the transformation property of the order parameter is changed as

$$pc_\sigma^\dagger(\mathbf{k})p^{-1} = \sum_{\sigma'} c_{\sigma'}^\dagger(p\mathbf{k})[D_{(1/2)}(g)]_{\sigma'\sigma}, \quad (1.1.6)$$

$$\Rightarrow p : \Delta_{\sigma_1\sigma_2}(\mathbf{k}) \rightarrow [D_{(1/2)}(p)\Delta(p^{-1}\mathbf{k})D_{(1/2)}(p)^T]_{\sigma_1\sigma_2}, \quad (1.1.7)$$

where $p \in P$ is a point-group operation.¹

According to Landau theory for the second-order phase transition, on one side of the transition point the crystal has the higher symmetry, while on the other side the symmetry is lower; the order parameter of the symmetry broken phase has to belong to an irreducible representation (IR) of the higher symmetry group in the other phase [37, 38]. In anisotropic superconductors, the point group symmetry P as well as the U(1) symmetry is broken below the transition temperature T_c , and thus, the order parameter belongs to an IR of P . Conversely speaking, superconducting order parameters can be classified by IRs of the point group P . In the following, we concretely see the classification method of the order parameter using the point group.

First, let us consider the limit where the spin-orbit coupling and the crystalline electric field is negligibly small. In this case, the “point group” is represented by the rotation group: $P = \text{SO}(3) \times \mathcal{I}$ with the inversion symmetry \mathcal{I} . Therefore, the superconducting order parameter is represented in the function space $D_{(l)} \times D_{(S)}$, where $D_{(l)}$ denotes the \mathbf{k} -space representation and $D_{(S)}$ the spin-space representation of P .² As a concrete representation, the order parameter is given by the spherical harmonics $Y_{lm}(\mathbf{k})$ for $D_{(l)}$, and the spin functions $\chi_s(0, 0) = 1$ for $D_{(S=0)}$ and

$$\chi_t(1, s_z) = \begin{cases} \hat{x} + i\hat{y} & s_z = -1 \\ \sqrt{2}\hat{z} & s_z = 0 \\ -\hat{x} + i\hat{y} & s_z = +1 \end{cases} \quad (1.1.8)$$

for $D_{(S=1)}$ space. That is,

$$\Delta_l(\mathbf{k}) = \begin{cases} \sum_m c_m Y_{lm}(\hat{\mathbf{k}})i\sigma_y & \text{singlet; } l = \text{even,} \\ \sum_{m,\hat{\mathbf{n}}} c_{m\hat{\mathbf{n}}} Y_{lm}(\hat{\mathbf{k}})(\boldsymbol{\sigma} \cdot \hat{\mathbf{n}})i\sigma_y & \text{triplet; } l = \text{odd,} \end{cases} \quad (1.1.9)$$

where c_m and $c_{m\hat{\mathbf{n}}}$ are complex numbers.

If we introduce spin-orbit coupling, these function spaces split into subspaces due to the symmetry lowering. In order to obtain the new classification spaces, we have to decompose the Kronecker

¹Since the spatial inversion $\mathcal{I} \in P$ is not an element of $\text{SU}(2)$, we define $D_{(1/2)}(\mathcal{I})$ as the identity matrix σ_0 .

²The indices $l = 0, 1, 2, \dots$ and $S = 0, 1$ are relative angular momentum and total spin angular momentum, respectively.

Table 1.1: Classification of superconducting order parameters by even-parity basis functions $\Delta_{\Gamma_i}(\mathbf{k}) = \psi_{\Gamma_i}(\mathbf{k})i\sigma_y$ and odd-parity basis functions $\Delta_{\Gamma_i}(\mathbf{k}) = \mathbf{d}_{\Gamma_i}(\mathbf{k}) \cdot \boldsymbol{\sigma}i\sigma_y$ for the tetragonal D_{4h} group [4].

IR (even)	Basis functions	IR (odd)	Basis functions
A_{1g}	$\psi(\mathbf{k}) = 1, k_x^2 + k_y^2, k_z^2$	A_{1u}	$\mathbf{d}(\mathbf{k}) = k_x\hat{x} + k_y\hat{y}, k_z\hat{z}$
A_{2g}	$\psi(\mathbf{k}) = k_xk_y(k_x^2 - k_y^2)$	A_{2u}	$\mathbf{d}(\mathbf{k}) = k_y\hat{x} - k_x\hat{y}$
B_{1g}	$\psi(\mathbf{k}) = k_x^2 - k_y^2$	B_{1u}	$\mathbf{d}(\mathbf{k}) = k_x\hat{x} - k_y\hat{y}$
B_{2g}	$\psi(\mathbf{k}) = k_xk_y$	B_{2u}	$\mathbf{d}(\mathbf{k}) = k_y\hat{x} + k_x\hat{y}$
E_g	$\psi_1(\mathbf{k}) = k_xk_z$ $\psi_2(\mathbf{k}) = k_yk_z$	E_u	$\mathbf{d}_1(\mathbf{k}) = k_z\hat{x}, k_x\hat{z}$ $\mathbf{d}_2(\mathbf{k}) = k_z\hat{y}, k_y\hat{z}$

product of \mathbf{k} - and spin-space,

$$\begin{cases} D_{(l)} \times D_{(S=0)} = D_{(l)} & \text{singlet; } l = \text{even,} \\ D_{(l)} \times D_{(S=1)} = D_{(l-1)} + D_{(l)} + D_{(l+1)} & \text{triplet; } l = \text{odd.} \end{cases} \quad (1.1.10)$$

The basis functions of the new representations can be derived by the Clebsch-Gordan formalism, which can be labeled by the total angular momentum J .

Now we turn the crystalline electric field on. The crystal symmetry is lowered from a continuous rotation group $\text{SO}(3) \times \mathcal{I}$ with an infinite number of IRs to a discrete point group with only a few IRs. Thus, we can classify the basis functions of the order parameters, by considering projections of the functions belonging to $D_{(J)}$ (with small J) on the IRs Γ of the crystal point group P . For example, Table 1.1 shows the classification results for $P = D_{4h}$ summarized in Ref. [4]. From the table, the $d_{x^2-y^2}$ -wave order parameter is found to belong to the B_{1g} IR of D_{4h} , which guarantees the presence of line nodes on the symmetry planes $k_x \pm k_y = 0$. Such a gap structure is proposed in cuprates [26] and CeCoIn₅ [26, 39, 40].

1.1.2 Inadequacies of the Sigrist-Ueda method

In the previous section, we see the classification scheme of the Sigrist-Ueda method, which is useful for symmetry analysis of superconducting order parameters. Indeed, the classification tables for the basic point groups O_h , D_{6h} , and D_{4h} in Ref. [4] have been used to unveil the fundamental properties of various unconventional superconductivity. However, recent studies have elucidated that the results of the Sigrist-Ueda method may not be precise for actual superconducting gap structures [5–17, 29–36]. In the following, we refer to three related problems of the method.

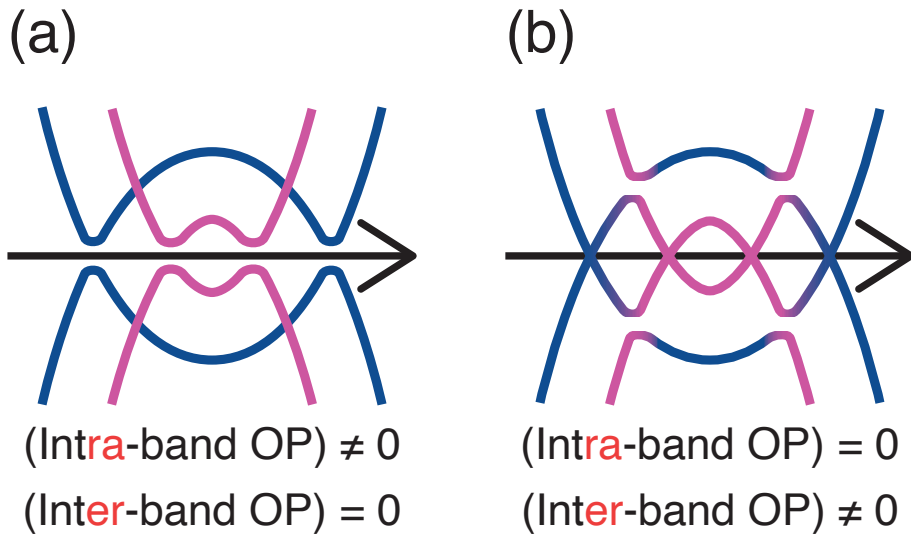


Figure 1.1: Schematic picture of two-band (four-band in the particle-hole space) superconductivity. Each figure shows the Bogoliubov quasiparticle spectrum for (a) finite *intra*-band and zero *inter*-band order parameters, and (b) zero *intra*-band and finite *inter*-band order parameters.

1.1.2.1 Incompatibility between order parameter and gap structure

First problem is that the order parameter obtained by the method does not appropriately indicate the superconducting gap structure. For example, let us consider two-band superconductivity depicted in Fig. 1.1. Figure 1.1(a) shows the situation where the *intra*-band order parameter is finite, while the *inter*-band order parameter is zero. In this case, the amplitude of the order parameter corresponds to the size of the superconducting gap (an excitation energy in the Bogoliubov spectrum). In Fig. 1.1(b), on the other hand, the situation is inverted; the *intra*-band (*inter*-band) order parameter is zero (finite). If the band splitting is sufficiently larger than the inter-band order parameter, the superconducting gap is zero in spite of the finite order parameter. This is a simple example of the incompatibility between an order parameter and a gap structure. From the above reason, our new classification method focuses only on *intra*-band order parameters (Chapter 2).

1.1.2.2 Absence of space group symmetry analysis

Secondly, the space group symmetry is not taken into account in the method. Since a space group is given by the combination of a point group and a translation group, it provides us with more information than the point group. Now we point out the importance of considering *nonsymmorphic* space group symmetry, by showing an example.

In 1985, Blount showed that no symmetry-protected line node exists in odd-parity superconductors [41], which is consistent with the result of the Sigrist-Ueda method. After that, however, some studies showed a counter-example, namely, a line node in nonsymmorphic systems, and indeed

suggested a line node protected by a nonsymmorphic space group symmetry in UPt₃ [6, 11–15]. At present, it is known that Blount’s theorem holds only in symmorphic crystals. The essence is that the nonsymmorphic symmetry causes the difference in the group-theoretical representation of gap functions between the basal planes (BPs) and the zone faces (ZFs) in the Brillouin zone (BZ). Although the Sigrist-Ueda method, which takes only point group symmetry into account, appropriately implies the gap functions on the BPs, it may fail to show those on the ZFs.

1.1.2.3 Absence of higher-spin state analysis

Third issue is that the Sigrist-Ueda method considers only spin-1/2 states. In multi-orbital and multi-sublattice superconductors, however, a band basis often acquires total angular momentum larger than 1/2. Such higher-pseudospin (3/2, 5/2, . . .) states may affect the resulting superconducting gap structures. Indeed, recent theoretical studies have suggested novel type of superconducting order parameters in higher-spin states [29–36].

1.2 Recent progress in superconductors with multi-degrees of freedom

In this section, we introduce recent develop beyond the results of the Sigrist-Ueda classification in the previous section. The unconventional results basically emerge in superconductors with multi-degrees of freedom, such as multi-sublattice (Sec. 1.2.1) and multi-orbital superconductors (Sec. 1.2.2).

1.2.1 Nonsymmorphic multi-sublattice superconductors

As mentioned in Sec. 1.1.2, recent theoretical studies have pointed out that the odd-parity superconductor UPt₃ possesses line nodes characterized by nonsymmorphic symmetry [6, 11–15], which was not predicted by the Sigrist-Ueda method. After that, nonsymmorphic-symmetry-protected nodes have been suggested in other superconductors: UCoGe [16], URhGe [16], UPd₂Al₃ [16, 17, 42], UNi₂Al₃ [17], and CrAs [17]. In these superconductors, nonsymmorphic symmetry (namely screw or glide symmetry) ensures that the crystal structure includes more than one sublattice. Such sublattice degree of freedom often play essential roles on the nodal structure.

In order to see the importance of sublattice degree of freedom, we consider an example of a one-dimensional (1D) zigzag chain with two sublattice *a* and *b*, depicted in Fig. 1.2. The system has nonsymmorphic screw symmetry $\{C_{2z}|\hat{\frac{z}{2}}\}$,³ which transfers each *a* atom to the *b* atom at the neighboring unit cell (the green arrow in Fig. 1.2). The transformation of $g = \{C_{2z}|\hat{\frac{z}{2}}\}$ is represented

³The notation $g = \{p_g|t_g\}$ is a conventional Seitz space group symbol with a point-group operation p_g and a translation t_g .

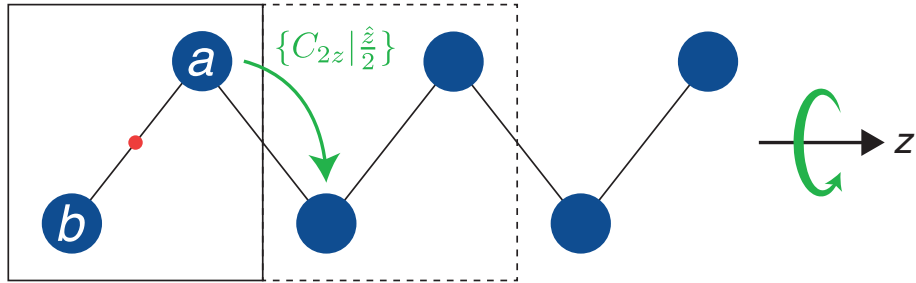


Figure 1.2: A 1D zigzag chain with two sublattice a and b . The black rectangle and the red point represents the unit cell and the inversion center, respectively. Due to screw symmetry $\{C_{2z}|\frac{\hat{z}}{2}\}$, each a atom is transferred to the b atom at the neighboring unit cell (green arrow).

as follows:

$$\begin{aligned} g c_{a\sigma}^\dagger(k_z) g^{-1} &= e^{-ik_z/2} \sum_{\sigma'} c_{b\sigma'}^\dagger(C_{2z}k_z)[D_{(1/2)}(g)]_{\sigma'\sigma} \\ &= \sum_{m'\sigma'} c_{m'\sigma'}^\dagger(k_z)[D_{(\text{perm})}(g; k_z)]_{m'm}[D_{(1/2)}(g)]_{\sigma'\sigma}. \end{aligned} \quad (1.2.1)$$

where $c_{m\sigma}^\dagger(k_z)$ ($m = a, b$) is a creation operator for sublattice m and pseudospin σ . Comparing Eq. (1.2.1) with Eq. (1.1.6), there newly appears $[D_{(\text{perm})}(g; k_z)]_{m'm} = e^{-ik_z/2}\delta_{m',gm}$, which is a representation matrix describing the interchange of the two sites.⁴ The momentum (k_z) dependence of the matrix, which is a consequence of nonsymmorphic symmetry, has a crucial role in the classification of superconducting gap functions. However, few works have investigated gap structures for *general* nonsymmorphic symmetries as well as some representative superconductors [15, 17].

1.2.2 Multi-orbital superconductors

The Sigrist-Ueda method performs classification of the superconducting order parameter based on the band-based representation, where the normal Bloch states are assumed to possess spin-1/2 degrees of freedom. Although the classification scheme is always possible, the electrons have other internal degrees of freedom such as orbital and sublattice, which cannot be neglected in real superconductors. Indeed, we have shown that sublattice degree of freedom affects the gap structure in the previous subsection. Now let us consider the effect of orbital degree of freedom on the transformation property of gap functions.

In multi-orbital superconductors, the normal Bloch states have a local orbital as well as (pseudo)spin-1/2 degrees of freedom. Here, we suppose a real atomic orbital with angular momentum L . Then, the normal Bloch basis is represented by the creation operator $c_{l\sigma}^{(L)\dagger}(\mathbf{k})$ with the

⁴Note that $c_{m\sigma}^\dagger(k_z)$ in Eq. (1.2.1) is defined by the sublattice-dependent Fourier transformation, while the sublattice-independent one is used in the discussion of Appendix B.2.

orbital (l) and the pseudospin (σ) bases, which transforms as

$$pc_{l\sigma}^{(L)\dagger}(\mathbf{k})p^{-1} = \sum_{l'\sigma'} c_{l'\sigma'}^{(L)\dagger}(p\mathbf{k})[D_{(L)}(p)]_{l'l}[D_{(1/2)}(p)]_{\sigma'\sigma}, \quad (1.2.2)$$

for a point-group operation $p \in P$. Here, $D_{(L)}(p)$ is a representation matrix describing the transformation among the orbital bases with angular momentum L , which makes a difference from Eq. (1.1.6). The product of $D_{(L)} \times D_{(1/2)}$ generates the Bloch states with higher total angular momentum than $1/2$, which play crucial roles on the superconducting gap structures. Indeed, the recent classification theory of order parameter in multi-orbital superconductors [29, 43] has suggested the nontrivial \mathbf{k} dependence of the gap function. For example, multi-orbital *even-parity* superconductors can possess *spin-triplet* (and orbital-triplet) order parameter, which is forbidden in single-orbital even-parity superconductors.

Furthermore, recent theoretical studies have investigated the pairing of Bloch states with $j = 3/2$ total angular momentum [30–36]. The theories have shown that $j = 3/2$ fermions permit Cooper pairs with quintet or septet total angular momentum, in addition to the usual singlet and triplet states. Also, a new type of nodal structure is founded to appear in the $j = 3/2$ system; in TRS breaking even-parity superconductors, the conventional nodal structure (a point or a line node) is “inflated,” which means the appearance of a surface node [31, 32]. They called it a *Bogoliubov FS* and elucidated that the Bogoliubov FS is characterized by a zero-dimensional (0D) \mathbb{Z}_2 topological number.

1.3 Organization of this thesis

In this thesis, we offer a comprehensive classification theory of superconducting gap nodes beyond the Sigrist-Ueda method [4] in various superconductors with spin-orbit coupling and multi-degrees of freedom. In Chapter 2, the modern classification method of superconducting gap, which makes use of the combination of group theory and topology, is introduced. Using the method, we systematically classify gap structures on high-symmetry regions in the BZ: mirror-invariant planes (Chapter 3) and rotation-invariant axes (Chapter 4). In Chapter 3, general conditions for nontrivial nonsymmorphic-symmetry-protected gap structures are shown from both aspects of finite-group representation theory [20] and topology [19]. As an example, such unusual gap structures are demonstrated in the model of Sr_2IrO_4 [18]. In Chapter 4, on the other hand, the classification results on rotational axes show that unconventional nodal structures appear even in symmorphic superconductors. We emphasize that higher-spin $3/2$ states affect the superconducting gap structures; the gap classification depends on the total angular momentum $j_z = 1/2, 3/2, \dots$ of normal Bloch states on threefold and sixfold rotational-symmetric lines [20, 21]. Such j_z -dependent gap structures are also discussed in various candidate superconductors. Especially, we elucidate the presence of perfectly spin-polarized nonunitary superconductivity in UPt_3 [21].

Chapter 2

Method: classification theory of superconducting gap

In this Chapter, we introduce modern gap classification theory using group theory (representation theory) and topological argument. First, in Sec. 2.1, we make a remark about some terminologies and notations of finite-group representation theory, which are used throughout the thesis, for the avoidance of confusion. In Sec. 2.2, we introduce the group-theoretical analysis of the superconducting gap on high-symmetry points in the BZ [5, 7–11, 15–18, 20]. Next, we explain the topological classification of nodes on the high-symmetry points by using the Wigner criteria and the orthogonality test in Sec. 2.3 [21]. Also, an intuitive understanding of the classification methods is given by showing simple examples (Sec. 2.4).

2.1 Preparation

In this section, we define some terminologies and notations which are commonly used in the group-theoretical classification (Sec. 2.2) and the topological classification (Sec. 2.3). In all the discussions below, we assume *centrosymmetric* superconductors,¹ which have the IS $\mathcal{I} = \{I|\mathbf{0}\}$. Also, *paramagnetic* (PM) and *antiferromagnetic* (AFM) superconductors have the TRS $\mathcal{T} = \{T|t_{\mathcal{T}}\}$, while *ferromagnetic* (FM) ones possess no TRS. Note that $t_{\mathcal{T}}$ represents a non-primitive translation for AFM superconductors, while it is zero for PM superconductors.

First, we focus on a magnetic space group M ; suppose that G is a unitary space group including IS, M is equal to $G + \mathcal{T}G$ for PM and AFM, and is G for FM superconductors. In order to classify the gap structure on high-symmetry \mathbf{k} -points (mirror planes and rotation axes) in the BZ, we restrict G (M) to $\mathcal{G}^{\mathbf{k}} \subset G$ ($\mathcal{M}^{\mathbf{k}} \subset M$), which is the (magnetic) little group leaving \mathbf{k} points on the axes invariant modulo a reciprocal lattice vector. Thus the factor group of the (magnetic) little group by

¹Indeed, our topological classification theory (Sec. 2.3) can also be applied to other cases, *e.g.*, noncentrosymmetric superconductors.

the translation group \mathcal{G}^k/\mathbb{T} (\mathcal{M}^k/\mathbb{T}) is called the (magnetic) little cogroup. The (magnetic) little cogroup is isomorphic to the corresponding (magnetic) point group; $\bar{\mathcal{G}}^k = C_s$ ($\bar{\mathcal{M}}^k = C_s + \mathcal{T}\mathcal{I}C_s$) for mirror planes, and $\bar{\mathcal{G}}^k = C_n$ or C_{nv} ($\bar{\mathcal{M}}^k = C_n + \mathcal{T}\mathcal{I}C_n$ or $C_{nv} + \mathcal{T}\mathcal{I}C_{nv}$) for n -fold rotational axes ($n = 2, 3, 4$, and 6).

Here, we define $\lambda_\alpha^k(m)$ as a double-valued small corepresentation of symmetry operations $m \in \mathcal{M}^k$, which represents the normal Bloch state with the crystal momentum \mathbf{k} :

$$mc_{\alpha i}^\dagger(\mathbf{k})m^{-1} = \sum_i c_{\alpha j}^\dagger(\mathbf{k})[\lambda_\alpha^k(m)]_{ji}. \quad (2.1.1)$$

α is the label of the double-valued IR, which corresponds to the total angular momentum of the Bloch state $j_z = \pm 1/2, \pm 3/2, \dots$ in spin-orbit coupled systems.² Since \mathcal{M}^k is the semi-direct product between the magnetic little cogroup $\bar{\mathcal{M}}^k$ and the translation group \mathbb{T} , the small corepresentation satisfies the following equation for the translation subgroup $\mathbb{T} \subset \mathcal{M}^k$:

$$\lambda_\alpha^k(T_R) = e^{-i\mathbf{k} \cdot T_R}, \quad (2.1.2)$$

where $T_R \in \mathbb{T}$. Furthermore, λ_α^k has a factor system $\{\omega_{\text{in}}(l_1, l_2)\} \in H^2(M, \text{U}(1)_\phi)$, which arises from internal degrees of freedom (e.g. a half-integer spin of electrons):

$$\omega_{\text{in}}(m_1, m_2)\lambda_\alpha^k(m_1 m_2) = \begin{cases} \lambda_\alpha^k(m_1)\lambda_\alpha^k(m_2) & \phi(m_1) = 1, \\ \lambda_\alpha^k(m_1)\lambda_\alpha^k(m_2)^* & \phi(m_1) = -1, \end{cases} \quad (2.1.3)$$

where $\phi : \mathcal{M} \rightarrow \mathbb{Z}_2 = \{\pm 1\}$ is an indicator for unitary/antiunitary symmetry. Next, we consider a more general element $l \in M$. The sewing matrix u_α^k on M , corresponding to λ_α^k , can be defined by

$$lc_{\alpha i}^\dagger(\mathbf{k})l^{-1} = \sum_i c_{\alpha j}^\dagger(l\mathbf{k})[u_\alpha^k(l)]_{ji}, \quad (2.1.4)$$

where we note that the momentum $l\mathbf{k}$ is not equivalent to \mathbf{k} for a general $l \in M$. u_α^k also satisfies the following equation:

$$\omega_{\text{in}}(l_1, l_2)u_\alpha^k(l_1 l_2) = \begin{cases} u_\alpha^{l_2 k}(l_1)u_\alpha^k(l_2) & \phi(l_1) = 1, \\ u_\alpha^{l_2 k}(l_1)u_\alpha^k(l_2)^* & \phi(l_1) = -1. \end{cases} \quad (2.1.5)$$

Especially, $u_\alpha^k(m) = \lambda_\alpha^k(m)$ for $m \in \mathcal{M}^k$. The factor system satisfies the following 2-cocycle condition,

$$\omega_{\text{in}}(l_1, l_2)\omega_{\text{in}}(l_1 l_2, l_3) = \omega_{\text{in}}(l_1, l_2 l_3)\omega_{\text{in}}(l_2, l_3)^{\phi(l_1)}, \quad (2.1.6)$$

²Strictly speaking, α is a double-valued IR of the finite group $\bar{\mathcal{M}}^k = \mathcal{M}^k/\mathbb{T}$ while j_z is a basis of the continuous group. Therefore there is no one-to-one correspondence between α and j_z in some cases. In the C_{2v} symmetry, for example, the IR $\alpha = 1/2$ includes all normal Bloch states with half-integer total angular momentum $j_z = \pm 1/2, \pm 3/2, \pm 5/2, \dots$. In this thesis, however, we represent j_z with minimum absolute value, which satisfies $j_z \downarrow \bar{\mathcal{M}}^k = \alpha$, as the angular-momentum counterpart of the IR α .

which is easily derived from the associativity of product of representation matrices.

For easy treatment of the sewing matrix u_α^k (and the small corepresentation λ_α^k), it is useful to consider the finite factor group M/\mathbb{T} . Then, the corresponding sewing matrix \bar{u}_α^k on M/\mathbb{T} is introduced by

$$u_\alpha^k(l) = e^{-il\mathbf{k}\cdot\tau_l} \bar{u}_\alpha^k(\bar{l}), \quad (2.1.7)$$

where \bar{l} is the representative in M/\mathbb{T} for $l \in M$, and

$$\tau_l = \mathbf{t}_l - \mathbf{t}_{\bar{l}}, \quad (2.1.8)$$

is the Bravais lattice translation in \mathbb{T} corresponding to l . Substituting (2.1.7) into (2.1.5),

$$\omega_{\text{in}}(l_1, l_2) e^{-il_1 l_2 \mathbf{k}\cdot\mathbf{v}(l_1, l_2)} \bar{u}_\alpha^k(\bar{l}_1 \bar{l}_2) = \begin{cases} \bar{u}_\alpha^{l_2 k}(\bar{l}_1) \bar{u}_\alpha^k(\bar{l}_2) & \phi(l_1) = 1, \\ \bar{u}_\alpha^{l_2 k}(\bar{l}_1) \bar{u}_\alpha^k(\bar{l}_2)^* & \phi(l_1) = -1, \end{cases} \quad (2.1.9)$$

$$\mathbf{v}(l_1, l_2) = \tau_{l_1 l_2} - \tau_{l_1} - p_{l_1} \tau_{l_2} = -[\mathbf{t}_{\bar{l}_1 \bar{l}_2} - \mathbf{t}_{\bar{l}_1} - p_{l_1} \mathbf{t}_{\bar{l}_2}]. \quad (2.1.10)$$

In Eq. (2.1.9), the nonsymmorphic part of the factor system³ is described by a Bravais lattice translation $\mathbf{v}(l_1, l_2)$, namely

$$\omega_{\text{ns}}^k(l_1, l_2) = e^{-ik\cdot\mathbf{v}(l_1, l_2)}, \quad (2.1.11)$$

which depends only on the corresponding representatives: $\omega_{\text{ns}}^k(l_1, l_2) = \omega_{\text{ns}}^k(\bar{l}_1, \bar{l}_2)$. Especially, the IR $\bar{\lambda}_\alpha^k$ of magnetic little cogroup $\bar{\mathcal{M}}^k = \mathcal{M}^k/\mathbb{T}$, which corresponds to the small corepresentation λ_α^k , satisfies the following equations:

$$\lambda_\alpha^k(m) = e^{-ik\cdot\tau_m} \bar{\lambda}_\alpha^k(\bar{m}), \quad (2.1.12)$$

$$\omega_{\text{in}}(m_1, m_2) \omega_{\text{ns}}^k(m_1, m_2) \bar{\lambda}_\alpha^k(\bar{m}_1 \bar{m}_2) = \begin{cases} \bar{\lambda}_\alpha^k(\bar{m}_1) \bar{\lambda}_\alpha^k(\bar{m}_2) & \phi(m_1) = 1, \\ \bar{\lambda}_\alpha^k(\bar{m}_1) \bar{\lambda}_\alpha^k(\bar{m}_2)^* & \phi(m_1) = -1, \end{cases} \quad (2.1.13)$$

where \bar{m} is the representative in $\bar{\mathcal{M}}^k$ for $m \in \mathcal{M}^k$.

$\bar{\lambda}_\alpha^k$ is constructed from the projective IR $\bar{\gamma}_\alpha^k$ of the (unitary) little cogroup $\bar{\mathcal{G}}^k$ with the appropriate factor system $\{\omega^k(l_1, l_2) = \omega_{\text{in}}(l_1, l_2) \omega_{\text{ns}}^k(l_1, l_2)\}$ [44, 45], by using the Wigner criterion (Herring test) [38, 45–48]:

$$W_\alpha^{\mathfrak{T}} \equiv \frac{1}{|\bar{\mathcal{G}}^k|} \sum_{\bar{g} \in \bar{\mathcal{G}}^k} \omega^k(\mathfrak{T}\bar{g}, \mathfrak{T}\bar{g}) \chi[\bar{\gamma}_\alpha^k(\overline{(\mathfrak{T}g)^2})] = \begin{cases} 1 & (\text{a}), \\ -1 & (\text{b}), \\ 0 & (\text{c}), \end{cases} \quad (2.1.14)$$

³The factor system also satisfies the 2-cocycle condition:

$$\omega_{\text{ns}}^{l_1 l_2 l_3 k}(l_1, l_2) \omega_{\text{ns}}^{l_1 l_2 l_3 k}(l_1 l_2, l_3) = \omega_{\text{ns}}^{l_1 l_2 l_3 k}(l_1, l_2 l_3) \omega_{\text{ns}}^{l_2 l_3 k}(l_2, l_3)^{\phi(l_1)}.$$

Table 2.1: Notations of some intriguing groups and representations. The terminologies in the first column are associated with an unitary group, while those in the third column are with a nonunitary group including antiunitary operators. In the table, we adopt the terminologies of Ref. [45].

Terminology	Notation	Terminology	Notation	Definition
Space group	G	Magnetic space group	M	Whole crystal symmetry of the system
Little group	\mathcal{G}^k	Magnetic little group	\mathcal{M}^k	Stabilizer of k
Small representation	γ_a^k	Small corepresentation	λ_a^k	IR of (magnetic) little group
Little cogroup	$\bar{\mathcal{G}}^k$	Magnetic little cogroup	$\bar{\mathcal{M}}^k$	Factor group of (magnetic) little group by \mathbb{T}
N/A	$\tilde{\gamma}_a^k$	N/A	$\tilde{\lambda}_a^k$	IR of (magnetic) little cogroup

where χ is the character of the representation, $\mathfrak{T} \equiv \mathcal{T}\mathcal{I}$ is a TRS-like operator preserving k . In the (b) and (c) cases, the degeneracy of $\tilde{\lambda}_a^k$ is twice as much as that of $\tilde{\gamma}_a^k$, while $\tilde{\lambda}_a^k(\bar{g})$ gives the same representation as $\tilde{\gamma}_a^k(\bar{g})$ for $\bar{g} \in \bar{\mathcal{G}}^k$ in the (a) case (for details, see Appendix A.1). In the above discussion, we have introduced a lot of notations for groups and representations. For the avoidance of confusion, we summarize the intriguing notations in Table 2.1, and show a simple example in the next section.

2.2 Group-theoretical classification of superconducting gap

In this section, we introduce the group-theoretical classification of the superconducting gap on high-symmetry points in the BZ [5, 7–11, 15–17].

2.2.1 Classification theory

As seen in Sec. 2.1, we can obtain the magnetic small representation λ_a^k corresponding to the normal Bloch state on a high-symmetry k point. In the superconducting state, zero center-of-mass momentum Cooper pairs have to be formed between degenerate states present at k and $-k$ in the same band when we adopt the weak-coupling BCS theory. Then, the two states should be connected by IS \mathcal{I} and/or TRS \mathcal{T} , except for an accidentally degenerate case. As a result, the representation P_a^k of the Cooper-pair wave function can be constructed from the representations of the Bloch state λ_a^k .

Next, we calculate the single-valued representation P_a^k of the Cooper-pair wave function. Taking into account the antisymmetry of the Cooper pairs and the degeneracy of the two states, we can regard P_a^k as an antisymmetrized Kronecker square [45, 49], with zero total momentum, of the induced representation $\lambda_a^k \uparrow \mathcal{M}_{\text{pair}}^k$. Here, $\mathcal{M}_{\text{pair}}^k \equiv \mathcal{M}^k + \mathcal{I}\mathcal{M}^k$ is the group to which the representation P_a^k of the pair wave function belongs. This is given by $P_a^k(m) = \bar{P}_a^k(\bar{m})$, where $m = \bar{m}t$ for $m \in \mathcal{M}_{\text{pair}}^k$, $\bar{m} \in \bar{\mathcal{M}}_{\text{pair}}^k \equiv \mathcal{M}_{\text{pair}}^k/\mathbb{T}$, and $t \in \mathbb{T}$. \bar{P}_a^k , which is the representation of $\bar{\mathcal{M}}_{\text{pair}}^k$, is obtained in a systematic way by using the double coset decomposition and the corresponding Mackey-Bradley

theorem [45, 49, 50],

$$\chi[\bar{P}_\alpha^k(\bar{g})] = \frac{\omega^k(\mathcal{I}, \bar{g})}{\omega^k(\bar{g}, \mathcal{I})} \chi[\bar{\lambda}_\alpha^k(\bar{g})]^2, \quad (2.2.1a)$$

$$\chi[\bar{P}_\alpha^k(\mathcal{I}\bar{g})] = -\frac{\omega^k(\mathcal{I}, \bar{g})\omega^k(\bar{g}, \bar{g})}{\omega^k(\bar{g}, \mathcal{I})} \chi[\bar{\lambda}_\alpha^k(\bar{g}^2)], \quad (2.2.1b)$$

where $\bar{g} \in \bar{\mathcal{G}}^k$. A proof of the Mackey-Bradley theorem in the context of Cooper pair wave functions is shown in Sec. 2.2.2.

Finally, we reduce \bar{P}_α^k into single-valued IRs of the point group $\bar{\mathcal{M}}_{\text{pair}}^k$. The gap functions should be zero, and thus, the gap nodes appear, if the corresponding IRs do not exist in the results of reductions [5, 7, 51]. Otherwise, the superconducting gap will open in general. Therefore the representation \bar{P}_α^k of pair wave function tells us the presence or absence of superconducting gap nodes.

2.2.2 Proof of Mackey-Bradley theorem in the context of Cooper pair wave function

We prove here the Mackey-Bradley theorem [45, 49, 50] described by Eq. (2.2.1) by considering the symmetry transformation of the Cooper pair wave function. First, we introduce a creation operator of a Bloch state in a band-based representation denoted by $c_{\alpha i}^\dagger(\mathbf{k})$, where α and i are the IR of the little cogroup $\bar{\mathcal{M}}^k$ and its basis, respectively. This operator is transformed as

$$\bar{m}c_{\alpha i}^\dagger(\mathbf{k})\bar{m}^{-1} = \sum_{i'} c_{\alpha i'}^\dagger(\mathbf{k})[\bar{\lambda}_\alpha^k(\bar{m})]_{i'i}, \quad (2.2.2)$$

by a space group operation $\bar{m} \in \bar{\mathcal{M}}^k$, where $\bar{\lambda}_\alpha^k$ is the representation matrix of the small representation α . Then, we define the Cooper pair wave function

$$[\Delta_\alpha(\mathbf{k})]_{ij} \equiv c_{\alpha i}^\dagger(\mathbf{k}) \cdot \mathcal{I} c_{\alpha j}^\dagger(\mathbf{k}) \mathcal{I}, \quad (2.2.3)$$

which is assumed to form a pair between two Bloch states belonging to the same IR α . Using Eq. (2.2.2), the Cooper pair wave function is transformed by $\bar{g} \in \bar{\mathcal{G}}^k$ as follows⁴:

$$\begin{aligned} \bar{g}[\Delta_\alpha(\mathbf{k})]_{ij}\bar{g}^{-1} &= \bar{g}c_{\alpha i}^\dagger(\mathbf{k})\bar{g}^{-1} \cdot \mathcal{I}(\mathcal{I}\bar{g}\mathcal{I})c_{\alpha j}^\dagger(\mathbf{k})(\mathcal{I}\bar{g}\mathcal{I})^{-1}\mathcal{I} \\ &= \sum_{i'} c_{\alpha i'}^\dagger(\mathbf{k})[\bar{\lambda}_\alpha^k(\bar{g})]_{i'i} \cdot \mathcal{I} \left\{ \frac{\omega^k(\mathcal{I}, \bar{g})}{\omega^k(\bar{g}, \mathcal{I})} \sum_{j'} c_{\alpha j'}^\dagger(\mathbf{k})[\bar{\lambda}_\alpha^k(\bar{g})]_{j'j} \right\} \mathcal{I} \end{aligned}$$

⁴Here,

$$\begin{aligned} (\mathcal{I}\bar{g}\mathcal{I})c_{\alpha j}^\dagger(\mathbf{k})(\mathcal{I}\bar{g}\mathcal{I})^{-1} &= \sum_{j_1} (\mathcal{I}\bar{g})c_{\alpha j_1}^\dagger(\mathcal{I}\mathbf{k})(\mathcal{I}\bar{g})^{-1}[\bar{u}_\alpha^k(\mathcal{I})]_{j_1 j} \\ &= \sum_{j_1, j_2} \mathcal{I}c_{\alpha j_2}^\dagger(\bar{g}\mathcal{I}\mathbf{k})\mathcal{I}^{-1}[\bar{u}_\alpha^{I\mathbf{k}}(\bar{g})]_{j_2 j_1}[\bar{u}_\alpha^k(\mathcal{I})]_{j_1 j} \\ &= \sum_{j_1, j_2, j_3} c_{\alpha j_3}^\dagger(\mathcal{I}\bar{g}\mathcal{I}\mathbf{k})[\bar{u}_\alpha^{\bar{g}I\mathbf{k}}(\mathcal{I})]_{j_3 j_2}[\bar{u}_\alpha^{I\mathbf{k}}(\bar{g})]_{j_2 j_1}[\bar{u}_\alpha^k(\mathcal{I})]_{j_1 j} \end{aligned}$$

$$\begin{aligned}
&= \sum_{i',j'} \{c_{\alpha i'}^\dagger(\mathbf{k}) \cdot \mathcal{I} c_{\alpha j'}^\dagger(\mathbf{k}) \mathcal{I}\} \frac{\omega^k(\mathcal{I}, \bar{g})}{\omega^k(\bar{g}, \mathcal{I})} [\bar{\lambda}_\alpha^k(\bar{g})]_{i'i} [\bar{\lambda}_\alpha^k(\bar{g})]_{j'j} \\
&= \sum_{i',j'} [\Delta_\alpha(\mathbf{k})]_{i'j'} \frac{\omega^k(\mathcal{I}, \bar{g})}{\omega^k(\bar{g}, \mathcal{I})} [\bar{\lambda}_\alpha^k(\bar{g})]_{i'i} [\bar{\lambda}_\alpha^k(\bar{g})]_{j'j}.
\end{aligned} \tag{2.2.4}$$

On the other hand, $\Delta_{ij}^\alpha(\mathbf{k})$ is transformed by $\mathcal{I}\bar{g} \in \mathcal{I}\bar{\mathcal{G}}^k$ as

$$\begin{aligned}
(\mathcal{I}\bar{g})[\Delta_\alpha(\mathbf{k})]_{ij}(\mathcal{I}\bar{g})^{-1} &= -(\mathcal{I}\bar{g})\mathcal{I}c_{\alpha j}^\dagger(\mathbf{k})\mathcal{I} \cdot c_{\alpha i}^\dagger(\mathbf{k})(\mathcal{I}\bar{g})^{-1} \\
&= -(\mathcal{I}\bar{g}\mathcal{I})c_{\alpha j}^\dagger(\mathbf{k})(\mathcal{I}\bar{g}\mathcal{I})^{-1} \cdot \mathcal{I}\{\bar{g}c_{\alpha i}^\dagger(\mathbf{k})\bar{g}^{-1}\}\mathcal{I} \\
&= -\sum_{i',j'} \{c_{\alpha i'}^\dagger(\mathbf{k}) \cdot \mathcal{I} c_{\alpha j'}^\dagger(\mathbf{k}) \mathcal{I}\} \frac{\omega^k(\mathcal{I}, \bar{g})}{\omega^k(\bar{g}, \mathcal{I})} [\bar{\lambda}_\alpha^k(\bar{g})]_{i'j} [\bar{\lambda}_\alpha^k(\bar{g})]_{j'i} \\
&= -\sum_{i',j'} [\Delta_\alpha(\mathbf{k})]_{i'j'} \frac{\omega^k(\mathcal{I}, \bar{g})}{\omega^k(\bar{g}, \mathcal{I})} [\bar{\lambda}_\alpha^k(\bar{g})]_{i'j} [\bar{\lambda}_\alpha^k(\bar{g})]_{j'i},
\end{aligned} \tag{2.2.5}$$

where we use the anticommutation relation of fermions.

From the above calculations, we obtain the representation of the Cooper pair wave function \bar{P}_α^k :

$$[\bar{P}_\alpha^k(\bar{g})]_{ij,i'j'} = \frac{\omega^k(\mathcal{I}, \bar{g})}{\omega^k(\bar{g}, \mathcal{I})} [\bar{\lambda}_\alpha^k(\bar{g})]_{i'i} [\bar{\lambda}_\alpha^k(\bar{g})]_{j'j}, \tag{2.2.6a}$$

$$[\bar{P}_\alpha^k(\mathcal{I}\bar{g})]_{ij,i'j'} = -\frac{\omega^k(\mathcal{I}, \bar{g})}{\omega^k(\bar{g}, \mathcal{I})} [\bar{\lambda}_\alpha^k(\bar{g})]_{i'j} [\bar{\lambda}_\alpha^k(\bar{g})]_{j'i}. \tag{2.2.6b}$$

Therefore, the character of P_α^k is given by

$$\begin{aligned}
\chi[\bar{P}_\alpha^k(\bar{g})] &= \sum_{ij} \frac{\omega^k(\mathcal{I}, \bar{g})}{\omega^k(\bar{g}, \mathcal{I})} [\bar{\lambda}_\alpha^k(\bar{g})]_{ii} [\bar{\lambda}_\alpha^k(\bar{g})]_{jj} \\
&= \frac{\omega^k(\mathcal{I}, \bar{g})}{\omega^k(\bar{g}, \mathcal{I})} \chi[\bar{\lambda}_\alpha^k(\bar{g})]^2,
\end{aligned} \tag{2.2.7a}$$

$$\begin{aligned}
\chi[\bar{P}_\alpha^k(\mathcal{I}\bar{g})] &= -\sum_{ij} \frac{\omega^k(\mathcal{I}, \bar{g})}{\omega^k(\bar{g}, \mathcal{I})} [\bar{\lambda}_\alpha^k(\bar{g})]_{ij} [\bar{\lambda}_\alpha^k(\bar{g})]_{ji} \\
&= -\frac{\omega^k(\mathcal{I}, \bar{g})\omega^k(\bar{g}, \bar{g})}{\omega^k(\bar{g}, \mathcal{I})} \chi[\bar{\lambda}_\alpha^k(\bar{g}^2)].
\end{aligned} \tag{2.2.7b}$$

These equations are Mackey-Bradley theorem described in Eqs. (2.2.1a) and (2.2.1b). ■

$$\begin{aligned}
&= \omega^{\mathcal{I}\bar{g}\mathcal{I}\mathbf{k}}(\mathcal{I}, \bar{g})\omega^{\mathcal{I}\bar{g}\mathcal{I}\mathbf{k}}(\mathcal{I}\bar{g}, \mathcal{I}) \sum_{j_3} c_{\alpha j_3}^\dagger(\mathcal{I}\bar{g}\mathcal{I}\mathbf{k}) [\bar{u}_\alpha^k(\overline{\mathcal{I}\bar{g}\mathcal{I}})]_{j_3j} \\
&= \frac{\omega^k(\mathcal{I}, \bar{g})}{\omega^k(\bar{g}, \mathcal{I})} \sum_{j'} c_{\alpha j'}^\dagger(\mathbf{k}) [\bar{\lambda}_\alpha^k(\bar{g})]_{j'j},
\end{aligned}$$

where we use $\mathcal{I}\bar{g}\mathcal{I} \in \mathcal{G}^k$ and $\overline{\mathcal{I}\bar{g}\mathcal{I}} = \bar{g}$ in the last equal.

2.3 Topological classification of superconducting gap

In this section, we consider the topological classification of the superconducting gap on high-symmetry points (mirror plane or rotation axis) in the BZ. As mentioned in Sec. 2.1, a unitary little cogroup on high-symmetry \mathbf{k} points in the BZ is denoted by $\bar{\mathcal{G}}^k$, and a IR of $\bar{\mathcal{G}}^k$ by α , which corresponds to the total angular momentum of the normal Bloch state $j_z = \pm 1/2, \pm 3/2, \dots$. Here, we define TRS, particle-hole symmetry (PHS), and chiral symmetry (CS) like operators preserving any \mathbf{k} points by $\mathfrak{T} \equiv \mathcal{T}\mathcal{I}$, $\mathfrak{C} \equiv C\mathcal{I}$, and $\Gamma \equiv \mathcal{T}C$, respectively. Thus the intrinsic symmetry is represented by the following group:

$$\bar{\mathfrak{G}}^k = \bar{\mathcal{G}}^k + \mathfrak{T}\bar{\mathcal{G}}^k + \mathfrak{C}\bar{\mathcal{G}}^k + \Gamma\bar{\mathcal{G}}^k. \quad (2.3.1)$$

Then, using the factor system $\{\omega^k(m_1, m_2)\} \in Z^2(\bar{\mathfrak{G}}^k, U(1)_\phi)$, we execute the *Wigner criteria* [38, 45–48] for \mathfrak{T} and \mathfrak{C} ,

$$W_\alpha^{\mathfrak{T}} \equiv \frac{1}{|\bar{\mathcal{G}}^k|} \sum_{\bar{g} \in \bar{\mathcal{G}}^k} \omega^k(\mathfrak{T}\bar{g}, \mathfrak{T}\bar{g}) \chi[\bar{\gamma}_\alpha^k(\overline{(\mathfrak{T}\bar{g})^2})] = \begin{cases} 1, \\ -1, \\ 0, \end{cases} \quad (2.3.2)$$

$$W_\alpha^{\mathfrak{C}} \equiv \frac{1}{|\bar{\mathcal{G}}^k|} \sum_{\bar{g} \in \bar{\mathcal{G}}^k} \omega^k(\mathfrak{C}\bar{g}, \mathfrak{C}\bar{g}) \chi[\bar{\gamma}_\alpha^k(\overline{(\mathfrak{C}\bar{g})^2})] = \begin{cases} 1, \\ -1, \\ 0, \end{cases} \quad (2.3.3)$$

and the *orthogonality test* [38, 48] for Γ :

$$W_\alpha^\Gamma \equiv \frac{1}{|\bar{\mathcal{G}}^k|} \sum_{\bar{g} \in \bar{\mathcal{G}}^k} \frac{\omega^k(\bar{g}, \Gamma)^*}{\omega^k(\Gamma, \Gamma^{-1}\bar{g}\Gamma)^*} \chi[\bar{\gamma}_\alpha^k(\overline{\Gamma^{-1}g\Gamma})^*] \chi[\bar{\gamma}_\alpha^k(\bar{g})] = \begin{cases} 1, \\ 0. \end{cases} \quad (2.3.4)$$

In the above tests, we investigate the orthogonality between $\{c_{ai}^\dagger(\mathbf{k})\}$ and $\{ac_{ai}^\dagger(\mathbf{k})a^{-1}\}$ ($a = \mathfrak{T}$, \mathfrak{C} , or Γ), where $c_{ai}^\dagger(\mathbf{k})$ is the i -th basis of the IR $\bar{\gamma}_\alpha^k$ (for details, see Appendixes A.1 and A.2). From Eqs. (2.3.2)–(2.3.4), we obtain the set of $(W_\alpha^{\mathfrak{T}}, W_\alpha^{\mathfrak{C}}, W_\alpha^\Gamma)$, which indicates the *effective* Altland-Zirnbauer (EAZ) symmetry class of the Bogoliubov-de Gennes (BdG) Hamiltonian on the high-symmetry points by using the knowledge of K theory [48, 52, 53]. Table 2.2 shows the correspondence between the set of $(W_\alpha^{\mathfrak{T}}, W_\alpha^{\mathfrak{C}}, W_\alpha^\Gamma)$ and the EAZ symmetry class.

Furthermore, from the EAZ symmetry class, we can classify the IR at the \mathbf{k} point into $0, \mathbb{Z}, 2\mathbb{Z}$ or \mathbb{Z}_2 (Table 2.2). In this context, $(W_\alpha^{\mathfrak{T}}, W_\alpha^{\mathfrak{C}}, W_\alpha^\Gamma)$ gives a symmetry-based topological classification of the Hamiltonian at each \mathbf{k} point on the plane (line). Therefore, when the plane (line) intersects a normal-state FS, the above information is nothing but a topological classification of superconducting gap nodes on the plane (line); when the classification is nontrivial ($\mathbb{Z}, 2\mathbb{Z}$, or \mathbb{Z}_2), the intersection leads to a node characterized by the topological invariant. Otherwise, a gap opens at the intersection line (point).

Table 2.2: Correspondence table between the set of $(W_\alpha^{\mathfrak{T}}, W_\alpha^{\mathfrak{C}}, W_\alpha^\Gamma)$ and the EAZ symmetry class. The fifth column shows a topological classification of the IR at the \mathbf{k} point for each EAZ class.

$W_\alpha^{\mathfrak{T}}$	$W_\alpha^{\mathfrak{C}}$	W_α^Γ	EAZ class	Classification
0	0	0	A	\mathbb{Z}
0	0	1	AIII	0
+1	0	0	AI	\mathbb{Z}
+1	+1	1	BDI	\mathbb{Z}_2
0	+1	0	D	\mathbb{Z}_2
-1	+1	1	DIII	0
-1	0	0	AII	$2\mathbb{Z}$
-1	-1	1	CII	0
0	-1	0	C	0
+1	-1	1	CI	0

2.4 Example: space group $P2_1/m$

In this section, we consider a unitary space group $G = P2_1/m$ as a simple example, which helps us understand the terminologies in Table 2.1 and the superconducting gap classification methods in Secs. 2.2 and 2.3. In the following discussion, we treat a magnetic space group $M = G + \{T|\mathbf{0}\}G = P2_1/m1'$ assuming the PM system.

2.4.1 Preparation

Since the magnetic space group M has a mirror operator $\mathcal{M}_z = \{M_z|_{\frac{\hat{z}}{2}}\}$, we focus on mirror-invariant planes $k_z = 0$ and $k_z = \pi$ in the BZ, where the (magnetic) little group is

$$\mathcal{G}^k = \mathbb{T} + \mathcal{M}_z \mathbb{T}, \quad (2.4.1)$$

$$\mathcal{M}^k = \mathcal{G}^k + \mathfrak{T}\mathcal{G}^k = \mathbb{T} + \mathcal{M}_z \mathbb{T} + \mathfrak{T}\mathbb{T} + \mathcal{M}_z \mathfrak{T}\mathbb{T}. \quad (2.4.2)$$

Therefore the (magnetic) little cogroup is

$$\bar{\mathcal{G}}^k = \mathcal{G}^k / \mathbb{T} = \{E, \mathcal{M}_z\}, \quad (2.4.3)$$

$$\bar{\mathcal{M}}^k = \mathcal{M}^k / \mathbb{T} = \{E, \mathcal{M}_z, \mathfrak{T}, \mathcal{M}_z \mathfrak{T}\}. \quad (2.4.4)$$

We find that the factor system is

$$\omega_{\text{in}}(\mathcal{M}_z, \mathcal{M}_z) = -1, \omega_{\text{in}}(\mathfrak{T}, \mathfrak{T}) = -1, \omega_{\text{in}}(\mathcal{M}_z, \mathfrak{T}) = \omega_{\text{in}}(\mathfrak{T}, \mathcal{M}_z), \quad (2.4.5a)$$

$$\omega_{\text{ns}}^k(\mathcal{M}_z, \mathcal{M}_z) = 1, \omega_{\text{ns}}^k(\mathfrak{T}\mathcal{M}_z, \mathfrak{T}\mathcal{M}_z) = e^{ik_z}. \quad (2.4.5b)$$

The projective IRs $\bar{\gamma}_{\pm 1/2}^k$ of the little cogroup $\bar{\mathcal{G}}^k$, with the factor system $\omega^k(\mathcal{M}_z, \mathcal{M}_z) = -1$, are given by

$$\bar{\gamma}_{\pm 1/2}^k(E) = 1, \quad \bar{\gamma}_{\pm 1/2}^k(\mathcal{M}_z) = \pm i, \quad (2.4.6)$$

which corresponds to spin-up and spin-down states, respectively. For the spin-up one ($\alpha = +1/2$), the Wigner criterion [38, 45–48] for TRS \mathfrak{T} is

$$\begin{aligned} W_{+1/2}^{\mathfrak{T}} &= \frac{1}{2} \sum_{\bar{g} \in \{E, \mathcal{M}_z\}} \omega^k(\mathfrak{T}\bar{g}, \mathfrak{T}\bar{g}) \chi[\bar{\gamma}_{+1/2}^k((\mathfrak{T}\bar{g})^2)] \\ &= \frac{1}{2}(-1 + e^{ik_z}) = \begin{cases} 0 & k_z = 0, \\ -1 & k_z = \pi. \end{cases} \end{aligned} \quad (2.4.7)$$

Thus the representation $\bar{\lambda}_{\pm 1/2}^k$ of the magnetic little cogroup $\bar{\mathcal{M}}^k$ can be constructed as follows:

\bar{m}	E	\mathcal{M}_z	\mathfrak{T}	$\mathcal{M}_z \mathfrak{T}$
$\bar{\lambda}_{\pm 1/2}^k(\bar{m})$	$\begin{pmatrix} 1 & 0 \\ 0 & 1 \end{pmatrix}$	$\begin{pmatrix} +i & 0 \\ 0 & -ie^{ik_z} \end{pmatrix}$	$\begin{pmatrix} 0 & 1 \\ -1 & 0 \end{pmatrix}$	$\begin{pmatrix} 0 & i \\ ie^{ik_z} & 0 \end{pmatrix}$

(2.4.8)

By using the above representation, the small corepresentation of $m \in \mathcal{M}^k$ is given by

$$\lambda^k(m) = e^{-ik \cdot \mathbf{R}} \bar{\lambda}^k(\bar{m}), \quad (2.4.9)$$

where $m = \bar{m}T_R$ with $\bar{m} \in \bar{\mathcal{M}}^k$ and $T_R = \{E|\mathbf{R}\} \in \mathbb{T}$.

2.4.2 Group-theoretical gap classification

Now we execute the group-theoretical gap classification (Sec. 2.2) on the mirror-invariant planes in the BZ. First of all, the factor system about the inversion symmetry \mathcal{I} is represented as follows:

$$\omega_{\text{in}}(\mathcal{I}, \mathcal{M}_z) = \omega_{\text{in}}(\mathcal{M}_z, \mathcal{I}) = 1, \quad (2.4.10a)$$

$$\omega_{\text{ns}}^k(\mathcal{I}, \mathcal{M}_z) = e^{ik_z}, \quad \omega_{\text{ns}}^k(\mathcal{M}_z, \mathcal{I}) = 1. \quad (2.4.10b)$$

Using the normal-state representation [Eq. (2.4.8)] and the Mackey-Bradley theorem [Eq. (2.2.1)], therefore, the representation $\bar{P}_{\pm 1/2}^k$ of Cooper-pair wave function is given by

$$\chi[\bar{P}_{\pm 1/2}^k(E)] = \frac{\omega^k(\mathcal{I}, E)}{\omega^k(E, \mathcal{I})} \chi[\bar{\lambda}_{\pm 1/2}^k(E)]^2 = 4, \quad (2.4.11a)$$

$$\chi[\bar{P}_{\pm 1/2}^k(\mathcal{M}_z)] = \frac{\omega^k(\mathcal{I}, \mathcal{M}_z)}{\omega^k(\mathcal{M}_z, \mathcal{I})} \chi[\bar{\lambda}_{\pm 1/2}^k(\mathcal{M}_z)]^2 = -e^{ik_z}(1 - e^{ik_z})^2, \quad (2.4.11b)$$

$$\chi[\bar{P}_{\pm 1/2}^k(\mathcal{I})] = -\frac{\omega^k(\mathcal{I}, E)\omega^k(E, \mathcal{I})}{\omega^k(E, \mathcal{I})} \chi[\bar{\lambda}_{\pm 1/2}^k(\overline{E^2})] = -2, \quad (2.4.11c)$$

$$\chi[\bar{P}_{\pm 1/2}^k(\mathcal{S}_2)] = -\frac{\omega^k(\mathcal{I}, \mathcal{M}_z)\omega^k(\mathcal{M}_z, \mathcal{M}_z)}{\omega^k(\mathcal{M}_z, \mathcal{I})} \chi[\bar{\lambda}_{\pm 1/2}^k(\overline{\mathcal{M}_z^2})] = 2e^{ik_z}, \quad (2.4.11d)$$

where $S_2 = \{C_2|\hat{\frac{z}{2}}\}$. We can decompose the pair representation $\bar{P}_{\pm 1/2}^k$ into IRs of the point group $C_{2h} \cong \bar{\mathcal{G}}^k + \mathcal{I}\bar{\mathcal{G}}^k$:

\bar{g}	E	\mathcal{M}_z	\mathcal{I}	S_2	Decomposition
$\bar{P}_{\pm 1/2}^{k_z=0}(\bar{g})$	4	0	-2	2	$A_g + 2A_u + B_u$
$\bar{P}_{\pm 1/2}^{k_z=\pi}(\bar{g})$	4	4	-2	-2	$A_g + 3B_u$

(2.4.12)

The decomposition shows the difference of superconducting gap structures between the BP $k_z = 0$ and the ZF $k_z = \pi$, which is attributed to the nonsymmorphic screw symmetry S_2 ; for example, A_u appears on $k_z = 0$, while it is prohibited on $k_z = \pi$. This means that, if the superconducting pairing symmetry belongs to the A_u IR, line nodes emerge only on the $k_z = \pi$ plane. Such an unusual nodal structure is considered to appear in some superconductors, *e.g.*, UPt₃ [6, 11–15], UCoGe [16], and CrAs [17].

2.4.3 Topological gap classification

We here confirm the group-theoretical classification result in the previous section, in terms of topological classification based on the EAZ symmetry class (Sec. 2.3). In this case, the little cogroup $\bar{\mathcal{G}}^k$ and its IR matrices $\bar{\gamma}_{\pm 1/2}^k$ have been given by Eqs. (2.4.3) and (2.4.6), respectively. Here we choose the representation matrix $\bar{\gamma}_{+1/2}^k$ of the IR $\alpha = +1/2$ and apply the topological classification introduced in Sec. 2.3.⁵

2.4.3.1 A_g gap function

Now we consider the A_g pair wave function of the point group C_{2h} . According to the group-theoretical gap classification, this function opens a superconducting gap on the line (see Eq. 2.4.12). Before going to the tests for the EAZ symmetry class, we prepare some relationships among the intrinsic symmetries. For the A_g pairing, we get the following factor system:

$$\omega_{\text{in}}(\mathfrak{C}, \mathfrak{C}) = 1, \quad \omega_{\text{in}}(\mathfrak{C}, \mathcal{M}_z) = \omega_{\text{in}}(\mathcal{M}_z, \mathfrak{C}), \quad (2.4.13a)$$

$$\omega_{\text{ns}}^k(\mathfrak{C}\mathcal{M}_z, \mathfrak{C}\mathcal{M}_z) = e^{ik_z}. \quad (2.4.13b)$$

Therefore⁶

$$\omega_{\text{in}}(\Gamma, \mathcal{M}_z) = \omega_{\text{in}}(\mathcal{M}_z, \Gamma), \quad (2.4.14a)$$

$$\omega_{\text{ns}}^k(\Gamma, \mathcal{M}_z) = \omega_{\text{ns}}^k(\mathcal{M}_z, \Gamma) = 1. \quad (2.4.14b)$$

⁵In this case, the final result is not changed even if we choose the other IR $\bar{\gamma}_{-1/2}^k$.

Next, we apply the topological classification to the normal Bloch state $\bar{\gamma}_{+1/2}^k$ and the A_g pair wave function. Using the above factor system, the Wigner criteria for \mathfrak{T} and \mathfrak{C} and the orthogonality test for Γ are given by

$$W_{+1/2}^{\mathfrak{T}} = \begin{cases} 0 & k_z = 0, \\ -1 & k_z = \pi, \end{cases} \quad (2.4.15)$$

$$\begin{aligned} W_{+1/2}^{\mathfrak{C}} &= \frac{1}{2} \left\{ \omega^k(\mathfrak{C}, \mathfrak{C}) \chi[\bar{\gamma}_{+1/2}^k(\overline{\mathfrak{C}^2})] + \omega^k(\mathfrak{C}\mathcal{M}_z, \mathfrak{C}\mathcal{M}_z) \chi[\bar{\gamma}_{+1/2}^k((\overline{\mathfrak{C}\mathcal{M}_z})^2)] \right\} \\ &= \frac{1}{2} (+1 - e^{ik_z}) = \begin{cases} 0 & k_z = 0, \\ +1 & k_z = \pi, \end{cases} \end{aligned} \quad (2.4.16)$$

$$\begin{aligned} W_{+1/2}^{\Gamma} &= \frac{1}{2} \left\{ \frac{\omega^k(E, \Gamma)}{\omega(\Gamma, \Gamma^{-1}E\Gamma)} \chi[\bar{\gamma}_{+1/2}^k(E)^*] \chi[\bar{\gamma}_{+1/2}^k(E)] \right. \\ &\quad \left. + \frac{\omega^k(\mathcal{M}_z, \Gamma)}{\omega(\Gamma, \Gamma^{-1}\mathcal{M}_z\Gamma)} \chi[\bar{\gamma}_{+1/2}^k(\overline{\Gamma^{-1}\mathcal{M}_z\Gamma})^*] \chi[\bar{\gamma}_{+1/2}^k(\mathcal{M}_z)] \right\} \\ &= \frac{1}{2}(1 + 1) = 1 \quad (k_z = 0, \pi). \end{aligned} \quad (2.4.17)$$

Thus, according to Table 2.2, the classifying space is identified as the EAZ symmetry class AIII (DIII) on the $k_z = 0$ ($k_z = \pi$) plane. Since the both classes are classified into 0, the gap classification is topologically trivial. This means that the A_g pair wave function opens a gap on the mirror-invariant planes, which is consistent with the group-theoretical classification.

Here we explain the meaning of the EAZ symmetry class. Figure 2.1 represents a schematic picture of the BdG Hamiltonian with the A_g pair wave function. First, we see the classification on the BP $k_z = 0$ [Fig. 2.1(a)]. In the above discussion, we started from the representation matrix $\bar{\gamma}_{+1/2}^k$ of the IR $\alpha = +1/2$, which corresponds to the normal Bloch state [the lower left particle in Fig. 2.1(a)]. The Wigner criterion for the TRS-like operator \mathfrak{T} results in $W_{+1/2}^{\mathfrak{T}} = 0$ [Eq. (2.4.15)], which indicates that \mathfrak{T} gives a basis of the nonequivalent IR (see Appendix A.1). Therefore the lower left particle in Fig. 2.1(a) is mapped by \mathfrak{T} to the lower right particle, which belongs to the other IR $\alpha = -1/2$. Similarly, since $W_{+1/2}^{\mathfrak{C}} = 0$ [Eq. (2.4.16)], the lower left particle is mapped by \mathfrak{C} to the upper right hole. On the other hand, since the orthogonality test leads to $W_{+1/2}^{\Gamma} = 1$ [Eq. (2.4.17)], the CS gives the basis of the equivalent IR (see Appendix A.2). Thus the lower left

⁶Taking into account the factor system in Eqs. (2.4.5) and (2.4.13), we can easily derive it by the following commutation relation:

$$\begin{aligned} [u(\Gamma), u(\mathcal{M}_z)] &= \omega_{\text{in}}(\mathfrak{T}, \mathfrak{C})^{-1} \{u(\mathfrak{T})u(\mathfrak{C})^*u(\mathcal{M}_z) - u(\mathcal{M}_z)u(\mathfrak{T})u(\mathfrak{C})^*\} \\ &= \omega_{\text{in}}(\mathfrak{T}, \mathfrak{C})^{-1} \{u(\mathfrak{T})u(\mathfrak{C})^*u(\mathcal{M}_z) - u(\mathfrak{T})u(\mathcal{M}_z)^*u(\mathfrak{C})^*\} \\ &= \omega_{\text{in}}(\mathfrak{T}, \mathfrak{C})^{-1} \{u(\mathfrak{T})u(\mathfrak{C})^*u(\mathcal{M}_z) - u(\mathfrak{T})u(\mathfrak{C})^*u(\mathcal{M}_z)\} = 0, \end{aligned}$$

where we use $\Gamma = \mathcal{T}\mathcal{C} = \mathfrak{T}\mathfrak{C}$.

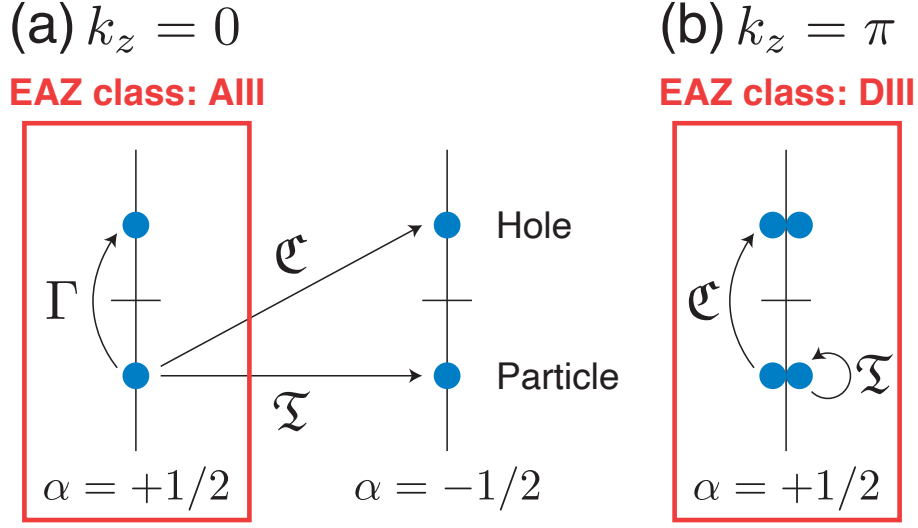


Figure 2.1: Schematic picture of the BdG Hamiltonian with the A_g pair wave function on mirror-invariant planes (a) $k_z = 0$ and (b) $k_z = \pi$. The red-framed spaces for (a) and (b) belong to the EAZ class AIII and DIII, respectively.

particle in Fig. 2.1(a) is mapped by Γ to the upper left hole, which belongs to the same IR $\alpha = +1/2$. For the above reason, the Hamiltonian in the space of $\bar{\gamma}_{+1/2}^k$ [the red frame in Fig. 2.1(a)] has only the CS Γ , which indicates the AZ class AIII [52, 53].

On the ZF $k_z = \pi$, on the other hand, the situation is changed [Fig. 2.1(b)]. In this case, the Wigner criteria for \mathfrak{T} and \mathfrak{C} are $W_{+1/2}^{\mathfrak{T}} = -1$ [Eq. (2.4.15)] and $W_{+1/2}^{\mathfrak{C}} = +1$ [Eq. (2.4.16)], respectively. They indicate that each of \mathfrak{T} and \mathfrak{C} gives a basis of the equivalent IR $+1/2$, and as a result, the CS also gives the same IR: $W_{+1/2}^{\Gamma} = 1$ [Eq. (2.4.17)]. Note that the mapped basis by the TRS \mathfrak{T} is linearly independent of the original basis, due to the result $W_{+1/2}^{\mathfrak{T}} = -1$ (see Appendix A.1). Therefore the lower particle in Fig. 2.1(b) is mapped, by the any symmetries \mathfrak{T} , \mathfrak{C} , and Γ , to the particle and holes belonging to the same IR $\alpha = +1/2$. That is why the Hamiltonian in the space of $\bar{\gamma}_{+1/2}^k$ [the red frame in Fig. 2.1(b)] is classified into the AZ class DIII [52, 53].

Furthermore, we see an intuitive understanding of the gap opening in the A_g symmetry. For simplicity, we only treat the BP $k_z = 0$ case in the discussion. Within the weak-coupling limit, *i.e.*, for the negligibly small inter-band pairing, it is sufficient to discuss the single-band model. In this case, the BdG Hamiltonian $H_{\text{BdG}}(\mathbf{k})$ on the mirror plane is generally written as follows:

$$H_{\text{BdG}}(\mathbf{k}) = \frac{1}{2} \mathbf{C}^\dagger(\mathbf{k}) \hat{H}_{\text{BdG}}(\mathbf{k}) \mathbf{C}(\mathbf{k}), \quad (2.4.18)$$

$$\mathbf{C}^\dagger(\mathbf{k}) = (c_{+1/2}^\dagger(\mathbf{k}), \mathfrak{T} c_{+1/2}^\dagger(\mathbf{k}) \mathfrak{T}^{-1}, \mathfrak{C} c_{+1/2}^\dagger(\mathbf{k}) \mathfrak{C}^{-1}, \Gamma c_{+1/2}^\dagger(\mathbf{k}) \Gamma^{-1}), \quad (2.4.19)$$

where $c_{+1/2}^\dagger(\mathbf{k})$ is a creation operator of a $j_z = +1/2$ Bloch state in a band-based representation,

which is the basis of the IR $\bar{\gamma}_{+1/2}^k$:

$$g c_{+1/2}^\dagger(\mathbf{k}) g^{-1} = \bar{\gamma}_{+1/2}^k(g) c_{+1/2}^\dagger(\mathbf{k}) \text{ for } g \in \bar{\mathcal{G}}^k. \quad (2.4.20)$$

$\hat{H}_{\text{BdG}}(\mathbf{k})$ is the matrix representation of $H_{\text{BdG}}(\mathbf{k})$:

$$\hat{H}_{\text{BdG}}(\mathbf{k}) = \begin{pmatrix} \xi(\mathbf{k})\sigma_0 & \Delta_0\psi(\mathbf{k})i\sigma_y \\ (\Delta_0\psi(\mathbf{k})i\sigma_y)^\dagger & -\xi(\mathbf{k})\sigma_0 \end{pmatrix}, \quad (2.4.21)$$

where $\xi(\mathbf{k})$ is the normal energy dispersion, and σ_i represents the Pauli matrix in pseudo-spin space. Here, the *spin-singlet* A_g gap function is defined as

$$\frac{1}{2}\Delta_0\psi(\mathbf{k}) \left\{ c_{+1/2}^\dagger(\mathbf{k})(\Gamma c_{+1/2}^\dagger(\mathbf{k})\Gamma^{-1})^\dagger - \mathfrak{T}c_{+1/2}^\dagger(\mathbf{k})\mathfrak{T}^{-1}(\mathfrak{C}c_{+1/2}^\dagger(\mathbf{k})\mathfrak{C}^{-1})^\dagger \right\} + \text{H.c.}, \quad (2.4.22)$$

where the magnitude of the gap function Δ_0 is chosen as a real number without loss of generality.

Due to the \mathcal{M}_z symmetry, the BdG Hamiltonian matrix commutes with the mirror reflection matrix $\hat{U}_{\text{BdG}}^k(\mathcal{M}_z)$:

$$[\hat{H}_{\text{BdG}}(\mathbf{k}), \hat{U}_{\text{BdG}}^k(\mathcal{M}_z)] = 0. \quad (2.4.23)$$

Therefore $\hat{H}_{\text{BdG}}(\mathbf{k})$ and $\hat{U}_{\text{BdG}}^k(\mathcal{M}_z)$ are simultaneously block-diagonalized; namely, there exists a unitary matrix \hat{V} such that

$$\hat{H}_{\text{BdG}}(\mathbf{k}) = \hat{V} \begin{pmatrix} \hat{H}_+(\mathbf{k}) & 0 \\ 0 & \hat{H}_-(\mathbf{k}) \end{pmatrix} \hat{V}^\dagger, \quad (2.4.24)$$

$$\hat{U}_{\text{BdG}}^k(\mathcal{M}_z) = \hat{V} \begin{pmatrix} +i\mathbf{1}_2 & 0 \\ 0 & -i\mathbf{1}_2 \end{pmatrix} \hat{V}^\dagger, \quad (2.4.25)$$

where we use $\omega^{k_z=0}(\mathcal{M}_z, \mathcal{M}_z) = -1$. The block-diagonalized Hamiltonian $H_+(\mathbf{k})$ and $H_-(\mathbf{k})$ are written as follows:

$$H_\pm(\mathbf{k}) = \frac{1}{2} \mathbf{C}_\pm^\dagger(\mathbf{k}) \hat{H}_\pm(\mathbf{k}) \mathbf{C}_\pm(\mathbf{k}), \quad (2.4.26)$$

$$\hat{H}_\pm(\mathbf{k}) = \begin{pmatrix} \xi(\mathbf{k}) & \pm\Delta_0\psi(\mathbf{k}) \\ \pm\Delta_0\psi(\mathbf{k})^* & -\xi(\mathbf{k}) \end{pmatrix}, \quad (2.4.27)$$

$$\mathbf{C}_+^\dagger(\mathbf{k}) = (c_{+1/2}^\dagger(\mathbf{k}), \Gamma c_{+1/2}^\dagger(\mathbf{k})\Gamma^{-1}), \quad (2.4.28)$$

$$\mathbf{C}_-^\dagger(\mathbf{k}) = (\mathfrak{T}c_{+1/2}^\dagger(\mathbf{k})\mathfrak{T}^{-1}, \mathfrak{C}c_{+1/2}^\dagger(\mathbf{k})\mathfrak{C}^{-1}), \quad (2.4.29)$$

since Γ does not change the eigenvalue of $\hat{U}_{\text{BdG}}^k(\mathcal{M}_z)$, but \mathfrak{T} and \mathfrak{C} do that.

Figure 2.2(a) schematically illustrates the band structures obtained by the BdG Hamiltonian (2.4.24). First, considering $\Delta_0 \rightarrow 0$ limit [left panel in Fig. 2.2(a)], we get the particle band

$$\xi(\mathbf{k})c_{+1/2}^\dagger(\mathbf{k})c_{+1/2}(\mathbf{k}) - (\xi(\mathbf{k})\mathfrak{T}c_{+1/2}^\dagger(\mathbf{k})c_{+1/2}(\mathbf{k})\mathfrak{T}^{-1}), \quad (2.4.30)$$

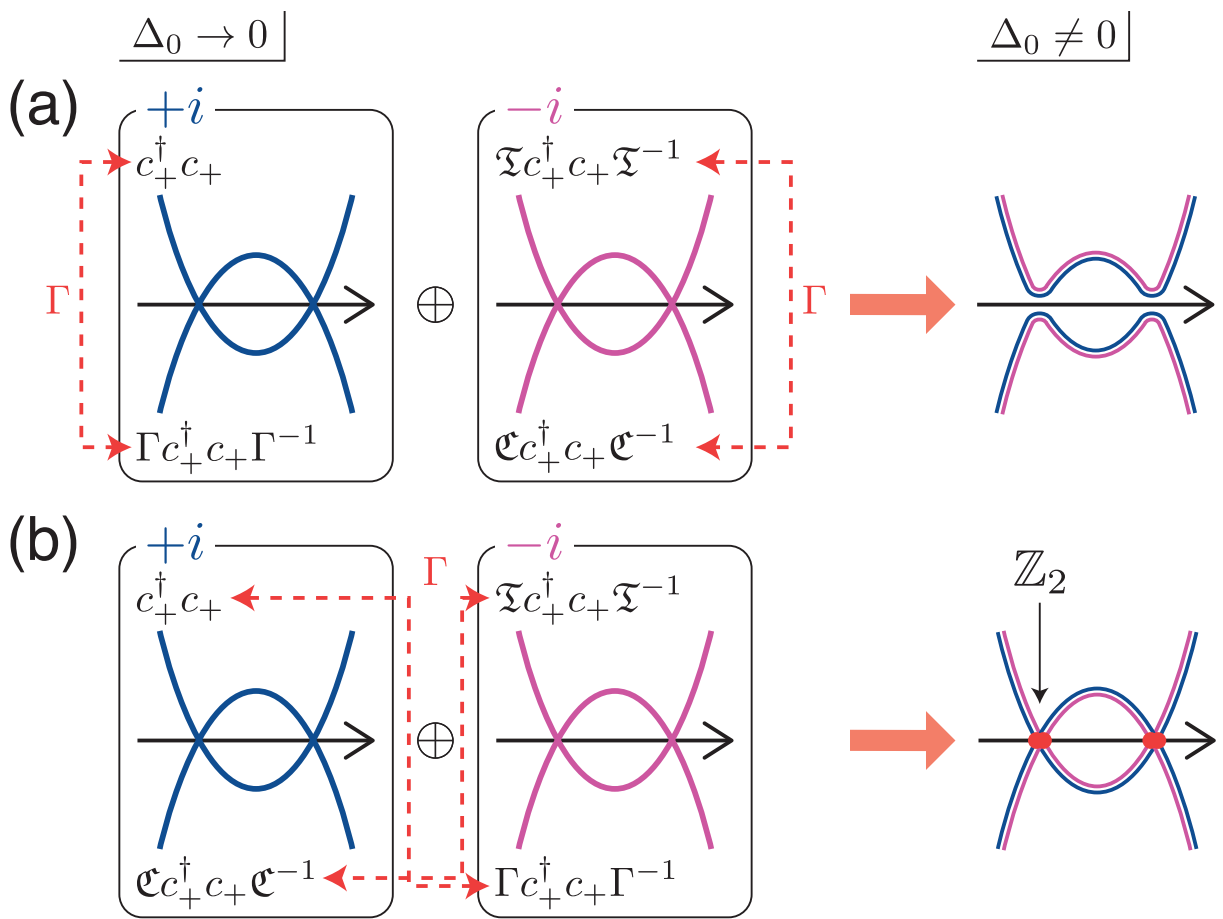


Figure 2.2: Band-theoretical picture of the BdG Hamiltonian with (a) the A_g pair wave function and (b) the B_g pair wave function on the mirror-invariant BP $k_z = 0$. c_+^\dagger is the abbreviated notation of $c_{+1/2}^\dagger(\mathbf{k})$. The red points represent nodes on the plane.

and the hole band

$$-\xi(\mathbf{k})\Gamma c_{+1/2}^\dagger(\mathbf{k})c_{+1/2}(\mathbf{k})\Gamma^{-1} \quad (-\xi(\mathbf{k})\mathfrak{C} c_{+1/2}^\dagger(\mathbf{k})c_{+1/2}(\mathbf{k})\mathfrak{C}^{-1}), \quad (2.4.31)$$

in the eigenspace of the eigenvalue $+i$ ($-i$). When the magnitude of the gap function Δ_0 is finite, therefore, the A_g pair wave function [Eq. (2.4.22)] can have finite off-diagonal components in each $+i$ and $-i$ eigenspace [see Eq. (2.4.27)]. These functions open the gaps at the zero energy [right panel in Fig. 2.2(a)]. This fact indicates the existence of gap on the mirror-invariant plane.

2.4.3.2 B_g gap function

Next, we investigate the B_g pair wave function on the mirror planes. Group-theoretical gap classification shows the emergence of line nodes on the planes (see Eq. 2.4.12).

We again choose the IR $\bar{\gamma}_{+1/2}^k$ and apply the topological classification. For the B_g pairing, the factor system is

$$\omega_{\text{in}}(\mathfrak{C}, \mathfrak{C}) = 1, \quad \omega_{\text{in}}(\mathfrak{C}, \mathcal{M}_z) = -\omega_{\text{in}}(\mathcal{M}_z, \mathfrak{C}), \quad (2.4.32a)$$

$$\omega_{\text{ns}}^k(\mathfrak{C}\mathcal{M}_z, \mathfrak{C}\mathcal{M}_z) = e^{ik_z}. \quad (2.4.32b)$$

Therefore,

$$\omega_{\text{in}}(\Gamma, \mathcal{M}_z) = -\omega_{\text{in}}(\mathcal{M}_z, \Gamma), \quad (2.4.33a)$$

$$\omega_{\text{ns}}^k(\Gamma, \mathcal{M}_z) = \omega_{\text{ns}}^k(\mathcal{M}_z, \Gamma) = 1. \quad (2.4.33b)$$

By using the above factor system, the Wigner criteria for \mathfrak{T} and \mathfrak{C} and the orthogonality test for Γ are given by

$$W_{+1/2}^{\mathfrak{T}} = \begin{cases} 0 & k_z = 0, \\ -1 & k_z = \pi, \end{cases} \quad (2.4.34)$$

$$W_{+1/2}^{\mathfrak{C}} = \frac{1}{2}(+1 + e^{ik_z}) = \begin{cases} +1 & k_z = 0, \\ 0 & k_z = \pi, \end{cases} \quad (2.4.35)$$

$$W_{+1/2}^{\Gamma} = \frac{1}{2}(1 - 1) = 0 \quad (k_z = 0, \pi). \quad (2.4.36)$$

According to Table 2.2, therefore, the classifying space is identified as the EAZ symmetry class D (AII) on the $k_z = 0$ ($k_z = \pi$) plane. Since the class D (AII) is classified into \mathbb{Z}_2 ($2\mathbb{Z}$), nodes emerge on the mirror-invariant planes by the B_g pair wave function when the FSs cross the planes. This node is topologically protected.

Figure 2.3 represents the schematic picture of the BdG Hamiltonian with the B_g pair wave function. On the BP $k_z = 0$, the normal Bloch basis of $\bar{\gamma}_{+1/2}^k$, namely, the lower left particle in Fig. 2.3(a), is mapped by \mathfrak{T} to the lower right particle belonging to the other IR $\alpha = -1/2$,

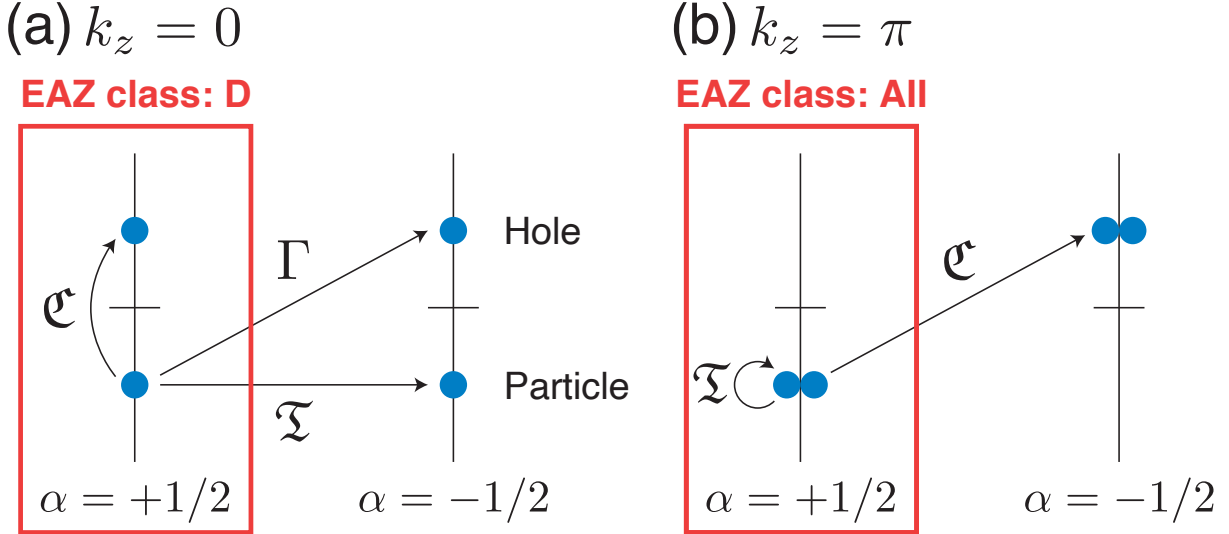


Figure 2.3: Schematic picture of the BdG Hamiltonian with the B_g pair wave function on mirror-invariant planes (a) $k_z = 0$ and (b) $k_z = \pi$. The red-framed spaces for (a) and (b) belong to the EAZ class D and AII, respectively.

because the Wigner criterion for the TRS \mathfrak{T} is $W_{+1/2}^{\mathfrak{T}} = 0$ [Eq. (2.4.34)]. Similarly, since $W_{+1/2}^{\Gamma} = 0$ [Eq. (2.4.36)], the lower left particle is mapped by Γ to the upper right hole. On the other hand, since the Wigner criterion for the PHS is $W_{+1/2}^{\mathfrak{C}} = +1$ [Eq. (2.4.35)], \mathfrak{C} gives the basis of the equivalent IR which does *not* generate an additional degeneracy (see Appendix A.1). Thus the lower left particle in Fig. 2.3(a) is mapped by \mathfrak{C} to the upper left hole belonging to the same IR $\alpha = +1/2$. For the above reason, the BdG Hamiltonian in the space of $\bar{\gamma}_{+1/2}^k$ [the red frame in Fig. 2.3(a)] has only the PHS \mathfrak{C} with $\mathfrak{C}^2 = +E$, which indicates the AZ class D [52, 53].

On the ZF $k_z = \pi$, the lower left particle in Fig. 2.3(b) is degenerated by \mathfrak{T} belonging to the equivalent IR $\alpha = +1/2$, because of the Wigner criterion $W_{+1/2}^{\mathfrak{T}} = -1$ [Eq. (2.4.34)]. On the other hand, since $W_{+1/2}^{\mathfrak{T}} = W_{+1/2}^{\Gamma} = 0$ [Eqs. (2.4.35) and (2.4.36)], the lower left particle is mapped by the PHS \mathfrak{C} and the CS Γ to the upper right holes in the nonequivalent IR $\alpha = -1/2$. Therefore, the Hamiltonian in the space of $\bar{\gamma}_{+1/2}^k$ [the red frame in Fig. 2.3(b)] has only the TRS \mathfrak{T} with $\mathfrak{T}^2 = -E$, which indicates the AZ class AII [52, 53].

Furthermore, we discuss an intuitive picture of the nodes appearing in the B_g symmetry for the BP $k_z = 0$ case. As is the case for the A_g IR, the BdG Hamiltonian matrix $\hat{H}_{\text{BdG}}(\mathbf{k})$ [Eq. (2.4.21)] and the mirror reflection matrix $\hat{U}_{\text{BdG}}^k(\mathcal{M}_z)$ are simultaneously block-diagonalized on the mirror-invariant plane [Eqs. (2.4.24) and (2.4.25)]. For the B_g IR, the Hamiltonian blocks $H_+(\mathbf{k})$ and

$H_-(\mathbf{k})$ are written as follows:

$$H_{\pm}(\mathbf{k}) = \frac{1}{2} \mathbf{C}_{\pm}^{\dagger}(\mathbf{k}) \hat{H}_{\pm}(\mathbf{k}) \mathbf{C}_{\pm}(\mathbf{k}), \quad (2.4.37)$$

$$\hat{H}_{\pm}(\mathbf{k}) = \begin{pmatrix} \xi(\mathbf{k}) & 0 \\ 0 & -\xi(\mathbf{k}) \end{pmatrix}, \quad (2.4.38)$$

$$\mathbf{C}_+^{\dagger}(\mathbf{k}) = (c_{+1/2}^{\dagger}(\mathbf{k}), \mathfrak{C} c_{+1/2}^{\dagger}(\mathbf{k}) \mathfrak{C}^{-1}), \quad (2.4.39)$$

$$\mathbf{C}_-^{\dagger}(\mathbf{k}) = (\mathfrak{T} c_{+1/2}^{\dagger}(\mathbf{k}) \mathfrak{T}^{-1}, \Gamma c_{+1/2}^{\dagger}(\mathbf{k}) \Gamma^{-1}), \quad (2.4.40)$$

since \mathfrak{C} does not change the eigenvalue of $\hat{U}_{\text{BdG}}^k(\mathcal{M}_z)$, but \mathfrak{T} and Γ do that. Note that the off-diagonal components of $\hat{H}_{\pm}(\mathbf{k})$ are zero because the *spin-singlet* B_g gap function has the same form as Eq. (2.4.22), which is *not* allowed in the equivalent eigenspace of $\pm i$. In other words, the momentum dependence of the B_g gap function $\psi(\mathbf{k})$ leads to the gap closing on the mirror plane, even when the magnitude Δ_0 is finite. The band structures are schematically shown in Fig. 2.2(b), which indicates the emergence of line nodes on the mirror plane $k_z = 0$ [right panel in Fig. 2.2(b)].

Finally, we comment on the \mathbb{Z}_2 classification of the gap node. As shown in Eq. (2.4.24), the BdG Hamiltonian matrix in this symmetry can be decomposed into the two matrices belonging to different eigenspaces of $\pm i$: $\hat{H}_+(\mathbf{k}) \oplus \hat{H}_-(\mathbf{k})$. Both matrices possess the PHS \mathfrak{C} with $\mathfrak{C}^2 = +E$. Therefore $\hat{H}_{\pm}(\mathbf{k})$ can be transformed into antisymmetric matrices by using the unitary part $\hat{U}_{\mathfrak{C}} = \hat{U}_{\mathfrak{C},+} \oplus \hat{U}_{\mathfrak{C},-}$ of the PHS \mathfrak{C} [31, 54]. Thus the nodes in each eigenspace are characterized by a \mathbb{Z}_2 number:

$$(-1)^{l_{\pm}} = \text{sgn}[i^n \text{Pf}\{\hat{U}_{\mathfrak{C},\pm} \hat{H}_{\pm}(\mathbf{k})\}] \in \mathbb{Z}_2, \quad (2.4.41)$$

with $n = \dim(\hat{H}_{\pm})/2$. This \mathbb{Z}_2 protection of nodes is the same as that of Bogoliubov FSs in even-parity chiral superconductors [31].

Chapter 3

Superconducting gap classification on high-symmetry planes

In this Chapter, using the classification theory introduced in Chapter 2, we completely classify the superconducting gap structures on high-symmetry (namely mirror- or glide-invariant) planes in the BZ. From the group-theoretical analysis, the classification tables for all possible symmetries are given in Sec. 3.1. The tables clarify the condition for nontrivial line nodes or gap opening on the BZ boundary, which are protected by nonsymmorphic symmetry. Next, in Sec. 3.2, we see a one-to-one correspondence between the group-theoretical and topological classification: all crystal-symmetry-protected line nodes on high-symmetry planes are also characterized by 0D and/or 1D topological numbers. Furthermore, we discuss the possibility of Majorana flat bands as surface states corresponding to the 1D topological number. Finally, as an example, we demonstrate nonsymmorphic-symmetry-protected gap structures in the model of Sr_2IrO_4 (Sec. 3.3).

3.1 Group-theoretical classification of symmetry-protected line nodes

In this section, we completely classify symmetry-protected line nodes on mirror- or glide-invariant planes [6, 11–17], clarifying the condition for the presence or absence of line nodes protected by nonsymmorphic symmetry. Furthermore, we show an additional constraint: line nodes (gap opening) peculiar to nonsymmorphic systems appear only on the ZF for 59 *primitive or orthorhombic base-centered space groups*. We provide classification tables (Table 3.2) of the space groups, which may allow nontrivial superconducting gap structures by nonsymmorphic symmetry.

3.1.1 Setup

First, we show constraints on crystal symmetry of the system where the formalism in Sec. 2.2 is applicable. Since this method requires the symmetry operation connecting \mathbf{k} and $-\mathbf{k}$, the system must be invariant under the IS \mathcal{I} . The symmetry-protected line node may appear on the high-symmetry \mathbf{k} -planes when a FS crosses the plane and the gap function vanishes there. Thus, we need to consider \mathbf{k} -planes as high-symmetry \mathbf{k} -points in order to discuss line nodes. Only an identity operation and a mirror reflection (or a glide reflection) are allowed as elements of the unitary little group for the general point on the high-symmetry \mathbf{k} -planes.

For the above reasons, we assume that the symmetry of the system contains point group C_{2h} , which is generated by a spatial inversion and a mirror reflection. In other words, the space group of the system G has a subgroup $H \subset G$ such that $H/\mathbb{T} \cong C_{2h}$. Taking translations into account, H is classified as follows:

$$H = \{E|\mathbf{0}\}\mathbb{T} + \{M_\perp|\mathbf{t}_M\}\mathbb{T} + \{I|\mathbf{0}\}\mathbb{T} + \{C_{2\perp}|\mathbf{t}_M\}\mathbb{T}, \quad (3.1.1a)$$

$$\mathbf{t}_M = \begin{cases} \mathbf{0} & (\text{RM}) \text{ Rotation + Mirror}, \\ \mathbf{t}_\parallel & (\text{RG}) \text{ Rotation + Glide}, \\ \mathbf{t}_\perp & (\text{SM}) \text{ Screw + Mirror}, \\ \mathbf{t}_\parallel + \mathbf{t}_\perp & (\text{SG}) \text{ Screw + Glide}. \end{cases} \quad (3.1.1b)$$

The translation group \mathbb{T} defines a Bravais Lattice, and $\mathbf{t}_i = \hat{r}_i/2$ ($i = \parallel$ or \perp) are non-primitive translation vectors. E denotes an identity operation, M_\perp is a mirror reflection about the plane perpendicular to the r_\perp axis, and $C_{2\perp}$ is a π -rotation around the r_\perp axis. Note that the direction of the twofold axis is represented by a symbol \perp , while the other directions orthogonal to the twofold axis are represented by a symbol \parallel [Fig. 3.1(a)]. In Eq. (3.1.1), the (RM) space group is symmorphic, and the other (RG), (SM), and (SG) space groups are nonsymmorphic.

Next, we discuss the magnetic (anti-unitary) symmetry of the system. When the system is FM, all the time-reversal operation is forbidden. On the other hand, in the PM or AFM state, the system is invariant under the anti-unitary operation,

$$\bar{\mathcal{T}} = \{T|\mathbf{t}_{\mathcal{T}}\}, \quad (3.1.2a)$$

$$\mathbf{t}_{\mathcal{T}} = \begin{cases} \mathbf{0} & (\text{PM}), \\ \mathbf{t}_\parallel & (\text{AFM1}), \\ \mathbf{t}_\perp & (\text{AFM2}), \\ \mathbf{t}_\parallel + \mathbf{t}_\perp & (\text{AFM3}). \end{cases} \quad (3.1.2b)$$

The pure TRS is allowed in the (PM) state, while the system is invariant under the successive operations of time-reversal and non-primitive translation in the (AFM1)-(AFM3) states. For example, a magnetic structure of the (AFM1) state is shown in Fig. 3.1(b): although magnetic moments (red

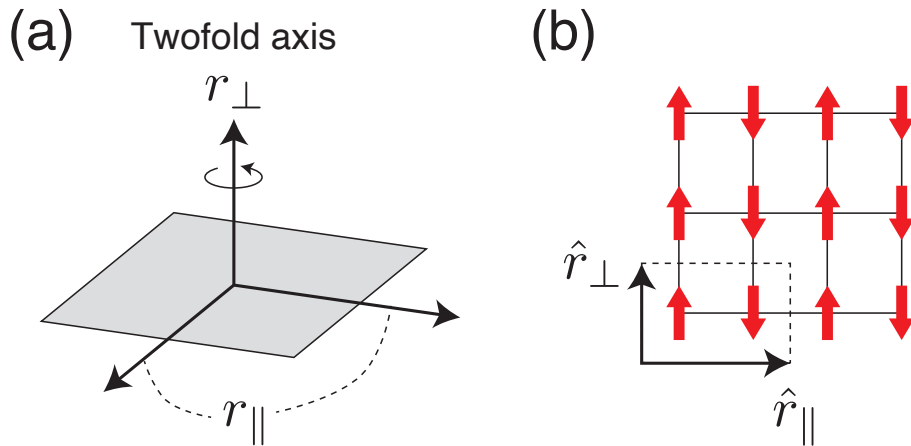


Figure 3.1: (a) The coordinate r_{\perp} along the twofold axis, and the other coordinates r_{\parallel} perpendicular to the twofold axis. (b) An example of the AFM1 case. The red arrows illustrate magnetic moments on a square lattice, and the dashed line indicates a magnetic unit cell.

arrows) flip under the time-reversal operation, the magnetic structure recovers after a half-translation $t_{\parallel} = \hat{r}_{\parallel}/2$.

3.1.2 Gap classification

By adding the anti-unitary operators (3.1.2) to the unitary space group (3.1.1), we can construct the magnetic space group $M = H$ (FM) or $M = H + \bar{\mathcal{T}}H$ (PM or AFM). Based on the magnetic space group, the gap classification introduced in Sec. 2.2 is applied to high-symmetry, namely, mirror- or glide-invariant planes in the BZ: the BP at $k_{\perp} = 0$ and the ZF at $k_{\perp} = \pi$. The obtained results are summarized in Table 3.1. In this table, the representations of superconducting gap functions are classified by the IRs of point group C_{2h} . We also show candidate materials for unusual gap structures, one of which is Sr_2IrO_4 [18] discussed in Sec. 3.3.

The classification of a superconducting gap on BPs is consistent with the Sigrist-Ueda method. On the other hand, the representations allowed on the ZF may differ from those on the BP. Then, the line nodes (or gap opening) protected by nonsymmorphic symmetry appear on the ZF. Such a situation is realized when the space group is (SM) or (SG), and/or the pseudo-TRS is (AFM2) or (AFM3). In other words, when the system preserves the symmetry operation(s) including non-primitive translation perpendicular to the mirror plane $[t_M]_{\perp} \neq 0$ and/or $[t_T]_{\perp} \neq 0$, the symmetry ensures nontrivial gap structures beyond the Sigrist-Ueda method.

Results consistent with Table 3.1 have been recently shown by Micklitz and Norman [17]. Using a Clifford algebra technique, they also confirmed that the line nodes by nonsymmorphic symmetry are protected by a \mathbb{Z} topological number. A further discussion [19] about the topological stability of the line nodes and resulting surface states, namely Majorana flat bands, is given in Sec. 3.2.

Table 3.1: Classification of superconducting gap on high-symmetry \mathbf{k} -plane. H and $\tilde{\mathcal{T}}$ specify the space group by Eqs. (3.1.1) and (3.1.2). The representations of Cooper pairs allowed on the high-symmetry \mathbf{k} -planes (BP and ZF) are shown. Materials realizing the space groups are also shown.

Cases	H	$\tilde{\mathcal{T}}$	Key ingredients
(1a)	(RM), (RG)	N/A	$[t_M]_\perp = 0$
(1b)	(SM), (SG)	N/A	$[t_M]_\perp \neq 0$
(2a)	(RM), (RG)	(PM), (AFM1)	$[t_M]_\perp = [t_T]_\perp = 0$
(2b)	(RM), (RG)	(AFM2), (AFM3)	$[t_M]_\perp = 0, [t_T]_\perp \neq 0$
(2c)	(SM), (SG)	(PM), (AFM1)	$[t_M]_\perp \neq 0, [t_T]_\perp = 0$
(2d)	(SM), (SG)	(AFM2), (AFM3)	$[t_M]_\perp \neq 0, [t_T]_\perp \neq 0$

Cases	BP ($k_\perp = 0$)	ZF ($k_\perp = \pi$)	Materials
(1a)	A_u	A_u	
(1b)	A_u	B_u	UCoGe (FM) [16], URhGe [16]
(2a)	$A_g + 2A_u + B_u$	$A_g + 2A_u + B_u$	
(2b)	$A_g + 2A_u + B_u$	$B_g + 3A_u$	Sr ₂ IrO ₄ (vertical) [18], UPt ₃ (AFM) [17]
(2c)	$A_g + 2A_u + B_u$	$A_g + 3B_u$	UPt ₃ (PM) [6, 11–15], UCoGe (PM) [16], CrAs [17]
(2d)	$A_g + 2A_u + B_u$	$B_g + A_u + 2B_u$	UPd ₂ Al ₃ [16, 17, 42], UNi ₂ Al ₃ [17], Sr ₂ IrO ₄ (horizontal) [18]

3.1.3 Application to 59 space groups

In the above discussion, we have shown the gap classification of line nodes on mirror- or glide-invariant planes. Here we reconsider constraints on the crystal symmetry of the system. Space groups containing C_{2h} symmetry are divided into four types: primitive, orthorhombic base-centered, body-centered, and face-centered space groups. All types of space groups have one or more mirror-invariant BPs ($k_\perp = 0$) in the BZ. On the other hand, corresponding mirror-invariant ZFs ($k_\perp = \pi$) exist only for primitive or orthorhombic base-centered space groups. Although some of body-centered or face-centered space groups also have mirror-invariant ZFs, all of them are $k_\perp = 2\pi$ planes, where the gap classification gives the same result as that on BPs ($k_\perp = 0$ planes). Examples of mirror-invariant BPs and ZFs in the BZ of a primitive or orthorhombic base-centered Bravais lattice are illustrated in Figs. 3.2(a)-3.2(d).

As shown in Table 3.1, unconventional line nodes (gap opening) protected by nonsymmorphic symmetry appear on $k_\perp = \pi$ planes. Therefore, we conclude that nontrivial nonsymmorphic-symmetry-protected line nodes may appear not for a body-centered or face-centered Bravais lattice, but for a *primitive or orthorhombic base-centered Bravais lattice*. This additional constraint simplifies the classification of space groups with respect to the superconducting gap structure.

For the above reason, we classify here only primitive and orthorhombic base-centered space groups containing C_{2h} symmetry, which may allow nontrivial gap structures by nonsymmorphic

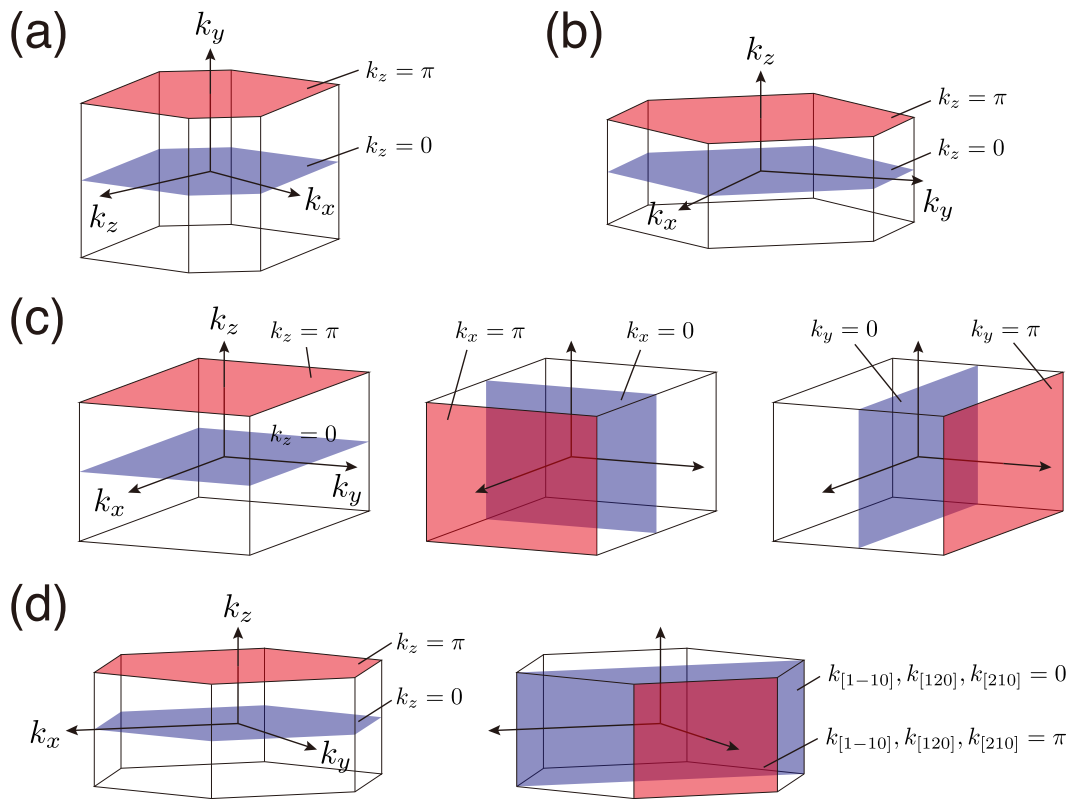


Figure 3.2: Mirror-invariant BPs and ZFs in the first BZ for (a) monoclinic primitive, (b) orthorhombic base-centered, (c) orthorhombic primitive / tetragonal primitive / cubic primitive, and (d) hexagonal primitive Bravais lattice. The blue and red planes represent BPs and ZFs, respectively.

Table 3.2: Gap classification for (a) monoclinic, (b) orthorhombic, (c) tetragonal, (d) hexagonal, and (e) cubic space groups. The table for the orthorhombic groups shows primitive and base-centered Bravais lattices, while the other tables show the primitive Bravais lattice. The first and second columns show the number and the name of space groups. The fourth column represents the type of the space groups in Eq. (3.1.1), corresponding to the direction (in the third column) of mirror-invariant BP and ZF. [see also Figs. 3.2(a)-3.2(d)]. Note that the direction “ v ” means x and y in the (c) tetragonal space groups, and [1–10], [120], and [210] in the (d) hexagonal ones. The fifth and sixth columns show the gap classification for *PM superconductors* on the BP $k_{\perp} = 0$ and the ZF $k_{\perp} = \pi$, respectively.

No.	Short	\perp	Type	$k_{\perp} = 0$	$k_{\perp} = \pi$
(a) Monoclinic					
10	$P2/m$	y	(RM)	$A_g + 2A_u + B_u$	$A_g + 2A_u + B_u$
11	$P2_1/m$	y	(SM)	$A_g + 2A_u + B_u$	$A_g + 3B_u$
13	$P2/c$	y	(RG)	$A_g + 2A_u + B_u$	$A_g + 2A_u + B_u$
14	$P2_1/c$	y	(SG)	$A_g + 2A_u + B_u$	$A_g + 3B_u$
(b) Orthorhombic					
47	$Pmmm$	x	(RM)	$A_g + B_{3g} + 2A_u + B_{1u} + B_{2u} + 2B_{3u}$	$A_g + B_{3g} + 2A_u + B_{1u} + B_{2u} + 2B_{3u}$
		y	(RM)	$A_g + B_{2g} + 2A_u + B_{1u} + 2B_{2u} + B_{3u}$	$A_g + B_{2g} + 2A_u + B_{1u} + 2B_{2u} + B_{3u}$
		z	(RM)	$A_g + B_{1g} + 2A_u + 2B_{1u} + B_{2u} + B_{3u}$	$A_g + B_{1g} + 2A_u + 2B_{1u} + B_{2u} + B_{3u}$
48	$Pnnn$	x	(RG)	$A_g + B_{3g} + 2A_u + B_{1u} + B_{2u} + 2B_{3u}$	$A_g + B_{3g} + 2A_u + B_{1u} + B_{2u} + 2B_{3u}$
		y	(RG)	$A_g + B_{2g} + 2A_u + B_{1u} + 2B_{2u} + B_{3u}$	$A_g + B_{2g} + 2A_u + B_{1u} + 2B_{2u} + B_{3u}$
		z	(RG)	$A_g + B_{1g} + 2A_u + 2B_{1u} + B_{2u} + B_{3u}$	$A_g + B_{1g} + 2A_u + 2B_{1u} + B_{2u} + B_{3u}$
49	$Pccm$	x	(RG)	$A_g + B_{3g} + 2A_u + B_{1u} + B_{2u} + 2B_{3u}$	$A_g + B_{3g} + 2A_u + B_{1u} + B_{2u} + 2B_{3u}$
		y	(RG)	$A_g + B_{2g} + 2A_u + B_{1u} + 2B_{2u} + B_{3u}$	$A_g + B_{2g} + 2A_u + B_{1u} + 2B_{2u} + B_{3u}$
		z	(RM)	$A_g + B_{1g} + 2A_u + 2B_{1u} + B_{2u} + B_{3u}$	$A_g + B_{1g} + 2A_u + 2B_{1u} + B_{2u} + B_{3u}$
50	$Pban$	x	(RG)	$A_g + B_{3g} + 2A_u + B_{1u} + B_{2u} + 2B_{3u}$	$A_g + B_{3g} + 2A_u + B_{1u} + B_{2u} + 2B_{3u}$
		y	(RG)	$A_g + B_{2g} + 2A_u + B_{1u} + 2B_{2u} + B_{3u}$	$A_g + B_{2g} + 2A_u + B_{1u} + 2B_{2u} + B_{3u}$
		z	(RG)	$A_g + B_{1g} + 2A_u + 2B_{1u} + B_{2u} + B_{3u}$	$A_g + B_{1g} + 2A_u + 2B_{1u} + B_{2u} + B_{3u}$
51	$Pmma$	x	(SM)	$A_g + B_{3g} + 2A_u + B_{1u} + B_{2u} + 2B_{3u}$	$A_g + B_{3g} + 3B_{1u} + 3B_{2u}$
		y	(RM)	$A_g + B_{2g} + 2A_u + B_{1u} + 2B_{2u} + B_{3u}$	$A_g + B_{2g} + 2A_u + B_{1u} + 2B_{2u} + B_{3u}$
		z	(RG)	$A_g + B_{1g} + 2A_u + 2B_{1u} + B_{2u} + B_{3u}$	$A_g + B_{1g} + 2A_u + 2B_{1u} + B_{2u} + B_{3u}$
52	$Pnna$	x	(RG)	$A_g + B_{3g} + 2A_u + B_{1u} + B_{2u} + 2B_{3u}$	$A_g + B_{3g} + 2A_u + B_{1u} + B_{2u} + 2B_{3u}$
		y	(SG)	$A_g + B_{2g} + 2A_u + B_{1u} + 2B_{2u} + B_{3u}$	$A_g + B_{2g} + 3B_{1u} + 3B_{3u}$
		z	(RG)	$A_g + B_{1g} + 2A_u + 2B_{1u} + B_{2u} + B_{3u}$	$A_g + B_{1g} + 2A_u + 2B_{1u} + B_{2u} + B_{3u}$
53	$Pmna$	x	(RM)	$A_g + B_{3g} + 2A_u + B_{1u} + B_{2u} + 2B_{3u}$	$A_g + B_{3g} + 2A_u + B_{1u} + B_{2u} + 2B_{3u}$
		y	(RG)	$A_g + B_{2g} + 2A_u + B_{1u} + 2B_{2u} + B_{3u}$	$A_g + B_{2g} + 2A_u + B_{1u} + 2B_{2u} + B_{3u}$
		z	(SG)	$A_g + B_{1g} + 2A_u + 2B_{1u} + B_{2u} + B_{3u}$	$A_g + B_{1g} + 3B_{2u} + 3B_{3u}$
54	$Pcca$	x	(SG)	$A_g + B_{3g} + 2A_u + B_{1u} + B_{2u} + 2B_{3u}$	$A_g + B_{3g} + 3B_{1u} + 3B_{2u}$
		y	(RG)	$A_g + B_{2g} + 2A_u + B_{1u} + 2B_{2u} + B_{3u}$	$A_g + B_{2g} + 2A_u + B_{1u} + 2B_{2u} + B_{3u}$
		z	(RG)	$A_g + B_{1g} + 2A_u + 2B_{1u} + B_{2u} + B_{3u}$	$A_g + B_{1g} + 2A_u + 2B_{1u} + B_{2u} + B_{3u}$

Table 3.2: (Continued).

No.	Short	\perp	Type	$k_{\perp} = 0$	$k_{\perp} = \pi$
55	<i>Pbam</i>	<i>x</i>	(SG)	$A_g + B_{3g} + 2A_u + B_{1u} + B_{2u} + 2B_{3u}$	$A_g + B_{3g} + 3B_{1u} + 3B_{2u}$
		<i>y</i>	(SG)	$A_g + B_{2g} + 2A_u + B_{1u} + 2B_{2u} + B_{3u}$	$A_g + B_{2g} + 3B_{1u} + 3B_{3u}$
		<i>z</i>	(RM)	$A_g + B_{1g} + 2A_u + 2B_{1u} + B_{2u} + B_{3u}$	$A_g + B_{1g} + 2A_u + 2B_{1u} + B_{2u} + B_{3u}$
56	<i>Pccn</i>	<i>x</i>	(SG)	$A_g + B_{3g} + 2A_u + B_{1u} + B_{2u} + 2B_{3u}$	$A_g + B_{3g} + 3B_{1u} + 3B_{2u}$
		<i>y</i>	(SG)	$A_g + B_{2g} + 2A_u + B_{1u} + 2B_{2u} + B_{3u}$	$A_g + B_{2g} + 3B_{1u} + 3B_{3u}$
		<i>z</i>	(RG)	$A_g + B_{1g} + 2A_u + 2B_{1u} + B_{2u} + B_{3u}$	$A_g + B_{1g} + 2A_u + 2B_{1u} + B_{2u} + B_{3u}$
57	<i>Pbcm</i>	<i>x</i>	(RG)	$A_g + B_{3g} + 2A_u + B_{1u} + B_{2u} + 2B_{3u}$	$A_g + B_{3g} + 2A_u + B_{1u} + B_{2u} + 2B_{3u}$
		<i>y</i>	(SG)	$A_g + B_{2g} + 2A_u + B_{1u} + 2B_{2u} + B_{3u}$	$A_g + B_{2g} + 3B_{1u} + 3B_{3u}$
		<i>z</i>	(SM)	$A_g + B_{1g} + 2A_u + 2B_{1u} + B_{2u} + B_{3u}$	$A_g + B_{1g} + 3B_{2u} + 3B_{3u}$
58	<i>Pnnm</i>	<i>x</i>	(SG)	$A_g + B_{3g} + 2A_u + B_{1u} + B_{2u} + 2B_{3u}$	$A_g + B_{3g} + 3B_{1u} + 3B_{2u}$
		<i>y</i>	(SG)	$A_g + B_{2g} + 2A_u + B_{1u} + 2B_{2u} + B_{3u}$	$A_g + B_{2g} + 3B_{1u} + 3B_{3u}$
		<i>z</i>	(RM)	$A_g + B_{1g} + 2A_u + 2B_{1u} + B_{2u} + B_{3u}$	$A_g + B_{1g} + 2A_u + 2B_{1u} + B_{2u} + B_{3u}$
59	<i>Pmmn</i>	<i>x</i>	(SM)	$A_g + B_{3g} + 2A_u + B_{1u} + B_{2u} + 2B_{3u}$	$A_g + B_{3g} + 3B_{1u} + 3B_{2u}$
		<i>y</i>	(SM)	$A_g + B_{2g} + 2A_u + B_{1u} + 2B_{2u} + B_{3u}$	$A_g + B_{2g} + 3B_{1u} + 3B_{3u}$
		<i>z</i>	(RG)	$A_g + B_{1g} + 2A_u + 2B_{1u} + B_{2u} + B_{3u}$	$A_g + B_{1g} + 2A_u + 2B_{1u} + B_{2u} + B_{3u}$
60	<i>Pbcn</i>	<i>x</i>	(SG)	$A_g + B_{3g} + 2A_u + B_{1u} + B_{2u} + 2B_{3u}$	$A_g + B_{3g} + 3B_{1u} + 3B_{2u}$
		<i>y</i>	(RG)	$A_g + B_{2g} + 2A_u + B_{1u} + 2B_{2u} + B_{3u}$	$A_g + B_{2g} + 2A_u + B_{1u} + 2B_{2u} + B_{3u}$
		<i>z</i>	(SG)	$A_g + B_{1g} + 2A_u + 2B_{1u} + B_{2u} + B_{3u}$	$A_g + B_{1g} + 3B_{2u} + 3B_{3u}$
61	<i>Pbca</i>	<i>x</i>	(SG)	$A_g + B_{3g} + 2A_u + B_{1u} + B_{2u} + 2B_{3u}$	$A_g + B_{3g} + 3B_{1u} + 3B_{2u}$
		<i>y</i>	(SG)	$A_g + B_{2g} + 2A_u + B_{1u} + 2B_{2u} + B_{3u}$	$A_g + B_{2g} + 3B_{1u} + 3B_{3u}$
		<i>z</i>	(SG)	$A_g + B_{1g} + 2A_u + 2B_{1u} + B_{2u} + B_{3u}$	$A_g + B_{1g} + 3B_{2u} + 3B_{3u}$
62	<i>Pnma</i>	<i>x</i>	(SG)	$A_g + B_{3g} + 2A_u + B_{1u} + B_{2u} + 2B_{3u}$	$A_g + B_{3g} + 3B_{1u} + 3B_{2u}$
		<i>y</i>	(SM)	$A_g + B_{2g} + 2A_u + B_{1u} + 2B_{2u} + B_{3u}$	$A_g + B_{2g} + 3B_{1u} + 3B_{3u}$
		<i>z</i>	(SG)	$A_g + B_{1g} + 2A_u + 2B_{1u} + B_{2u} + B_{3u}$	$A_g + B_{1g} + 3B_{2u} + 3B_{3u}$
63	<i>Cmcm</i>	<i>z</i>	(SM)	$A_g + B_{1g} + 2A_u + 2B_{1u} + B_{2u} + B_{3u}$	$A_g + B_{1g} + 3B_{2u} + 3B_{3u}$
64	<i>Cmca</i>	<i>z</i>	(SG)	$A_g + B_{1g} + 2A_u + 2B_{1u} + B_{2u} + B_{3u}$	$A_g + B_{1g} + 3B_{2u} + 3B_{3u}$
65	<i>Cmmm</i>	<i>z</i>	(RM)	$A_g + B_{1g} + 2A_u + 2B_{1u} + B_{2u} + B_{3u}$	$A_g + B_{1g} + 2A_u + 2B_{1u} + B_{2u} + B_{3u}$
66	<i>Cccm</i>	<i>z</i>	(RM)	$A_g + B_{1g} + 2A_u + 2B_{1u} + B_{2u} + B_{3u}$	$A_g + B_{1g} + 2A_u + 2B_{1u} + B_{2u} + B_{3u}$
67	<i>Cmma</i>	<i>z</i>	(RG)	$A_g + B_{1g} + 2A_u + 2B_{1u} + B_{2u} + B_{3u}$	$A_g + B_{1g} + 2A_u + 2B_{1u} + B_{2u} + B_{3u}$
68	<i>Ccca</i>	<i>z</i>	(RG)	$A_g + B_{1g} + 2A_u + 2B_{1u} + B_{2u} + B_{3u}$	$A_g + B_{1g} + 2A_u + 2B_{1u} + B_{2u} + B_{3u}$
(c) Tetragonal					
83	<i>P4/m</i>	<i>z</i>	(RM)	$A_g + B_g + 2A_u + 2B_u + E_u$	$A_g + B_g + 2A_u + 2B_u + E_u$
84	<i>P4₂/m</i>	<i>z</i>	(RM)	$A_g + B_g + 2A_u + 2B_u + E_u$	$A_g + B_g + 2A_u + 2B_u + E_u$
85	<i>P4/n</i>	<i>z</i>	(RG)	$A_g + B_g + 2A_u + 2B_u + E_u$	$A_g + B_g + 2A_u + 2B_u + E_u$
86	<i>P4₂/n</i>	<i>z</i>	(RG)	$A_g + B_g + 2A_u + 2B_u + E_u$	$A_g + B_g + 2A_u + 2B_u + E_u$
123	<i>P4/mmm</i>	<i>z</i>	(RM)	$A_{1g} + A_{2g} + B_{1g} + B_{2g} + 2A_{1u} + 2A_{2u} + 2B_{1u} + 2B_{2u} + 2E_u$	$A_{1g} + A_{2g} + B_{1g} + B_{2g} + 2A_{1u} + 2A_{2u} + 2B_{1u} + 2B_{2u} + 2E_u$
		<i>v</i>	(RM)	$A_{1g} + B_{1g} + E_g + 2A_{1u} + A_{2u} + 2B_{1u} + B_{2u} + 3E_u$	$A_{1g} + B_{1g} + E_g + 2A_{1u} + A_{2u} + 2B_{1u} + B_{2u} + 3E_u$

Table 3.2: (Continued).

Table 3.2: (Continued).

No.	Short	\perp	Type	$k_{\perp} = 0$	$k_{\perp} = \pi$
134	$P4_2/nnm$	z	(RG)	$A_{1g} + A_{2g} + B_{1g} + B_{2g} + 2A_{1u} + 2A_{2u} + 2B_{1u} + 2B_{2u} + 2E_u$	$A_{1g} + A_{2g} + B_{1g} + B_{2g} + 2A_{1u} + 2A_{2u} + 2B_{1u} + 2B_{2u} + 2E_u$
		v	(RG)	$A_{1g} + B_{1g} + E_g + 2A_{1u} + A_{2u} + 2B_{1u} + B_{2u} + 3E_u$	$A_{1g} + B_{1g} + E_g + 2A_{1u} + A_{2u} + 2B_{1u} + B_{2u} + 3E_u$
135	$P4_2/mbc$	z	(RM)	$A_{1g} + A_{2g} + B_{1g} + B_{2g} + 2A_{1u} + 2A_{2u} + 2B_{1u} + 2B_{2u} + 2E_u$	$A_{1g} + A_{2g} + B_{1g} + B_{2g} + 2A_{1u} + 2A_{2u} + 2B_{1u} + 2B_{2u} + 2E_u$
		v	(SG)	$A_{1g} + B_{1g} + E_g + 2A_{1u} + A_{2u} + 2B_{1u} + B_{2u} + 3E_u$	$A_{1g} + B_{1g} + E_g + 3A_{2u} + 3B_{2u} + 3E_u$
136	$P4_2/mnm$	z	(RM)	$A_{1g} + A_{2g} + B_{1g} + B_{2g} + 2A_{1u} + 2A_{2u} + 2B_{1u} + 2B_{2u} + 2E_u$	$A_{1g} + A_{2g} + B_{1g} + B_{2g} + 2A_{1u} + 2A_{2u} + 2B_{1u} + 2B_{2u} + 2E_u$
		v	(SG)	$A_{1g} + B_{1g} + E_g + 2A_{1u} + A_{2u} + 2B_{1u} + B_{2u} + 3E_u$	$A_{1g} + B_{1g} + E_g + 3A_{2u} + 3B_{2u} + 3E_u$
137	$P4_2/nmc$	z	(RG)	$A_{1g} + A_{2g} + B_{1g} + B_{2g} + 2A_{1u} + 2A_{2u} + 2B_{1u} + 2B_{2u} + 2E_u$	$A_{1g} + A_{2g} + B_{1g} + B_{2g} + 2A_{1u} + 2A_{2u} + 2B_{1u} + 2B_{2u} + 2E_u$
		v	(SM)	$A_{1g} + B_{1g} + E_g + 2A_{1u} + A_{2u} + 2B_{1u} + B_{2u} + 3E_u$	$A_{1g} + B_{1g} + E_g + 3A_{2u} + 3B_{2u} + 3E_u$
138	$P4_2/ncm$	z	(RG)	$A_{1g} + A_{2g} + B_{1g} + B_{2g} + 2A_{1u} + 2A_{2u} + 2B_{1u} + 2B_{2u} + 2E_u$	$A_{1g} + A_{2g} + B_{1g} + B_{2g} + 2A_{1u} + 2A_{2u} + 2B_{1u} + 2B_{2u} + 2E_u$
		v	(SG)	$A_{1g} + B_{1g} + E_g + 2A_{1u} + A_{2u} + 2B_{1u} + B_{2u} + 3E_u$	$A_{1g} + B_{1g} + E_g + 3A_{2u} + 3B_{2u} + 3E_u$
(d) Hexagonal					
175	$P6/m$	z	(RM)	$A_g + E_{2g} + 2A_u + B_u + E_{1u} + 2E_{2u}$	$A_g + E_{2g} + 2A_u + B_u + E_{1u} + 2E_{2u}$
176	$P6_3/m$	z	(SM)	$A_g + E_{2g} + 2A_u + B_u + E_{1u} + 2E_{2u}$	$A_g + E_{2g} + 3B_u + 3E_{1u}$
191	$P6/mmm$	z	(RM)	$A_{1g} + A_{2g} + 2E_{2g} + 2A_{1u} + 2A_{2u} + B_{1u} + B_{2u} + 2E_{1u} + 4E_{2u}$	$A_{1g} + A_{2g} + 2E_{2g} + 2A_{1u} + 2A_{2u} + B_{1u} + B_{2u} + 2E_{1u} + 4E_{2u}$
		v	(RM)	$A_{1g} + B_{2g} + E_{1g} + E_{2g} + 2A_{1u} + A_{2u} + B_{1u} + 2B_{2u} + 3E_{1u} + 3E_{2u}$	$A_{1g} + B_{2g} + E_{1g} + E_{2g} + 2A_{1u} + A_{2u} + B_{1u} + 2B_{2u} + 3E_{1u} + 3E_{2u}$
192	$P6/mcc$	z	(RM)	$A_{1g} + A_{2g} + 2E_{2g} + 2A_{1u} + 2A_{2u} + B_{1u} + B_{2u} + 2E_{1u} + 4E_{2u}$	$A_{1g} + A_{2g} + 2E_{2g} + 2A_{1u} + 2A_{2u} + B_{1u} + B_{2u} + 2E_{1u} + 4E_{2u}$
		v	(RG)	$A_{1g} + B_{2g} + E_{1g} + E_{2g} + 2A_{1u} + A_{2u} + B_{1u} + 2B_{2u} + 3E_{1u} + 3E_{2u}$	$A_{1g} + B_{2g} + E_{1g} + E_{2g} + 2A_{1u} + A_{2u} + B_{1u} + 2B_{2u} + 3E_{1u} + 3E_{2u}$
193	$P6_3/mcm$	z	(SM)	$A_{1g} + A_{2g} + 2E_{2g} + 2A_{1u} + 2A_{2u} + B_{1u} + B_{2u} + 2E_{1u} + 4E_{2u}$	$A_{1g} + A_{2g} + 2E_{2g} + 3B_{1u} + 3B_{2u} + 6E_{1u}$
		v	(RM)	$A_{1g} + B_{2g} + E_{1g} + E_{2g} + 2A_{1u} + A_{2u} + B_{1u} + 2B_{2u} + 3E_{1u} + 3E_{2u}$	$A_{1g} + B_{2g} + E_{1g} + E_{2g} + 2A_{1u} + A_{2u} + B_{1u} + 2B_{2u} + 3E_{1u} + 3E_{2u}$
194	$P6_3/mmc$	z	(SM)	$A_{1g} + A_{2g} + 2E_{2g} + 2A_{1u} + 2A_{2u} + B_{1u} + B_{2u} + 2E_{1u} + 4E_{2u}$	$A_{1g} + A_{2g} + 2E_{2g} + 3B_{1u} + 3B_{2u} + 6E_{1u}$
		v	(RG)	$A_{1g} + B_{2g} + E_{1g} + E_{2g} + 2A_{1u} + A_{2u} + B_{1u} + 2B_{2u} + 3E_{1u} + 3E_{2u}$	$A_{1g} + B_{2g} + E_{1g} + E_{2g} + 2A_{1u} + A_{2u} + B_{1u} + 2B_{2u} + 3E_{1u} + 3E_{2u}$

Table 3.2: (Continued).

No.	Short	\perp	Type	$k_{\perp} = 0$	$k_{\perp} = \pi$
(e) Cubic					
200	$Pm\bar{3}$	x, y, z	(RM)	$A_g + E_g + T_g + 2A_u + 2E_u + 4T_u$	$A_g + E_g + T_g + 2A_u + 2E_u + 4T_u$
201	$Pn\bar{3}$	x, y, z	(RG)	$A_g + E_g + T_g + 2A_u + 2E_u + 4T_u$	$A_g + E_g + T_g + 2A_u + 2E_u + 4T_u$
205	$Pa\bar{3}$	x, y, z	(SG)	$A_g + E_g + T_g + 2A_u + 2E_u + 4T_u$	$A_g + E_g + T_g + 6T_u$
221	$Pm\bar{3}m$	x, y, z	(RM)	$A_{1g} + A_{2g} + 2E_g + T_{1g} + T_{2g} + 2A_{1u} + 2A_{2u} + 4E_u + 4T_{1u} + 4T_{2u}$	$A_{1g} + A_{2g} + 2E_g + T_{1g} + T_{2g} + 2A_{1u} + 2A_{2u} + 4E_u + 4T_{1u} + 4T_{2u}$
222	$Pn\bar{3}n$	x, y, z	(RG)	$A_{1g} + A_{2g} + 2E_g + T_{1g} + T_{2g} + 2A_{1u} + 2A_{2u} + 4E_u + 4T_{1u} + 4T_{2u}$	$A_{1g} + A_{2g} + 2E_g + T_{1g} + T_{2g} + 2A_{1u} + 2A_{2u} + 4E_u + 4T_{1u} + 4T_{2u}$
223	$Pm\bar{3}n$	x, y, z	(RM)	$A_{1g} + A_{2g} + 2E_g + T_{1g} + T_{2g} + 2A_{1u} + 2A_{2u} + 4E_u + 4T_{1u} + 4T_{2u}$	$A_{1g} + A_{2g} + 2E_g + T_{1g} + T_{2g} + 2A_{1u} + 2A_{2u} + 4E_u + 4T_{1u} + 4T_{2u}$
224	$Pn\bar{3}m$	x, y, z	(RG)	$A_{1g} + A_{2g} + 2E_g + T_{1g} + T_{2g} + 2A_{1u} + 2A_{2u} + 4E_u + 4T_{1u} + 4T_{2u}$	$A_{1g} + A_{2g} + 2E_g + T_{1g} + T_{2g} + 2A_{1u} + 2A_{2u} + 4E_u + 4T_{1u} + 4T_{2u}$

symmetry. Symmetry on BPs and ZFs [colored planes in Figs. 3.2(a)-3.2(d)] are classified into (RM), (RG), (SM), or (SG) of Eq. (3.1.1), which enables us to determine the corresponding superconducting gap structure on the planes, using Table 3.1, when the magnetic symmetry is given. The results of the space group classification and the gap classification for *PM superconductors* are summarized in Tables 3.2(a)-3.2(e). Even for FM and AFM superconductors, we can straightforwardly elucidate the gap structure by combining Tables 3.1 and 3.2. Therefore, the group-theoretical classification on high-symmetry planes is completed.

Finally, space groups of the candidate materials for nonsymmorphic line nodes (gap opening) are illustrated in the following.

- PM UPt₃ [6, 11–15]:

$$G = P6_3/mmc \text{ [Table 3.2(d)]}, \\ \bar{\mathcal{T}} = \{T|\mathbf{0}\};$$

- PM UCoGe [16]:

$$G = Pnma \text{ [Table 3.2(b)]}, \\ \bar{\mathcal{T}} = \{T|\mathbf{0}\};$$

- FM UCoGe [16]:

$$G = P2_1/c \text{ [Table 3.2(a)]};$$

- AFM UPd₂Al₃ [16, 17, 42]:

$$G = P2_1/m \text{ [Table 3.2(a)]}, \\ \bar{\mathcal{T}} = \{T|\mathbf{t}_{\perp}\};$$

- AFM Sr₂IrO₄ [18]:

$$G = Pcc\bar{a} \text{ [Table 3.2(b)]},$$

$$\tilde{\mathcal{T}} = \{T|t_{\parallel} + t_{\perp}\}.$$

3.2 Topological classification of symmetry-protected line nodes and Majorana flat bands

Let us now discuss the symmetry-protected line nodes from the viewpoint of topology. Such topological properties are of importance in identifying the bulk-boundary correspondence, *i.e.*, the line-node-induced Majorana flat bands. We can formulate the topology of line nodes using the BdG Hamiltonian,

$$H_{\text{BdG}} = \frac{1}{2} \sum_{\mathbf{k}, i, j} \mathbf{C}_i^{\dagger}(\mathbf{k}) [\hat{H}_{\text{BdG}}(\mathbf{k})]_{ij} \mathbf{C}_j(\mathbf{k}), \quad (3.2.1)$$

with $\mathbf{C}_i^{\dagger}(\mathbf{k}) = (c_i^{\dagger}(\mathbf{k}), c_i(-\mathbf{k}))$. We note that this Hamiltonian exhibits PHS since

$$\hat{U}_{\text{BdG}}(\bar{C}) \hat{H}_{\text{BdG}}(\mathbf{k})^* \hat{U}_{\text{BdG}}(\bar{C})^{\dagger} = -\hat{H}_{\text{BdG}}(-\mathbf{k}), \quad (3.2.2)$$

where $\hat{U}_{\text{BdG}}(\bar{C}) = \tau_x$ is the anti-unitary operator, and τ_i is the Pauli matrix in Nambu space. We choose a periodic Bloch basis so that $\hat{H}_{\text{BdG}}(\mathbf{k}) = \hat{H}_{\text{BdG}}(\mathbf{k} + \mathbf{G})$, where \mathbf{G} a reciprocal lattice vector.

First, we consider how the symmetry operations affect the BdG Hamiltonian. The creation operator of an electron transforms under a unitary space group operation g as

$$g c_i^{\dagger}(\mathbf{k}) g^{-1} = \sum_j c_j^{\dagger}(g\mathbf{k}) [e^{-ig\mathbf{k}\cdot\boldsymbol{\tau}_g} \bar{u}^k(g)]_{ji}, \quad (3.2.3)$$

where $\bar{g} = \{I|\mathbf{0}\}$, $\{M_{\perp}|\mathbf{t}_{\mathcal{M}}\}$, and $\{C_{2\perp}|\mathbf{t}_{\mathcal{M}}\}$. We dub them as $\bar{\mathcal{I}}$, $\bar{\mathcal{M}}_{\perp}$, and $\bar{\mathcal{C}}_{2\perp}$, respectively. If the BdG Hamiltonian is invariant with respect to the symmetry operations, one yields

$$\hat{U}_{\text{BdG}}^k(\bar{g}) \hat{H}_{\text{BdG}}(\mathbf{k}) \hat{U}_{\text{BdG}}^k(\bar{g})^{\dagger} = \hat{H}_{\text{BdG}}(g\mathbf{k}), \quad (3.2.4)$$

with $\hat{U}_{\text{BdG}}^k(\bar{g}) = \text{diag}[\bar{u}^k(\bar{g}), \eta_g \bar{u}^{-k}(\bar{g})^*]$. Here, $\eta_g = \omega_{\text{in}}(C, g)/\omega_{\text{in}}(g, C) = \pm 1$, where the choice of sign is the same as the sign of the character of g in the IR of the order parameter. In addition, \mathcal{T} acts on the creation operators as

$$\mathcal{T} c_i^{\dagger}(\mathbf{k}) \mathcal{T}^{-1} = c_i^{\dagger}(-\mathbf{k}) [e^{i\mathbf{k}\cdot\boldsymbol{\tau}_{\mathcal{T}}} \bar{u}^k(\bar{\mathcal{T}})]_{ji}, \quad (3.2.5)$$

which yields

$$\hat{U}_{\text{BdG}}^k(\bar{\mathcal{T}}) \hat{H}_{\text{BdG}}(\mathbf{k})^* \hat{U}_{\text{BdG}}^k(\bar{\mathcal{T}})^{\dagger} = \hat{H}_{\text{BdG}}(-\mathbf{k}), \quad (3.2.6)$$

with $\hat{U}_{\text{BdG}}^k(\bar{\mathcal{T}}) = \text{diag}[\bar{u}^k(\bar{\mathcal{T}}), \bar{u}^{-k}(\bar{\mathcal{T}})^*]$.

Next, we clarify the relations between the symmetry operations. On the mirror plane, the PHS operator satisfies

$$\hat{U}_{\text{BdG}}(\bar{C})\hat{U}_{\text{BdG}}^k(\bar{g})^* = \eta_g \hat{U}_{\text{BdG}}^{-k}(\bar{g})\hat{U}_{\text{BdG}}(\bar{C}), \quad (3.2.7)$$

while $\hat{U}_{\text{BdG}}^k(\bar{\mathcal{M}}_\perp)$, $\hat{U}_{\text{BdG}}^k(\bar{\mathcal{I}})$, and $\hat{U}_{\text{BdG}}^k(\bar{\mathcal{T}})$ satisfy

$$\hat{U}_{\text{BdG}}^k(\bar{\mathcal{I}})\hat{U}_{\text{BdG}}^k(\bar{\mathcal{M}}_\perp) = \exp(-2ik \cdot t_{\mathcal{M}})\hat{U}_{\text{BdG}}^{-k}(\bar{\mathcal{M}}_\perp)\hat{U}_{\text{BdG}}^k(\bar{\mathcal{I}}), \quad (3.2.8a)$$

$$\hat{U}_{\text{BdG}}^k(\bar{\mathcal{T}})\hat{U}_{\text{BdG}}^k(\bar{\mathcal{M}}_\perp)^* = \exp(-2ik_\perp \cdot t_{\mathcal{T}})\hat{U}_{\text{BdG}}^{-k}(\bar{\mathcal{M}}_\perp)\hat{U}_{\text{BdG}}^k(\bar{\mathcal{T}}), \quad (3.2.8b)$$

where we use $\omega_{\text{in}}(\mathcal{I}, \mathcal{M}_\perp) = \omega_{\text{in}}(\mathcal{M}_\perp, \mathcal{I})$, $\omega_{\text{in}}(\mathcal{T}, \mathcal{M}_\perp) = \omega_{\text{in}}(\mathcal{M}_\perp, \mathcal{T})$, and the nonsymmorphic part of factor system $\omega_{\text{ns}}^k(g_1, g_2)$ in Eq. (2.1.11).

A line node in superconducting gaps, in general, appears either at (a) a general position or (b) a high-symmetric plane, *i.e.*, a mirror or glide plane since it occurs on the FS. See Fig. 3.3(a). For the former case, symmetries affecting a line node are the ones keeping the arbitrary position of the line node. Such symmetry operations are given by the PHS-like operator $\mathfrak{C}^k \equiv \hat{U}_{\text{BdG}}(\bar{C})\hat{U}_{\text{BdG}}^k(\bar{\mathcal{I}})^*K$, the TRS-like operator $\mathfrak{T}^k \equiv \hat{U}_{\text{BdG}}^{-k}(\bar{\mathcal{T}})\hat{U}_{\text{BdG}}^k(\bar{\mathcal{I}})^*K$, which are obtained from combinations of the PHS and TRS operators with inversion operators, and the chiral operator $\Gamma^k \equiv i\hat{U}_{\text{BdG}}^{-k}(\bar{\mathcal{T}})\hat{U}_{\text{BdG}}(\bar{C})^*$. Here, K is the complex conjugate and $\eta_{\mathcal{I}}(\mathfrak{C}^k)^2 = -(\mathfrak{T}^k)^2 = (\Gamma^k)^2 = 1$. On the other hand, for the latter case, a line nodes is on a high-symmetric plane, which may be enforced by the mirror reflection operation $\hat{U}_{\text{BdG}}^k(\mathcal{M}_\perp)$. Since $[\hat{U}_{\text{BdG}}^k(\mathcal{M}_\perp)]^2 = -e^{-2ik_\parallel \cdot t_{\mathcal{M}}}$, the sign of the squared operator may also change at the ZF. We conveniently fix the sign by defining $\mathcal{M}^k \equiv e^{ik_\parallel \cdot t_{\mathcal{M}}}\hat{U}_{\text{BdG}}^k(\mathcal{M}_\perp)$ which satisfies $(\mathcal{M}^k)^2 = -1$. Using Eqs. (3.2.7) and (3.2.8), we then obtain the commutation relations,

$$\mathfrak{C}^k \mathcal{M}^k = e^{-2ik_\perp \cdot t_{\mathcal{M}}} \eta_{\mathcal{M}_\perp} \mathcal{M}^k \mathfrak{C}^k, \quad (3.2.9a)$$

$$\Gamma^k \mathcal{M}^k = e^{-2ik_\perp \cdot t_{\mathcal{T}}} \eta_{\mathcal{M}_\perp} \mathcal{M}^k \Gamma^k, \quad (3.2.9b)$$

while the commutation relation between \mathfrak{T}^k and \mathcal{M}^k can be determined from Eq. (3.2.9). The right-hand side of Eq. (3.2.9) may change sign in the BP and the ZF, depending on the action of $[t_{\mathcal{M}}]_\perp$ and $[t_{\mathcal{T}}]_\perp$.

3.2.1 Line node at a general position

As a vortex in the momentum space, the stability of a line node is ensured by a 1D topological number defined on a circle enclosing the line node. However, the PHS-like or TRS-like operator does not give a nonzero 1D topological number, so the CS is required [55–57].¹ Furthermore, since $(\mathfrak{C}^k)^2 = \eta_{\mathcal{I}}$, even-parity superconductors ($\eta_{\mathcal{I}} = 1$) and odd-parity superconductors ($\eta_{\mathcal{I}} = -1$) belong to different Altland-Zirnbauer (AZ) classes [52, 53], and only even-parity superconductors

¹ $\mathcal{T}\mathcal{I}$ symmetry also enables us to define the 1D \mathbb{Z}_2 number, but in the case of superconductors, either \mathcal{T} or \mathcal{I} should be preserved in order for electrons at \mathbf{k} and $-\mathbf{k}$ to form a bulk Cooper pair. Thus, $\mathcal{T}\mathcal{I}$ symmetry implies the presence of \mathcal{T} , which gives chiral symmetry with PHS. The \mathbb{Z}_2 number then reduces to the parity of Eq. (3.2.10).

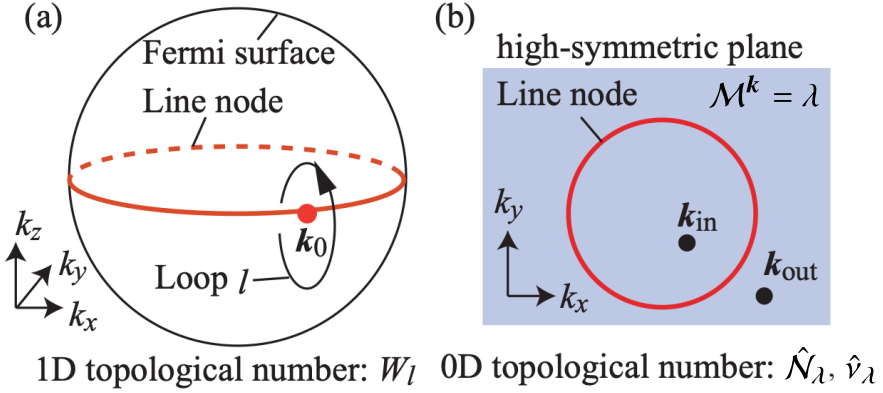


Figure 3.3: (a) When a line node appears at a general position \mathbf{k}_0 , it is encircled by a loop l . (b) On the other hand, if one lies on a high-symmetric plane, two points \mathbf{k}_{in} and \mathbf{k}_{out} encircle it.

can support a non-zero 1D topological number. For even-parity superconductors, the 1D topological number in terms of Γ^k can be defined on a loop l ,

$$W_l = \frac{i}{4\pi} \oint_l d\mathbf{k} \cdot \text{Tr}[\Gamma^k \hat{H}_{\text{BdG}}(\mathbf{k})^{-1} \partial_{\mathbf{k}} \hat{H}_{\text{BdG}}(\mathbf{k})]. \quad (3.2.10)$$

3.2.2 Line node on a high-symmetry plane

We take M^k into account as a symmetry operation relevant to a line node in addition to \mathfrak{C}^k , \mathfrak{T}^k , and Γ^k . On a high-symmetric plane, a line node separates the two-dimensional (2D) BZ into two disjoint regions, which are distinguished by a 0D topological number. See Fig. 3.3(b). For a 0D topological number, we refer to the topological periodic table presented in Refs. [58–63] and regarding \mathfrak{T}^k , \mathfrak{C}^k , and Γ^k in terms of the AZ symmetry. On the mirror plane, the mirror operator commutes with the BdG Hamiltonian and so the BdG Hamiltonian splits into mirror sectors, $\hat{H}_{\text{BdG}} \rightarrow \hat{h}_\lambda \oplus \hat{h}_{-\lambda}$, where λ is an eigenvalue of M^k . Then, Γ^k (\mathfrak{C}^k and \mathfrak{T}^k) exists within the mirror sectors if it (anti)commutes with M^k . For instance, when $[\mathfrak{C}^k, M^k] = \{\mathfrak{T}^k, M^k\} = \{\Gamma^k, M^k\} = 0$, the EAZ symmetry class of each mirror sector is the AII class [$(\mathfrak{T}^k)^2 = -1$] and its 0D topological number is $2\mathbb{Z}$. As such, we have determined the possible 0D topological numbers in the mirror sectors and summarized in Table 3.3. The obtained 0D topological numbers $2\mathbb{Z}$ and \mathbb{Z}_2 of a line node in the mirror sector h_λ can then be defined as

$$\hat{\mathcal{N}}_\lambda = \hat{n}(\mathbf{k}_{\text{out}})_\lambda - \hat{n}(\mathbf{k}_{\text{in}})_\lambda, \quad (3.2.11)$$

$$(-1)^{\hat{\nu}_\lambda} = \text{sgn} \left[\frac{\text{Pf}\{\hat{h}_\lambda(\mathbf{k}_{\text{out}}) L_{\mathbf{k}_{\text{out}}, \lambda}\}}{\text{Pf}\{\hat{h}_\lambda(\mathbf{k}_{\text{in}}) L_{\mathbf{k}_{\text{in}}, \lambda}\}} \right], \quad (3.2.12)$$

respectively, where $\hat{n}(\mathbf{k})_\lambda$ is the number of occupied states with momentum \mathbf{k} , $\mathfrak{C}^k = (L_{\mathbf{k}, \lambda} \oplus L_{\mathbf{k}, -\lambda})K$, and \mathbf{k}_{in} (\mathbf{k}_{out}) is the momentum inside (outside) of the nodal loop. In the weak coupling limit,

Table 3.3: Topology of the symmetry-protected line nodes, labeled by the symbol $M_{g(u)}^{pq}$. The superscripts p, q are defined by $p = e^{-2ik_\perp \cdot t_M} \eta_{\mathcal{M}_\perp}$ and $q = e^{-2ik_\perp \cdot t_T} \eta_{\mathcal{M}_\perp}$, respectively, while the subscript $g(u)$ indicates whether the SC has even (g) or odd (u) parity. The bottom table shows the comparison between Table 3.1 and the 0D topological numbers, where A_g (B_u) and B_g (A_u) in the BP correspond to the $M_{g(u)}^{++}$ and $M_{g(u)}^{--}$ classes, respectively. Cases (2a)-(2d) correspond to those in Table 3.1. The labels (i)-(iii) indicate the SC class of the Majorana flat bands.

Topological No.	M_g^{++}	M_g^{+-}	M_g^{-+}	M_g^{--}	M_u^{++}	M_u^{+-}	M_u^{-+}	M_u^{--}
0D	0	$2\mathbb{Z}$	0	\mathbb{Z}_2	0	$2\mathbb{Z}$	0	0
1D	$2\mathbb{Z}$	$2\mathbb{Z}$	$2\mathbb{Z}$	$2\mathbb{Z}$	0	0	0	0

	A_g		B_g		A_u		B_u	
Cases	BP	ZF	BP	ZF	BP	ZF	BP	ZF
(2a)	0	\rightarrow	0	(ii) \mathbb{Z}_2	\rightarrow	\mathbb{Z}_2	0	\rightarrow
(2b)	(iii) 0	\rightarrow	$2\mathbb{Z}$	(iii) \mathbb{Z}_2	\rightarrow	0	0	(i) 0
(2c)	0	\rightarrow	0	(ii) \mathbb{Z}_2	\rightarrow	$2\mathbb{Z}$	(i) 0	\rightarrow
(2d)	(iii) 0	\rightarrow	\mathbb{Z}_2	(iii) \mathbb{Z}_2	\rightarrow	0	0	\rightarrow

i.e., $\Delta(\mathbf{k}) \rightarrow 0$, Eqs. (3.2.11) and (3.2.12) are directly linked to the FS topology: If we define $\mathcal{N}_\lambda = n(\mathbf{k}_{\text{out}})_\lambda - n(\mathbf{k}_{\text{in}})_\lambda$ in the normal Hamiltonian to be the topological number of the FS in the mirror sector with eigenvalue λ , Eqs. (3.2.11) and (3.2.12) are reduced to

$$\hat{\mathcal{N}}_\lambda = 2\mathcal{N}_\lambda, \quad (3.2.13)$$

$$(-1)^{\hat{\nu}_\lambda} = (-1)^{\mathcal{N}_\lambda}, \quad (3.2.14)$$

which implies that a nodal loop is only topologically stable if $\mathcal{N}_\lambda \neq 0$.

We are now in a position to elucidate the relationship between the group theoretical and topological classifications. The IRs A_g , A_u , B_g , and B_u then correspond to the topological classifications labeled by M_g^{++} , M_u^{--} , M_g^{--} , and M_u^{++} in the BP, where the superscripts of the symbol encode the commutation relations (3.2.9a) and (3.2.9b) and the subscript indicates even (g) or odd (u) parity. Moreover, the mirror symmetry classes in the ZF depend on $[t_M]_\perp$ and $[t_T]_\perp$ due to Eq. (3.2.9). In Tables 3.1 and 3.3, we find a one-to-one correspondence, in which the absence of IRs coincides with the presence of the 0D topological numbers.

3.2.3 Possible Majorana flat bands

Finally, we consider the connection between symmetry-protected line nodes and Majorana flat bands, which are characterized by 0D and 1D topological numbers, respectively. As was discussed

above, the 1D topological number exists only for even-parity superconductors, so do Majorana flat bands. In such even-parity superconductors, the 0D and 1D topological numbers are intrinsically related to each other and satisfy

$$|\hat{\mathcal{N}}_\lambda| = |W_l|, \quad (-1)^{\hat{v}_\lambda} = (-1)^{W_l/2}, \quad (3.2.15)$$

which implies that a symmetry-protected line node is always accompanied by the 1D topological number. We note also that the 1D topological number survives even when the mirror symmetry is broken, which reflects the strong stability of the line nodes.

Using Table 3.3 and Eq. (3.2.15), we can identify three classes with respect to the stability of the line nodes. A line node may be protected by (i) the 0D topological number in odd-parity superconductors with TRS (or a magnetic translation symmetry), or alternatively, by both the 0D and 1D topological numbers in even parity superconductors with (ii) TRS or (iii) a magnetic translation symmetry. We immediately find that there is no Majorana flat band in class (i) superconductors since there is no 1D topological number corresponding to a Majorana flat band in odd-parity superconductors. In order to demonstrate the existence of Majorana flat bands in class (ii) and (iii) superconductors, consider a system with an open boundary, *e.g.*, the $x_i = 0$ plane. Then, an Majorana flat band appears on the $x_i = 0$ plane if the 1D topological number in Eq. (3.2.10) defined on the loop $l(k_j, k_l) = \{(k_i, k_j, k_l) | -\pi \leq k_i \leq \pi\}$ is nonzero [64, 65], where (k_i, k_j, k_l) are perpendicular to each other, and $l(k_j, k_l)$ does not intersect with the line node. For superconductors satisfying the conditions of class (ii), the operator $\bar{\mathcal{T}}$ corresponds to a pure TRS, so $l(k_j, k_l)$ can be defined for arbitrary surface direction. Thus, an Majorana flat band appears on the superconductors' surface in analogy with high- T_c cuprate superconductors [66, 67]. On the other hand, $\bar{\mathcal{T}}$ in class (iii) corresponds to a magnetic translation, so $l(k_j, k_l)$ needs to be compatible with a translation vector $t_{\mathcal{T}}$, *i.e.*, an Majorana flat band only arises when one satisfies $t_{\mathcal{T}} \cdot \hat{e}_i = 0$ for class (iii) superconductors, where \hat{e}_i is a unit vector normal to the surface. Note that the behavior we have outlined here is similar to that of surface states in antiferromagnetic topological insulators [68–75]. Thus, a limitation on possible Majorana flat bands in class (iii) superconductors appears in contrast to Majorana flat bands in class (ii) and noncentrosymmetric superconductors [76–78]. In particular, when $t_{\mathcal{T}}$ is perpendicular to the mirror plane, Majorana flat bands do not exist on any surface because no surface direction simultaneously satisfies the constraints arising from the magnetic translation and the mirror symmetry. Thus, a distortion or interaction that breaks the mirror symmetry is necessary to reveal the hidden Majorana flat bands.

3.3 Example: Sr_2IrO_4 in $- + + -$ state

In this section, we suggest that superconductivity with nonsymmorphic-symmetry-protected gap structures in Table 3.1 appear in the $- + + -$ magnetic state of Sr_2IrO_4 , which is regarded as a higher-order magnetic octupole (MO) order. These results are evidenced by a combination of group theoretical analysis and numerical analysis of an effective $J_{\text{eff}} = 1/2$ model for Sr_2IrO_4 .

3.3.1 Background

A layered perovskite $5d$ transition metal oxide Sr_2IrO_4 has attracted recent attention because a lot of similarities to the high-temperature cuprate superconductors have been recognized. For example, Sr_2IrO_4 (La_2CuO_4) has one hole per Ir (Cu) ion, and shows a pseudospin-1/2 AFM order [79]. Moreover, recent experiments on electron-doped Sr_2IrO_4 indicate the emergence of a pseudogap [80–82] and at low temperatures a d -wave gap [83], which strengthens the analogy with cuprates. Furthermore, d -wave superconductivity in Sr_2IrO_4 by carrier doping is theoretically predicted by several studies [84–87]. Distinct differences of Sr_2IrO_4 from cuprates are large spin-orbit coupling and nonsymmorphic crystal structure, both of which attract interest in the modern condensed matter physics.

Below $T_N \simeq 230$ K, an AFM order develops in undoped Sr_2IrO_4 . Large spin-orbit coupling and rotation of octahedra lead to canted magnetic moments from the a axis and induce a small FM moment along the b axis (Fig. 3.4). Several magnetic structures for stacking along the c axis have been reported in response to circumstances. The magnetic ground states determined by resonant x-ray scattering [88–90], neutron diffraction [91, 92], and second-harmonic generation [93], are summarized in a recent theoretical work [94]. In the undoped compound, the FM component shows the stacking pattern $- + ++$ [88, 89, 91], as illustrated in Fig. 3.4. On the other hand, the $+ + ++$ pattern is suggested as the magnetic structure of Sr_2IrO_4 in a magnetic field directed in the ab plane [88] and of Rh-doped $\text{Sr}_2\text{Ir}_{1-x}\text{Rh}_x\text{O}_4$ [90, 92]. The recent observation [93], however, advocates the $- + --$ magnetic pattern indicating an intriguing odd-parity hidden order in Sr_2IrO_4 (see Fig. 3.4).

The crystal space group of Sr_2IrO_4 was originally reported as $I4_1/acd$ from neutron powder diffraction experiments [95, 96]. Very recently, however, the crystal structure has been revealed by single-crystal neutron diffraction to be rather $I4_1/a$ [92]. In either case, the symmetry of Sr_2IrO_4 is globally centrosymmetric and nonsymmorphic. On the other hand, the site symmetry of the Ir site is S_4 lacking local inversion symmetry. In such noncentrosymmetric systems, antisymmetric spin-orbit coupling (ASOC) entangles various internal degrees of freedom, such as spin, orbital, and sublattice, namely multipole degrees of freedom. As an intriguing consequence of the ASOC, locally noncentrosymmetric systems may realize odd-parity multipole order [97–104] beyond the paradigm of even-parity multipole order in d - and f -electron systems [105].

3.3.2 Classification of $- + ++$ and $- + --$ order based on magnetic multipole

Before going to the main issue, we show that the $- + ++$ and $- + --$ order are classified into a MO and magnetic quadrupole (MQ) order, respectively.

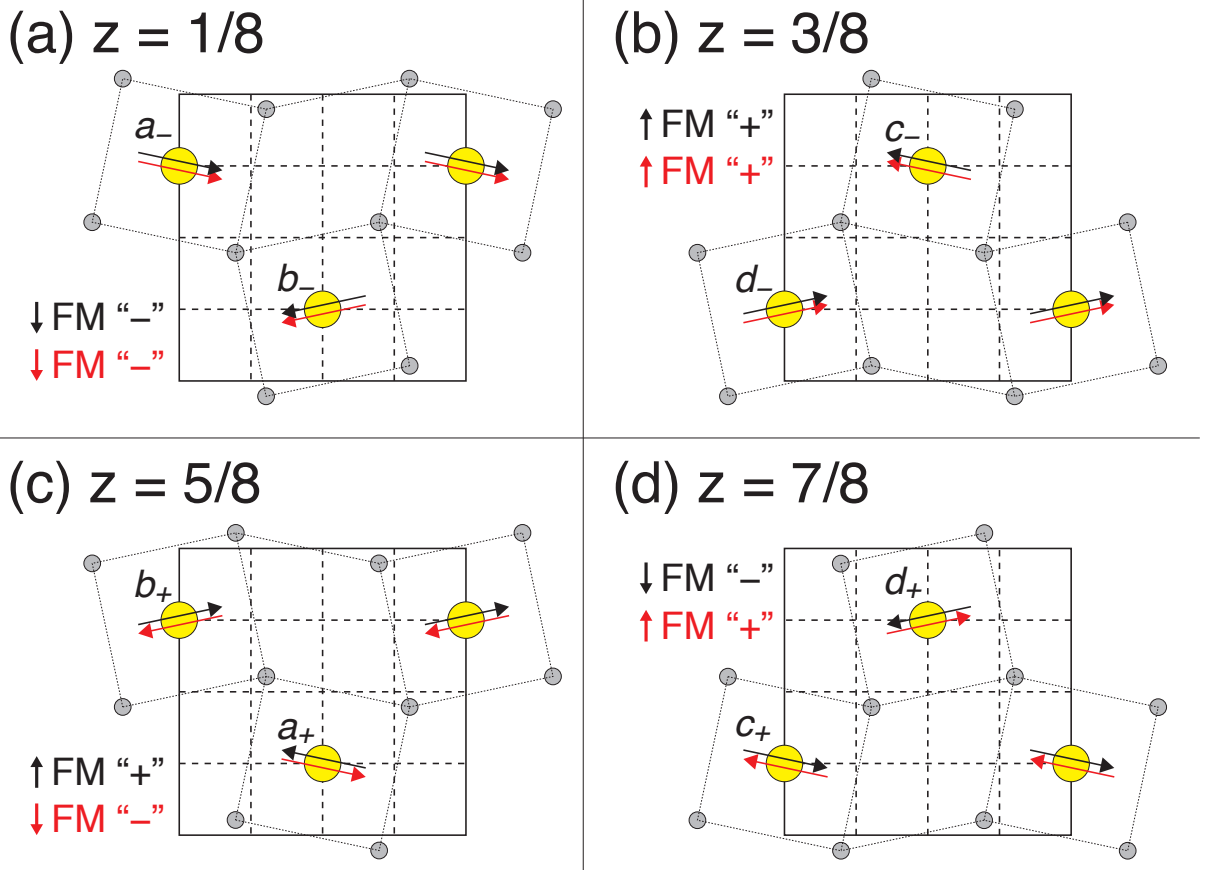


Figure 3.4: Crystal and magnetic symmetries of Sr_2IrO_4 in the 4 IrO_2 planes: (a) $z = \frac{1}{8}$, (b) $z = \frac{3}{8}$, (c) $z = \frac{5}{8}$, and (d) $z = \frac{7}{8}$ [18, 94]. The two magnetic patterns of interest, $- + - +$ (black arrows) and $- - + +$ (red arrows), are shown. They differ by the FM in-plane component along the b axis. Iridium atoms (yellow circles) are labeled as a_- , b_- , c_- , d_- , a_+ , b_+ , c_+ , d_+ .

Table 3.4: Irreducible decomposition of D_{4h} even-parity IRs in D_{2h} point group.

(IRs of D_{4h})	A_{2g}	B_{1g}	B_{2g}	E_g
$(\text{IRs of } D_{4h}) \downarrow D_{2h}$	B_{1g}	A_g	B_{1g}	$B_{2g} + B_{3g}$

Table 3.5: Irreducible decomposition of D_{4h} odd-parity IRs in C_{2v} point group.

(IRs of D_{4h})	A_{1u}	A_{2u}	B_{1u}	B_{2u}	E_u
$(\text{IRs of } D_{4h}) \downarrow C_{2v}$	A_2	B_2	A_2	B_2	$A_1 + B_1$

3.3.2.1 $- + + -$ order

Although the crystal symmetry of Sr_2IrO_4 is D_{4h} , it reduces to D_{2h} in the $- + + -$ ordered state. In Table 3.4, the even-parity IRs of D_{4h} except A_{1g} (A_{2g} , B_{1g} , B_{2g} , and E_g) are subduced to representations of D_{2h} . Since only B_{1g} contains the fully symmetric IR of D_{2h} (A_g), the $- + + -$ order belongs to B_{1g} representation of D_{4h} .

The lowest-order TRS-odd basis function of B_{1g} is $\alpha y s_z + \beta z (y s_x + x s_y)$ in the real space. This basis function represents an even-parity MO ($l = 3$) order [106],

$$\hat{M}_{3,-2} - \hat{M}_{3,2} \propto x y \hat{z} + y z \hat{x} + z x \hat{y}, \quad (3.3.1)$$

$$\hat{M}_{l,m} = \mu_B \sum_{j=1}^n \left(\frac{2l_j}{l+1} + 2s_j \right) \cdot \nabla_j \left(r_j^l Z_{l,m}(\hat{\mathbf{r}}_j)^* \right), \quad (3.3.2)$$

where $Z_{l,m}(\hat{\mathbf{r}}) \equiv \sqrt{\frac{4\pi}{2l+1}} Y_{l,m}(\hat{\mathbf{r}})$ is the normalized spherical harmonics. Thus, the $- + + -$ order is classified into a MO order.

3.3.2.2 $- + - +$ order

In the $- + - +$ ordered state, the crystal symmetry reduces from D_{4h} to C_{2v} . Here, the odd-parity IRs of D_{4h} (A_{1u} , A_{2u} , B_{1u} , B_{2u} , and E_u) are subduced to representations of C_{2v} (Table 3.5). Since only E_u contains the fully symmetric IR of C_{2v} (A_1), the $- + - +$ order belongs to E_u representation of D_{4h} .

This IR E_u permits TRS-odd basis functions: $\alpha y s_z + \beta z s_y$ in the real space, and k_x in the momentum space. In the real space, the basis function contains an odd-parity MQ ($l = 2$) order [106],

$$\hat{M}_{2,1} + \hat{M}_{2,-1} \propto y \hat{z} + z \hat{y}. \quad (3.3.3)$$

Table 3.6: The gap structure for A_{1g} and B_{2g} gap functions.

Order parameter	$k_z = 0$	$k_z = \pi/c$	$k_{x,y} = 0$	$k_{x,y} = \pi/a$
A_{1g} (<i>s</i> -wave)	gap	node	gap	node
B_{2g} (d_{xy} -wave)	gap	node	node	gap

Therefore, the $-+--$ order contains the component of a MQ order, though it may include a toroidal dipole order proportional to $y\hat{z} - z\hat{y}$ [97].

3.3.3 Classification

Now we consider the superconductivity in the $-++-$ state.² The magnetic space group of the $-++-$ state is a nonsymmorphic group $P_{Icc}\bar{a} = Pcc\bar{a} + \{T|\frac{\hat{x}}{2} + \frac{\hat{y}}{2} + \frac{\hat{z}}{2}\}Pcc\bar{a}$. We especially focus on the Cooper pairs on the mirror-invariant BPs $k_{z,x,y} = 0$ and the ZFs $k_z = \pi/c$ and $k_{x,y} = \pi/a$. By using Tables 3.1 and 3.2, we can calculate the character of the Cooper pair wave functions $\bar{P}^k \uparrow D_{4h}$, and then decompose it into IRs of the original crystal symmetry D_{4h} . The obtained results are summarized in the following:

- On the horizontal planes $k_z = 0$ and π/c ,

$$\bar{P}^k \uparrow D_{4h} = \begin{cases} A_{1g} + A_{2g} + B_{1g} + B_{2g} + 2A_{1u} + 2A_{2u} + 2B_{1u} + 2B_{2u} + 2E_u & \text{BP}, \\ 2E_g + A_{1u} + A_{2u} + B_{1u} + B_{2u} + 4E_u & \text{ZF}; \end{cases} \quad (3.3.4)$$

- On the vertical planes $k_{x,y} = 0$ and π/a ,

$$\bar{P}^k \uparrow D_{4h} = \begin{cases} A_{1g} + B_{1g} + E_g + 2A_{1u} + A_{2u} + 2B_{1u} + B_{2u} + 3E_u & \text{BP}, \\ A_{2g} + B_{2g} + E_g + 3A_{1u} + 3B_{1u} + 3E_u & \text{ZF}. \end{cases} \quad (3.3.5)$$

We find that possible IRs change from BPs to ZFs as a consequence of the nonsymmorphic symmetry. The gap functions should be zero, and thus, the gap nodes appear, if the corresponding IRs do not exist in these results of reductions [5, 7, 51]. Otherwise, the superconducting gap will open in general. From Eqs. (3.3.4) and (3.3.5), for instance, we find the gap structure of A_{1g} and B_{2g} superconducting states summarized in Table 3.6.

3.3.4 Numerical calculation

We demonstrate the results of group theory (Table 3.6) using an effective model for $J_{\text{eff}} = 1/2$ manifold.

²In this thesis, we do not discuss the FFLO superconductivity in the $-+--$ state [18], because it digresses from the main subject.

3.3.4.1 Model

We introduce a 3D single-orbital tight-binding model describing superconductivity coexisting with magnetic order in Sr_2IrO_4 ,

$$H_{\text{BdG}} = \frac{1}{2} \sum_{\mathbf{k}} \mathbf{C}^\dagger(\mathbf{k}) \hat{H}_{\text{BdG}}(\mathbf{k}) \mathbf{C}(\mathbf{k}), \quad (3.3.6)$$

where

$$\begin{aligned} \mathbf{C}^\dagger(\mathbf{k}) = & (a_{-\uparrow}^\dagger(\mathbf{k}_+), a_{-\downarrow}^\dagger(\mathbf{k}_+), \dots, d_{-\uparrow}^\dagger(\mathbf{k}_+), d_{-\downarrow}^\dagger(\mathbf{k}_+), \\ & a_{+\uparrow}^\dagger(\mathbf{k}_+), a_{+\downarrow}^\dagger(\mathbf{k}_+), \dots, d_{+\uparrow}^\dagger(\mathbf{k}_+), d_{+\downarrow}^\dagger(\mathbf{k}_+), \\ & a_{-\uparrow}^\dagger(\mathbf{k}_-), a_{-\downarrow}^\dagger(\mathbf{k}_-), \dots, d_{-\uparrow}^\dagger(\mathbf{k}_-), d_{-\downarrow}^\dagger(\mathbf{k}_-), \\ & a_{+\uparrow}^\dagger(\mathbf{k}_-), a_{+\downarrow}^\dagger(\mathbf{k}_-), \dots, d_{+\uparrow}^\dagger(\mathbf{k}_-), d_{+\downarrow}^\dagger(\mathbf{k}_-)), \end{aligned} \quad (3.3.7)$$

with $\mathbf{k}_+ \equiv \mathbf{k} + \frac{\mathbf{q}}{2}$, $\mathbf{k}_- \equiv -\mathbf{k} + \frac{\mathbf{q}}{2}$ are 32-dimensional vector of creation-annihilation operators. The center-of-mass momentum \mathbf{q} of Cooper pairs is assumed to be zero in most cases except for the studies of FFLO state [18]. We define $a_{\pm s}^\dagger(\mathbf{k}), \dots, d_{\pm s}^\dagger(\mathbf{k})$ as the creation operators of electrons with spin $s = \uparrow, \downarrow$ on the sublattices a_\pm, \dots, d_\pm , respectively (see Fig. 3.4 for the sublattices). The 32×32 BdG Hamiltonian is described with use of the normal state Hamiltonian $\hat{H}_n(\mathbf{k})$ and the order parameter part $\hat{\Delta}(\mathbf{k})$,

$$\hat{H}_{\text{BdG}}(\mathbf{k}) = \begin{pmatrix} \hat{H}_n(\mathbf{k}_+) & \hat{\Delta}(\mathbf{k}) \\ \hat{\Delta}(\mathbf{k})^\dagger & -\hat{H}_n^T(\mathbf{k}_-) \end{pmatrix}, \quad (3.3.8)$$

where

$$\hat{H}_n(\mathbf{k}) = \hat{H}_{\text{kin}}(\mathbf{k}) + \hat{H}_{\text{ASOC}}(\mathbf{k}) + \hat{H}_{\text{MO}}. \quad (3.3.9)$$

The kinetic term $\hat{H}_{\text{kin}}(\mathbf{k})$ is given by the following equation:

$$\hat{H}_{\text{kin}}(\mathbf{k}) = \left[\begin{array}{c|c} \hat{H}_{\text{intra-layer}}(\mathbf{k}) & \hat{H}_{\text{inter-layer2}}(\mathbf{k}) \\ \hline +\hat{H}_{\text{inter-layer1}}(\mathbf{k}) & \hat{H}_{\text{intra-layer}}(\mathbf{k}) \\ \hline \hat{H}_{\text{inter-layer2}}(\mathbf{k})^\dagger & +\hat{H}_{\text{inter-layer1}}(\mathbf{k}) \end{array} \right], \quad (3.3.10)$$

where

$$\hat{H}_{\text{intra-layer}}(\mathbf{k}) = \sigma_0^{(\text{layer})} \otimes [(\varepsilon_2(\mathbf{k}) - \mu) \sigma_0^{(\text{sl})} \otimes \sigma_0^{(\text{spin})} + \varepsilon_1(\mathbf{k}) \sigma_x^{(\text{sl})} \otimes \sigma_0^{(\text{spin})}], \quad (3.3.11)$$

$$\begin{aligned} \hat{H}_{\text{inter-layer1}}(\mathbf{k}) = & \sigma_x^{(\text{layer})} \otimes [\text{Re}(\varepsilon_3^x(\mathbf{k})) \sigma_0^{(\text{sl})} \otimes \sigma_0^{(\text{spin})} + \text{Re}(\varepsilon_3^y(\mathbf{k})) \sigma_x^{(\text{sl})} \otimes \sigma_0^{(\text{spin})}] \\ & - \sigma_y^{(\text{layer})} \otimes [\text{Im}(\varepsilon_3^x(\mathbf{k})) \sigma_0^{(\text{sl})} \otimes \sigma_0^{(\text{spin})} + \text{Im}(\varepsilon_3^y(\mathbf{k})) \sigma_x^{(\text{sl})} \otimes \sigma_0^{(\text{spin})}], \end{aligned} \quad (3.3.12)$$

$$\begin{aligned} \hat{H}_{\text{inter-layer2}}(\mathbf{k}) = & \sigma_x^{(\text{layer})} \otimes [\text{Re}(\varepsilon_3^y(\mathbf{k})) \sigma_0^{(\text{sl})} \otimes \sigma_0^{(\text{spin})} + \text{Re}(\varepsilon_3^x(\mathbf{k})) \sigma_x^{(\text{sl})} \otimes \sigma_0^{(\text{spin})}] \\ & + \sigma_y^{(\text{layer})} \otimes [\text{Im}(\varepsilon_3^y(\mathbf{k})) \sigma_0^{(\text{sl})} \otimes \sigma_0^{(\text{spin})} + \text{Im}(\varepsilon_3^x(\mathbf{k})) \sigma_x^{(\text{sl})} \otimes \sigma_0^{(\text{spin})}], \end{aligned} \quad (3.3.13)$$

with the chemical potential μ . $\sigma_i^{(\text{spin})}$, $\sigma_i^{(\text{sl})}$, and $\sigma_i^{(\text{layer})}$ are the Pauli matrices representing the spin, sublattice, and layer degrees of freedom, respectively. The single electron kinetic energy terms $\varepsilon_1(\mathbf{k})$, $\varepsilon_2(\mathbf{k})$, and $\varepsilon_3^{x,y}(\mathbf{k})$ are described by taking into account the nearest-, next-nearest-, and third-nearest-neighbor hoppings,

$$\varepsilon_1(\mathbf{k}) = -4t_1 \cos \frac{k_x a}{2} \cos \frac{k_y a}{2}, \quad (3.3.14)$$

$$\varepsilon_2(\mathbf{k}) = -2t_2(\cos(k_x a) + \cos(k_y a)), \quad (3.3.15)$$

$$\varepsilon_3^x(\mathbf{k}) = -t_3 \cos \frac{k_x a}{2} e^{-ik_z c/4}, \quad (3.3.16)$$

$$\varepsilon_3^y(\mathbf{k}) = -t_3 \cos \frac{k_y a}{2} e^{-ik_z c/4}. \quad (3.3.17)$$

For our results in the $-+--$ state [18], the violation of local inversion symmetry which induces the staggered ASOC, $\hat{H}_{\text{ASOC}}(\mathbf{k})$, plays an essential role.³ This term is given by the following matrix:

$$\hat{H}_{\text{ASOC}}(\mathbf{k}) = \left[\begin{array}{c|c} \hat{H}_{\text{ASOC-intra1}}(\mathbf{k}) & \hat{H}_{\text{ASOC-inter}}^x(\mathbf{k}) \\ +\hat{H}_{\text{ASOC-intra2}}(\mathbf{k}) & \\ +\hat{H}_{\text{ASOC-inter}}^y(\mathbf{k}) & \\ \hline \hat{H}_{\text{ASOC-inter}}^x(\mathbf{k})^\dagger & \hat{H}_{\text{ASOC-intra1}}(\mathbf{k}) \\ & +\hat{H}_{\text{ASOC-intra2}}(\mathbf{k}) \\ & +\hat{H}_{\text{ASOC-inter}}^y(\mathbf{k}) \end{array} \right]. \quad (3.3.18)$$

We take into account two intra-layer terms $\hat{H}_{\text{ASOC-intra1}}(\mathbf{k})$, $\hat{H}_{\text{ASOC-intra2}}(\mathbf{k})$ and two inter-layer terms $\hat{H}_{\text{ASOC-inter}}^{x,y}(\mathbf{k})$:

$$\hat{H}_{\text{ASOC-intra1}}(\mathbf{k}) = i\alpha_1 \cos \frac{k_x a}{2} \cos \frac{k_y a}{2} \sigma_0^{(\text{layer})} \otimes i\sigma_y^{(\text{sl})} \otimes \sigma_z^{(\text{spin})}, \quad (3.3.19)$$

$$\hat{H}_{\text{ASOC-intra2}}(\mathbf{k}) = \alpha_2 \sigma_z^{(\text{layer})} \otimes \sigma_z^{(\text{sl})} \otimes (\sin(k_x a) \cos(k_y a) \sigma_x^{(\text{spin})} - \sin(k_y a) \cos(k_x a) \sigma_y^{(\text{spin})}), \quad (3.3.20)$$

³The ASOC is derived from atomic LS coupling [107, 108]. In our effective $J_{\text{eff}} = 1/2$ model, therefore, the ASOC takes account of the effect of LS-type SOC. Since multiorbital electronic structure does not play any essential role in our results, we will obtain qualitatively the same results in the $5d$ multiorbital model.

$$\hat{H}_{\text{ASOC-inter}}^x(\mathbf{k}) = -\alpha_3 \left[i\sigma_y^{(\text{layer})} \otimes i\sigma_y^{(\text{sl})} \otimes \left(\cos \frac{k_z c}{4} \sin \frac{k_x a}{2} \sigma_x^{(\text{spin})} - 2 \sin \frac{k_z c}{4} \cos \frac{k_x a}{2} \sigma_z^{(\text{spin})} \right) \right. \\ \left. + i \cdot \sigma_x^{(\text{layer})} \otimes i\sigma_y^{(\text{sl})} \otimes \left(\sin \frac{k_z c}{4} \sin \frac{k_x a}{2} \sigma_x^{(\text{spin})} + 2 \cos \frac{k_z c}{4} \cos \frac{k_x a}{2} \sigma_z^{(\text{spin})} \right) \right], \quad (3.3.21)$$

$$\hat{H}_{\text{ASOC-inter}}^y(\mathbf{k}) = \alpha_3 \left[i\sigma_y^{(\text{layer})} \otimes i\sigma_y^{(\text{sl})} \otimes \left(\cos \frac{k_z c}{4} \sin \frac{k_y a}{2} \sigma_y^{(\text{spin})} - 2 \sin \frac{k_z c}{4} \cos \frac{k_y a}{2} \sigma_z^{(\text{spin})} \right) \right. \\ \left. - i \cdot \sigma_x^{(\text{layer})} \otimes i\sigma_y^{(\text{sl})} \otimes \left(\sin \frac{k_z c}{4} \sin \frac{k_y a}{2} \sigma_y^{(\text{spin})} + 2 \cos \frac{k_z c}{4} \cos \frac{k_y a}{2} \sigma_z^{(\text{spin})} \right) \right], \quad (3.3.22)$$

which are allowed by the crystal symmetry of Sr_2IrO_4 .

The last term in Eq. (3.3.9), \hat{H}_{MO} , expresses the molecular field of magnetic order, $- + + -$ and $- + - +$. This term causes various superconducting phenomena, which have been demonstrated in this section. As shown in Fig. 3.4, each site has the in-plane magnetic moment. Thus, the molecular field is given by

$$\hat{H}_{\text{MO}} = \begin{bmatrix} -\mathbf{h}(\theta_{a-}) \cdot \boldsymbol{\sigma} & & & \\ & \ddots & & \\ & & \ddots & \\ & & & -\mathbf{h}(\theta_{d+}) \cdot \boldsymbol{\sigma} \end{bmatrix}, \quad (3.3.23)$$

where

$$(\theta_{a-}, \dots, \theta_{d-}, \theta_{a+}, \dots, \theta_{d+}) = \begin{cases} (348^\circ, 192^\circ, 168^\circ, 12^\circ, 168^\circ, 12^\circ, 348^\circ, 192^\circ) & (- + + - \text{ state}) \\ (348^\circ, 192^\circ, 168^\circ, 12^\circ, 348^\circ, 192^\circ, 168^\circ, 12^\circ) & (- + - + \text{ state}), \end{cases} \quad (3.3.24)$$

and $\mathbf{h}(\theta) = h(\cos \theta, \sin \theta, 0)$ [94].

Next we describe the order parameter $\hat{\Delta}(\mathbf{k})$. When the on-site s -wave superconductivity is assumed, it takes the form

$$\hat{\Delta}^{(s)}(\mathbf{k}) = \Delta_0 \hat{\mathbf{1}}_2 \otimes \sigma_0^{(\text{layer})} \otimes \sigma_0^{(\text{sl})} \otimes i\sigma_y^{(\text{spin})}. \quad (3.3.25)$$

For the d_{xy} -wave superconductivity originating from the interaction between the nearest-neighbor sites, we obtain

$$\hat{\Delta}^{(d)}(\mathbf{k}) = \Delta_0 \sin \frac{k_x a}{2} \sin \frac{k_y a}{2} \hat{\mathbf{1}}_2 \otimes \sigma_0^{(\text{layer})} \otimes \sigma_x^{(\text{sl})} \otimes i\sigma_y^{(\text{spin})}. \quad (3.3.26)$$

Finally, we show the parameters which are used in this section. We adopt the hopping parameters of the effective $J_{\text{eff}} = 1/2$ model [85] derived from the three-orbital Hubbard model, where the hopping parameters are $t_1 = 1$, $t_2 = 0.26$, and $t_3 = 0.1$. We here assume moderate ASOCs $\alpha_1 = 0.3$ and $\alpha_2 = \alpha_3 = 0.1$ so that the effects of ASOCs are visible in the numerical results. Since the superconductivity has been predicted at the electron density around $n \sim 1.2$ [85], we determine the

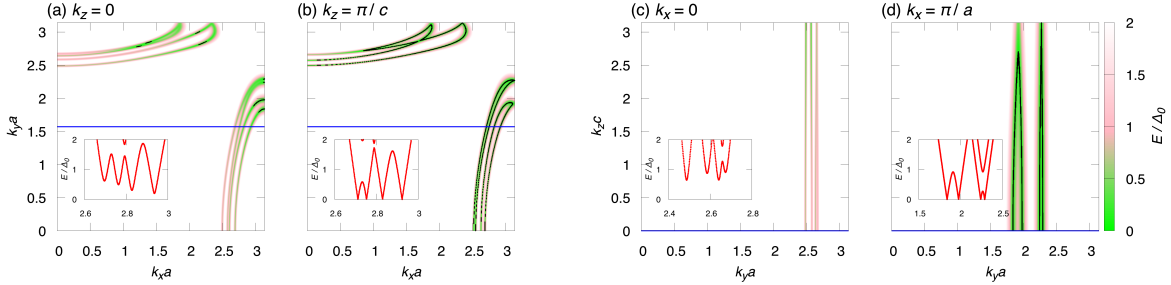


Figure 3.5: The contour plot of quasiparticle energy dispersion E in the s -wave superconducting state normalized by the order parameter Δ_0 on (a) $k_z = 0$, (b) $k_z = \pi/c$, (c) $k_x = 0$, and (d) $k_x = \pi/a$. The insets in (a), (b), (c), and (d) show the dispersion E/Δ_0 along the respective blue line. Line nodes (black lines) appear on the ZF, $k_z = \pi/c$ and $k_x = \pi/a$.

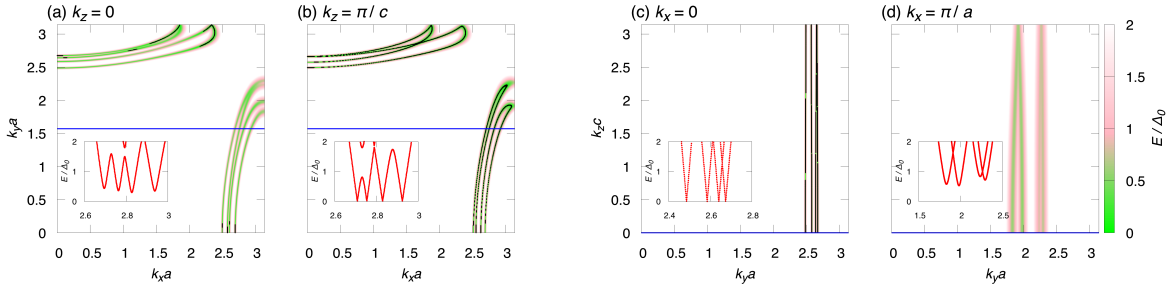


Figure 3.6: The contour plot of quasiparticle energy dispersion E/Δ_0 for the d_{xy} -wave order parameter on (a) $k_z = 0$, (b) $k_z = \pi/c$, (c) $k_x = 0$, and (d) $k_x = \pi/a$. The insets show E/Δ_0 along the respective blue line. Line nodes (black lines) appear on the ZF $k_z = \pi/c$ and the BP $k_x = 0$.

chemical potential $\mu = 1.05$ so as to be consistent with the electron density. Then, four spinful energy bands cross the Fermi level. The magnitude of gap function is chosen to be $\Delta_0 = 0.02$. The conclusions of this section are not altered by the choice of parameters, because they are evidenced by the group theoretical analysis.

3.3.4.2 Results

Now we show the numerical results of the model introduced in the previous section. By diagonalizing the BdG Hamiltonian [Eq. (3.3.8)], the quasiparticle energy dispersion in the superconducting state $E = E(k_x, k_y, k_z)$ is obtained. The results are shown in Figs. 3.5 and 3.6. Only $0 \leq E/\Delta_0 < 2$ region is colored, and especially nodal ($E \sim 0$) points are plotted by black.

The gap structure of the two superconducting states reproduces Table 3.6. In both s -wave and d_{xy} -wave cases, the numerical results are consistent with the group theory. In other words, the gap nodes in Figs. 3.5 and 3.6 are protected by nonsymmorphic space group symmetry. Note that exceptional cases of the gap classification in Table 3.6 appear in some accidentally degenerate

region [13]. For example, we see such unexpected gap structures on the $k_y = \pi/a$ plane.

As introduced previously, both theory [84–87] and experiment [83] suggest d_{xy} -wave superconductivity analogous to cuprates⁴. In this case, a horizontal line node appears on the ZF ($k_z = \pi/c$) in contrast to the usual d_{xy} -wave state. Moreover, the gap opening at the other ZFs ($k_{x,y} = \pi/a$) is also nontrivial because the usual d_{xy} -wave order parameter vanishes not only at BPs but also at ZFs. These nontrivial gap structures are protected by the nonsymmorphic space group symmetry.

⁴Because of the $\pi/4$ rotation of a principle axis, the d_{xy} -wave superconductivity corresponds to the $d_{x^2-y^2}$ -wave state in cuprates.

Chapter 4

Superconducting gap classification on high-symmetry lines

In Chapter 3, the condition for nontrivial line nodes beyond the Sigrist-Ueda method has been elucidated by using the gap classification on high-symmetry \mathbf{k} planes. In this Chapter, on the other hand, we show nontrivial symmetry-protected gap structures using the gap classification on high-symmetry \mathbf{k} lines, namely the n -fold rotational axes ($n = 2, 3, 4$, and 6). In the following part, nonsymmorphic symmetry may not play any important role,¹ and thus, we consider symmorphic space groups and the PM state, for simplicity. In Secs. 4.1 and 4.2, we present the general classification table on high-symmetry axes using group theory and topology, respectively. Furthermore, some candidate superconductors are shown: UPt₃ (Sec. 4.3), SrPtAs (Sec. 4.4), CeCoIn₅ (Sec. 4.5), UCoGe (Sec. 4.6), MoS₂ (Sec. 4.7), UBe₁₃ (Sec. 4.8), and PrOs₄Sb₁₂ (Sec. 4.9).

4.1 Group-theoretical classification

The magnetic little group on a n -fold axis \mathcal{M}_n^k is given by

$$\mathcal{M}_n^k = \mathcal{G}_n^k + \mathfrak{T}\mathcal{G}_n^k = \sum_{m=0}^{n-1} \{C_n|\mathbf{0}\}^m \mathbb{T} + \mathfrak{T} \sum_{m=0}^{n-1} \{C_n|\mathbf{0}\}^m \mathbb{T}, \quad (4.1.1)$$

where C_n represents the n -fold rotation. The small corepresentations of \mathcal{M}_n^k are obtained by the double-valued IR of corresponding point groups (little cogroups) $C_n \cong \mathcal{G}_n^k / \mathbb{T}$ [Tables 4.1(a)-(d)]. Note that each IR in Table 4.1 is composed of two 1D representations, which are degenerate due to the successive operations of time-reversal and spatial inversion $\mathfrak{T} = \{TI|\mathbf{0}\}$. The subscripts 1/2,

¹The results in Table 4.2 are not changed even when the system has non-primitive translations parallel to the n -fold axis, because the phase factor arising from the translations is canceled during calculation of the Mackey-Bradley theorem.

Table 4.1: The double-valued IRs of cyclic point groups [38, 45, 109].

(a) Twofold axis			(b) Threefold axis								
C_2	E	C_2	C_3	E	C_3	C_3^2					
$E_{1/2}$	2	0	$E_{1/2}$	2	1	-1					
			$2B_{3/2}$	2	-2	2					
(c) Fourfold axis				(d) Sixfold axis							
C_4	E	C_4	C_4^3	C_4^2	C_6	E	C_6	C_6^5	C_3	C_3^2	C_2
$E_{1/2}$	2	$\sqrt{2}$	$-\sqrt{2}$	0	$E_{1/2}$	2	$\sqrt{3}$	$-\sqrt{3}$	1	-1	0
$E_{3/2}$	2	$-\sqrt{2}$	$\sqrt{2}$	0	$E_{5/2}$	2	$-\sqrt{3}$	$\sqrt{3}$	1	-1	0
					$E_{3/2}$	2	0	0	-2	2	0

$3/2$, and $5/2$ correspond to the total angular momentum of the Bloch state $j_z = \pm 1/2$, $\pm 3/2$, and $\pm 5/2$, respectively [38, 109].

In some other cases, more generally, a high-symmetry axis in the BZ has a vertical mirror symmetry where the mirror plane contains the axis. Therefore, the general magnetic little cogroup is $\bar{\mathcal{M}}^k = C_{n(v)} + \mathfrak{T}C_{n(v)}$. From the small corepresentation corresponding to the Bloch wave function, we can calculate \bar{P}_α^k , the representation of the Cooper pair wave function, using the Mackey-Bradley theorem [Eq. (2.2.1)]. The obtained results of \bar{P}_α^k are summarized in Table 4.2.

As shown in Table 4.2, the pair wave function on $C_{2(v)}$ - and $C_{4(v)}$ -symmetric lines has a unique representation irrespective of the IR α , namely the total angular momentum of the normal Bloch state. On $C_{3(v)}$ - and $C_{6(v)}$ -symmetric axes, on the other hand, there are two nonequivalent representations of the pair wave function depending on the angular momentum j_z . For example, on the threefold axis, the E_u order parameter is allowed (forbidden) in the case of the $E_{1/2}$ ($2B_{3/2}$) Bloch state. This means that the E_u superconducting gap opens in the energy band of the $j_z = \pm 1/2$ state, while nodes appear for $j_z = \pm 3/2$. Therefore, the presence or absence of nodes is j_z -dependent when the system has threefold or sixfold rotational symmetry. In this thesis, we call it a j_z -dependent gap structure, which is not obtained by the Sigrist-Ueda method [4].

4.2 Topological classification

As revealed in Sec. 2.3, the gap (node) on high-symmetry k -points is represented by the absence (presence) of a topological number in the classification by the EAZ symmetry class. Similarly, we can classify all superconducting gap structures on C_n - or C_{nv} -symmetric lines in the BZ, which are summarized in Table 4.3. Note that the EAZ classes in the table are *not* equal to the AZ symmetry

Table 4.2: Group-theoretical classification of superconducting gap on high-symmetry lines where the little cogroup is $\bar{\mathcal{G}}^k$. \bar{P}_α^k on each line is decomposed by IRs of corresponding $\bar{\mathcal{G}}_{\text{pair}}^k = \bar{\mathcal{G}}^k + \mathcal{I}\bar{\mathcal{G}}^k$. The labels of IR (α) are represented by the subscripts 1/2, 3/2, and 5/2.

$\bar{\mathcal{G}}^k (\bar{\mathcal{G}}_{\text{pair}}^k)$	$\bar{\lambda}_\alpha^k$	\bar{P}_α^k
$C_2 (C_{2h})$	$E_{1/2}$	$A_g + A_u + 2B_u$
$C_3 (S_6)$	$E_{1/2}$	$A_g + A_u + E_u$
	$2B_{3/2}$	$A_g + 3A_u$
$C_4 (C_{4h})$	$E_{1/2}, E_{3/2}$	$A_g + A_u + E_u$
$C_6 (C_{6h})$	$E_{1/2}, E_{5/2}$	$A_g + A_u + E_{1u}$
	$E_{3/2}$	$A_g + A_u + 2B_u$
$C_{2v} (D_{2h})$	$E_{1/2}$	$A_g + A_u + B_{2u} + B_{3u}$
$C_{3v} (D_{3d})$	$E_{1/2}$	$A_{1g} + A_{1u} + E_u$
	$E_{3/2}$	$A_{1g} + 2A_{1u} + A_{2u}$
$C_{4v} (D_{4h})$	$E_{1/2}, E_{3/2}$	$A_{1g} + A_{1u} + E_u$
$C_{6v} (D_{6h})$	$E_{1/2}, E_{5/2}$	$A_{1g} + A_{1u} + E_{1u}$
	$E_{3/2}$	$A_{1g} + A_{1u} + B_{1u} + B_{2u}$

classes of the *total* BdG Hamiltonian, but represent the symmetry of the Hamiltonian decomposed by the IRs of $\bar{\mathcal{G}}^k$. From Table 4.3, we can identify whether the superconducting gap closes or not on *almost all the high-symmetric axes* with some exceptions² by determining the IR of the normal Bloch state and that of the superconducting order parameter.

Now we remark the treatment of the 2D IRs in Table 4.3. A general 2D superconducting order parameter matrix has the form $\hat{\Delta}(\mathbf{k}) = \eta_+ \hat{\Delta}_+(\mathbf{k}) + \eta_- \hat{\Delta}_-(\mathbf{k})$; for example, we consider a superconducting order parameter belonging to the E_g IR of C_3 , for which

$$C_3 \hat{\Delta}_\pm(\mathbf{k}) C_3^T = e^{\pm i 2\pi/3} \hat{\Delta}_\pm(\mathbf{k}), \quad (4.2.1)$$

on the C_3 -symmetric line. For arbitrary parameters η_+ and η_- , however, it is impossible to determine a commutation relation between the rotation symmetry C_3 and the PHS C . On the other hand, if we choose the 1D order parameter with one of the two rotation-invariant bases $\hat{\Delta}(\mathbf{k}) = \hat{\Delta}_\pm(\mathbf{k})$, namely $(\eta_+, \eta_-) = (1, 0)$ or $(0, 1)$, the commutation can be given by

$$\omega_{\text{in}}(C_3, C) = e^{\pm i 2\pi/3} \omega_{\text{in}}(C, C_3). \quad (4.2.2)$$

In other words, $\hat{\Delta}(\mathbf{k}) = \hat{\Delta}_+(\mathbf{k})$ ($\hat{\Delta}_-(\mathbf{k})$) belongs to the 1D IR 2E_g (1E_g) of S_6 [see Table 4.4(a)].

²For example, the gap classification on a C_{2v} -symmetric hinge of the BZ with *glide symmetry* is different from that of Table 4.3(e) with mirror symmetry [110].

Table 4.3: Topological classification of gap structures on high-symmetry lines in the BZ. Each classification is represented by the type of the topological number and the gap structure on the line: (G) full gap, (P) point nodes, (L) a part of line nodes, and (S) a part of surface nodes (Bogoliubov FSs). In a spontaneously TRS breaking phase, since all 2D IRs are decomposed into the 1D IRs with different eigenvalues of the rotation symmetry (see also Table 4.4), the IRs in D_{3d} , D_{4h} , and D_{6h} are the same as those in S_6 , C_{4h} , and C_{6h} , respectively. Therefore we do not show the 2D IRs in the tables (f), (g), and (h).

(a) $\bar{\mathcal{G}}^k = C_2, \alpha = \pm 1/2$			(b1) $\bar{\mathcal{G}}^k = C_3, \alpha = +[-]1/2$			(b2) $\bar{\mathcal{G}}^k = C_3, \alpha = \pm 3/2$		
IR of C_{2h}	EAZ	Classification	IR of S_6	EAZ	Classification	IR of S_6	EAZ	Classification
A_g	AIII	0 (G)	A_g	AIII	0 (G)	A_g	DIII	0 (G)
A_u	AIII	0 (G)	A_u	AIII	0 (G)	A_u	CII	0 (G)
B_g	D	\mathbb{Z}_2 (L)	${}^2E_g[{}^1E_g]$	D	\mathbb{Z}_2 (S)	${}^{1,2}E_g$	A	\mathbb{Z} (S)
B_u	C	0 (G)	${}^1E_g[{}^2E_g]$	A	\mathbb{Z} (S)	${}^2E_u[{}^1E_u]$	C	0 (G)
			${}^2E_u[{}^1E_u]$	C	0 (G)	${}^{1,2}E_u$	A	\mathbb{Z} (P)
			${}^1E_u[{}^2E_u]$	A	\mathbb{Z} (P)			
(c) $\bar{\mathcal{G}}^k = C_4, \alpha = +[-]1/2, +[-]3/2$			(d1) $\bar{\mathcal{G}}^k = C_6, \alpha = +[-]1/2, +[-]5/2$			(d2) $\bar{\mathcal{G}}^k = C_6, \alpha = \pm 3/2$		
IR of C_{4h}	EAZ	Classification	IR of C_{6h}	EAZ	Classification	IR of C_{6h}	EAZ	Classification
A_g	AIII	0 (G)	A_g	AIII	0 (G)	A_g	AIII	0 (G)
A_u	AIII	0 (G)	A_u	AIII	0 (G)	A_u	AIII	0 (G)
B_g	A	\mathbb{Z} (L)	B_g	A	\mathbb{Z} (L)	B_g	D	\mathbb{Z}_2 (L)
B_u	A	\mathbb{Z} (P)	B_u	A	\mathbb{Z} (P)	B_u	C	0 (G)
${}^2E_g[{}^1E_g]$	D	\mathbb{Z}_2 (S)	${}^1E_{1g}[{}^2E_{1g}]$	D	\mathbb{Z}_2 (S)	${}^{1,2}E_{1g}$	A	\mathbb{Z} (S)
${}^1E_g[{}^2E_g]$	A	\mathbb{Z} (S)	${}^2E_{1g}[{}^1E_{1g}]$	A	\mathbb{Z} (S)			
${}^2E_u[{}^1E_u]$	C	0 (G)	${}^1E_{1u}[{}^2E_{1u}]$	C	0 (G)	${}^{1,2}E_{1u}$	A	\mathbb{Z} (P)
${}^1E_u[{}^2E_u]$	A	\mathbb{Z} (P)	${}^2E_{1u}[{}^1E_{1u}]$	A	\mathbb{Z} (P)	${}^{1,2}E_{2g}$	A	\mathbb{Z} (S)
			${}^{1,2}E_{2g}$	A	\mathbb{Z} (S)	${}^{1,2}E_{2g}$	A	\mathbb{Z} (S)
			${}^{1,2}E_{2u}$	A	\mathbb{Z} (P)	${}^{1,2}E_{2u}$	A	\mathbb{Z} (P)
(e) $\bar{\mathcal{G}}^k = C_{2v}, \alpha = 1/2$			(f1) $\bar{\mathcal{G}}^k = C_{3v}, \alpha = 1/2$			(f2) $\bar{\mathcal{G}}^k = C_{3v}, \alpha = 3/2$		
IR of D_{2h}	EAZ	Classification	IR of D_{3d}	EAZ	Classification	IR of D_{3d}	EAZ	Classification
A_g	CI	0 (G)	A_{1g}	CI	0 (G)	A_{1g}	AIII	0 (G)
A_u	CI	0 (G)	A_{1u}	CI	0 (G)	A_{1u}	C	0 (G)
B_{1g}	BDI	\mathbb{Z}_2 (L)	A_{2g}	BDI	\mathbb{Z}_2 (L)	A_{2g}	D	\mathbb{Z}_2 (L)
B_{1u}	BDI	\mathbb{Z}_2 (P)	A_{2u}	BDI	\mathbb{Z}_2 (P)	A_{2u}	AIII	0 (G)
B_{2g}	BDI	\mathbb{Z}_2 (L)	2D IRs see (b1)			2D IRs see (b2)		
B_{2u}	CI	0 (G)						
B_{3g}	BDI	\mathbb{Z}_2 (L)						
B_{3u}	CI	0 (G)						
(g) $\bar{\mathcal{G}}^k = C_{4v}, \alpha = 1/2, 3/2$			(h1) $\bar{\mathcal{G}}^k = C_{6v}, \alpha = 1/2, 5/2$			(h2) $\bar{\mathcal{G}}^k = C_{6v}, \alpha = 3/2$		
IR of D_{4h}	EAZ	Classification	IR of D_{6h}	EAZ	Classification	IR of D_{6h}	EAZ	Classification
A_{1g}	CI	0 (G)	A_{1g}	CI	0 (G)	A_{1g}	CI	0 (G)
A_{1u}	CI	0 (G)	A_{1u}	CI	0 (G)	A_{1u}	CI	0 (G)
A_{2g}	BDI	\mathbb{Z}_2 (L)	A_{2g}	BDI	\mathbb{Z}_2 (L)	A_{2g}	BDI	\mathbb{Z}_2 (L)
A_{2u}	BDI	\mathbb{Z}_2 (P)	A_{2u}	BDI	\mathbb{Z}_2 (P)	A_{2u}	BDI	\mathbb{Z}_2 (P)
B_{1g}	AI	\mathbb{Z} (L)	B_{1g}	AI	\mathbb{Z} (L)	B_{1g}	BDI	\mathbb{Z}_2 (L)
B_{1u}	AI	\mathbb{Z} (P)	B_{1u}	AI	\mathbb{Z} (P)	B_{1u}	CI	0 (G)
B_{2g}	AI	\mathbb{Z} (L)	B_{2g}	AI	\mathbb{Z} (L)	B_{2g}	BDI	\mathbb{Z}_2 (L)
B_{2u}	AI	\mathbb{Z} (P)	B_{2u}	AI	\mathbb{Z} (P)	B_{2u}	CI	0 (G)
2D IRs	see (c)		2D IRs	see (d1)		2D IRs	see (d2)	

Table 4.4: Character tables for 2D IRs of the point groups (a) S_6 , (b) C_{4h} , and (c) C_{6h} . All notations are based on Bilbao Crystallographic Server [111]. It is noteworthy that all representations labeled by the indices 1 and 2 are 1D IRs, which are doubly degenerated under TRS (*e.g.*, $E_u = {}^1E_u + {}^2E_u$). In each table, characters are shown only for generators of the corresponding group.

(a) S_6				(c) C_{6h}					
	E	C_3	I		E	C_6	I		
1E_g	Γ_3^+	1	$e^{-i2\pi/3}$	+1	${}^1E_{1g}$	Γ_6^+	1	$e^{-i\pi/3}$	+1
2E_g	Γ_2^+	1	$e^{+i2\pi/3}$	+1	${}^2E_{1g}$	Γ_5^+	1	$e^{+i\pi/3}$	+1
1E_u	Γ_2^-	1	$e^{-i2\pi/3}$	-1	${}^1E_{1u}$	Γ_6^-	1	$e^{-i\pi/3}$	-1
2E_u	Γ_3^-	1	$e^{+i2\pi/3}$	-1	${}^2E_{1u}$	Γ_5^-	1	$e^{+i\pi/3}$	-1
					${}^1E_{2g}$	Γ_3^+	1	$-e^{-i\pi/3}$	+1
(b) C_{4h}					${}^2E_{2g}$	Γ_2^+	1	$-e^{+i\pi/3}$	+1
1E_g	Γ_4^+	1	$-i$	+1	${}^1E_{2u}$	Γ_3^-	1	$-e^{-i\pi/3}$	-1
2E_g	Γ_3^+	1	$+i$	+1	${}^2E_{2u}$	Γ_2^-	1	$-e^{+i\pi/3}$	-1
1E_u	Γ_4^-	1	$-i$	-1					
2E_u	Γ_3^-	1	$+i$	-1					

Note that since $\hat{\Delta}_+(\mathbf{k})$ and $\hat{\Delta}_-(\mathbf{k})$ are a pair of the order parameter connected by TRS, choosing one of them leads to TRS and CS breaking. Thus we only have to calculate the Wigner criterion for the PHS-like operator $\mathfrak{C} = \mathcal{CI}$:

$$W_{+1/2}^{\mathfrak{C}} = \frac{1}{3} \sum_{\bar{g} \in \{E, C_3, (C_3)^2\}} \omega^k(\mathfrak{C}\bar{g}, \mathfrak{C}\bar{g}) \chi[\bar{\gamma}_{+1/2}^k(\overline{(\mathfrak{C}g)^2})]$$

$$= \begin{cases} 0 & {}^1E_g, \\ 1 & {}^2E_g, \end{cases} \quad (4.2.3)$$

$$W_{+3/2}^{\mathfrak{C}} = \frac{1}{3} \sum_{\bar{g} \in \{E, C_3, (C_3)^2\}} \omega^k(\mathfrak{C}\bar{g}, \mathfrak{C}\bar{g}) \chi[\bar{\gamma}_{+3/2}^k(\overline{(\mathfrak{C}g)^2})]$$

$$= 0 \quad ({}^{1,2}E_g), \quad (4.2.4)$$

where we use Eq. (4.2.2), $\omega_{\text{in}}(\mathfrak{C}, \mathfrak{C}) = +1$, $\omega_{\text{in}}(C_3, C_3)\omega_{\text{in}}((C_3)^2, C_3) = -1$, and the IRs of C_3 in the following.

IR	E	C_3	$(C_3)^2$
$\bar{\gamma}_{+1/2}^k$	1	$e^{+i\pi/3}$	$e^{+i2\pi/3}$
$\bar{\gamma}_{+3/2}^k$	1	-1	1

Here the 1D IRs ${}^{1,2}E_g$ of S_6 are defined in Table 4.4(a). Equations (4.2.3) and (4.2.4) show that the classification results of 1E_g and 2E_g are different (equivalent) for the IR of the normal Bloch

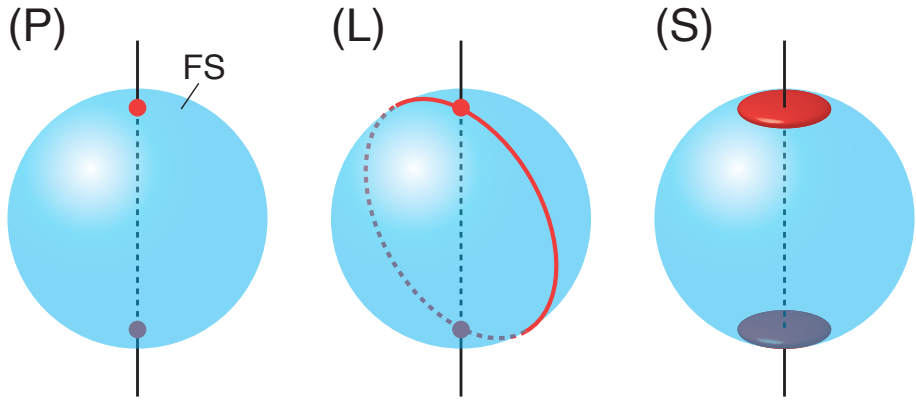


Figure 4.1: Three cases of the gap closing on a high-symmetry axis: (P) point nodes, (L) a part of line nodes, and (S) a part of surface nodes (Bogoliubov FSs).

state $\alpha = +1/2 (+3/2)$; see also Tables 4.3(b1) and 4.3(b2). We remark that the calculations of Eq. (4.2.3) are reversed for an $\alpha = -1/2$ band:

$$W_{-1/2}^{\mathfrak{C}} = \begin{cases} 1 & {}^1E_g, \\ 0 & {}^2E_g. \end{cases} \quad (4.2.6)$$

These results are represented in the square brackets in Table 4.3(b1). In case of the other 2D IRs, we similarly decompose them into the 1D IRs with different eigenvalues of the rotation symmetry (see Table 4.4). For such 1D IRs produced from 2D IRs, therefore, the groups D_{3d} , D_{4h} , and D_{6h} are reduced to S_6 , C_{4h} , and C_{6h} , respectively. Thus we do not show the 2D IRs for D_{3d} , D_{4h} , and D_{6h} groups in Table 4.3.

In Table 4.3, the classification “0” indicates the fully gapped structure on the intriguing high-symmetry line, which is consistent with the results of Table 4.2. If the classification is nontrivial (\mathbb{Z} or \mathbb{Z}_2), on the other hand, the gap closes on the line. As shown in Fig. 4.1, such gap structures have three types when the whole FS is considered: (P) point nodes, (L) a part of line nodes, and (S) a part of surface nodes (Bogoliubov FSs). The condition for each node structure is specified by the parity and TRS of the order parameter as follows.

Case (S): even-parity and TRS breaking order parameter. When both particle bands and hole bands are doubly degenerate, nodes on the high-symmetry axis are point nodes. Indeed, most of the single-band models reproduce the situation. In real superconductors where multi-band effects cannot be neglected, however, the degeneracy splits due to the inter-band pairing effect [31, 112]. As a result, the point nodes are inflated to surface nodes, which are characterized by the 0D topological number (Pfaffian of the antisymmetrized total BdG Hamiltonian) $P(\mathbf{k}) \in \mathbb{Z}_2$ [31].

Case (L): even-parity and TRS preserving order parameter. When the high-symmetry axis possesses the mirror symmetry parallel to the axis (*i.e.*, $\bar{\mathcal{G}}^k \cong C_{nv}$), we can classify the presence or absence of line nodes on the mirror-invariant plane [17, 19, 20] (see Chapter 3). Taking into

account the compatibility relation between the high-symmetry axis and the mirror-invariant plane, it is found that nodes on the C_{nv} -symmetric axis are a part of line nodes on the plane. The line nodes are also protected by the 1D topological number (winding number) $W_l \in \mathbb{Z}$ in Eq. (3.2.10), which is defined by the CS [19, 55, 65]. Even when the mirror symmetry is broken, therefore, the line nodes do not vanish as long as the CS is preserved. Since the line nodes remain intersectant with the axis because of the rotational symmetry, nodes on the C_n -symmetric axis are also a part of the line nodes.

Case (P): odd-parity order parameter. Except for the BZ boundary in nonsymmorphic space groups,³ there is no line node in odd-parity superconductivity [41, 55].

- (P1) When the order parameter breaks TRS, band degeneracy generally splits. However, nodes on the high-symmetry axis are not a part of surface nodes since no 0D topological number is defined at a general point in the 3D BZ. Thus the stable nodes are point nodes.
- (P2) When the order parameter preserves TRS, nodes on the high-symmetry axis are point nodes because the band splitting does not occur.

In the following sections, we see some representative candidates of symmetry-protected nodes on high-symmetry lines.

4.3 Point nodes: UPt₃ (Space group: $P6_3/mmc$)

4.3.1 Background

Superconductivity in UPt₃ has been intensively investigated after the discovery of superconductivity in 1980's [113]. Multiple superconducting phases illustrated in Fig. 4.2 [114–117] unambiguously exhibit exotic Cooper pairing which is probably categorized into the 2D IR of point group D_{6h} [4]. After several theoretical proposals examined by experiments for more than three decades, the E_{2u} representation has been regarded as the most reasonable symmetry of superconducting order parameter [118, 119]. In particular, the multiple superconducting phases in the temperature–magnetic-field plane are naturally reproduced by assuming a weak symmetry-breaking term of hexagonal symmetry [118]. Furthermore, a phase-sensitive measurement [120] and the observation of spontaneous TRS breaking [121, 122] in the low-temperature and low-magnetic-field B phase, which was predicted in the E_{2u} state, support the E_{2u} symmetry of superconductivity.

The crystal structure of UPt₃ is illustrated in Fig. 4.3. The symmetry of the crystal is represented by nonsymmorphic space group $P6_3/mmc$,⁴ which is based on the primitive hexagonal Bravais lattice. In this space group, the BZ takes the form of Fig. 4.4. This BZ has a threefold rotation axis on the K - H line as well as a sixfold rotation axis on the Γ - A line.

³This case is beyond the scope of the Chapter.

⁴Symmetry breaking by a weak crystal distortion has been reported [124], although its reliability is under debate. We here assume high symmetry space group $P6_3/mmc$.

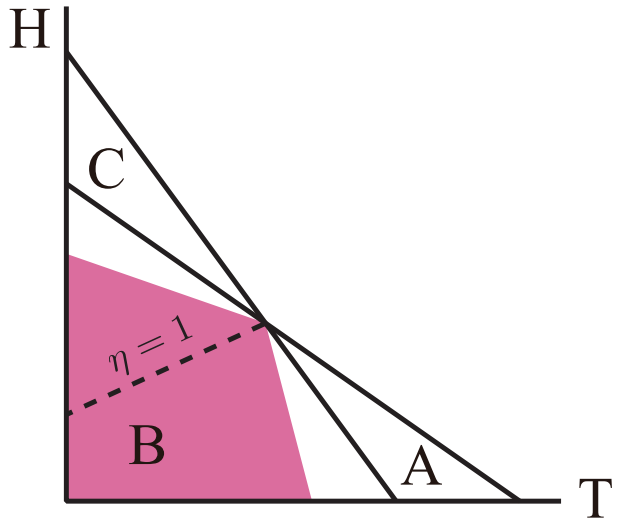


Figure 4.2: Multiple superconducting phases of UPt₃ in the magnetic field-temperature plane [118, 119]. The shaded region shows the Weyl superconducting phase [13, 123]. In the system, C_3 symmetry is preserved only on the dashed line.

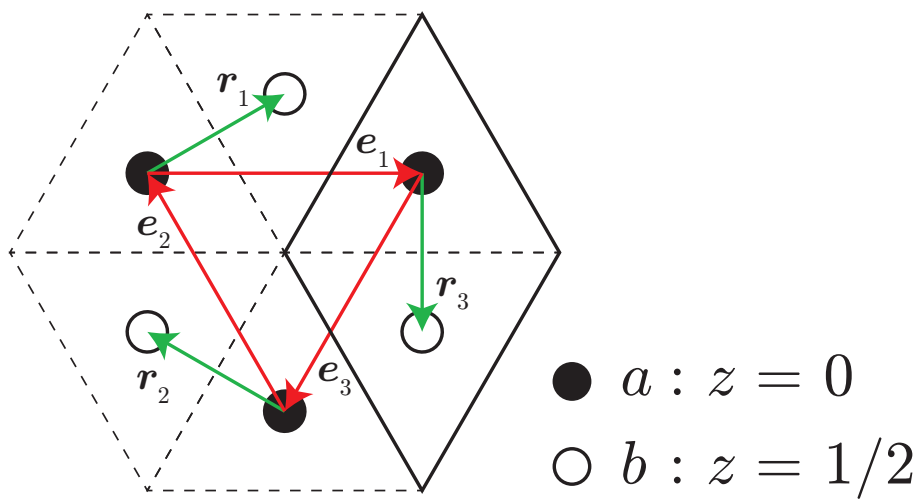


Figure 4.3: Crystal structure of UPt₃. Uranium ions form AB stacked triangular lattice. 2D vectors, e_i and r_i , are shown by arrows. The black solid diamond shows the unit cell.

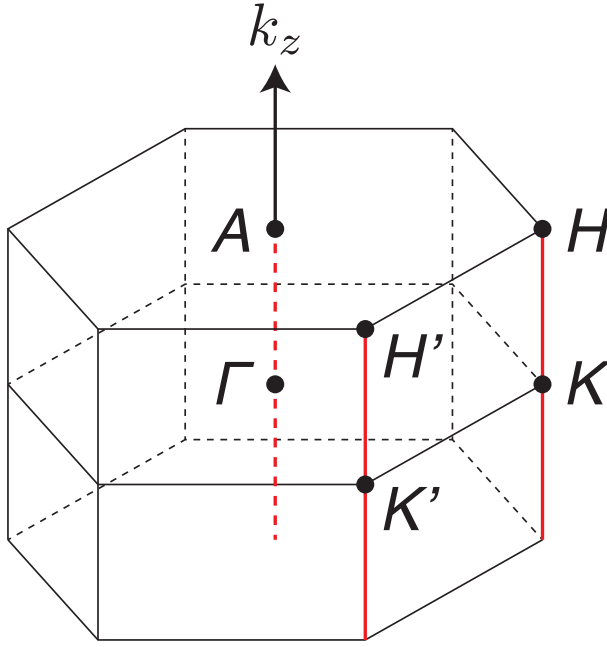


Figure 4.4: The first BZ of primitive hexagonal lattice. The red lines show threefold and sixfold rotation symmetric axes.

Quantum oscillation measurements combined with band-structure calculations [14, 119, 125–128] have shown a pair of FSs centered at the A point (A -FSs), three FSs at the Γ point (Γ -FSs), and two FSs at the K point (K -FSs) in UPt_3 . Although previous studies have clarified gap structures on the A -FSs and Γ -FSs [5–7, 11–14, 123], those on the K -FSs have not been theoretically studied. From the results of classification theory given in this section, however, it would be interesting to examine the gap structure on the K -FSs, since they cross the K - H line. Indeed, we show the intriguing j_z -dependent point nodes on the K - H line.

4.3.2 Gap classification on K - H line

Now we apply the gap classification in Tables 4.2 and 4.3 to the space group of UPt_3 . In the space group $P6_3/mmc$, the BZ has a sixfold axis Γ - A , and threefold axes K - H and K' - H' (see Fig. 4.4). On the Γ - A line, the little cogroup has C_{6v} symmetry which results in three types of the normal Bloch state $E_{1/2}$, $E_{3/2}$, and $E_{5/2}$. In the superconducting state, we obtain two different representations of the Cooper pair wave function (see Table 4.2):

$$\bar{P}^k = \begin{cases} A_{1g} + A_{1u} + E_{1u} & (\bar{\lambda}_\alpha^k = E_{1/2}, E_{5/2}), \\ A_{1g} + A_{1u} + B_{1u} + B_{2u} & (\bar{\lambda}_\alpha^k = E_{3/2}), \end{cases} \quad (4.3.1)$$

which have been decomposed into IRs of point group $D_{6h} = C_{6v} + IC_{6v}$. The same result has been suggested by Yarzhemsky [5, 7]. From the discussion in this section, UPt_3 is considered to possess

the E_{2u} superconducting order parameter. According to Eq. (4.3.1), the E_{2u} representation is not allowed for any representations $E_{1/2}$, $E_{3/2}$, and $E_{5/2}$. Therefore, point nodes appear on the Γ - A line irrespective of the property of the normal Bloch state. We can obtain the same conclusion with the Sigrist-Ueda method.

On the other hand, the gap structure on the K - H (K' - H') line is j_z -dependent. The little cogroup has C_{3v} symmetry, which results in two representations $\bar{\lambda}_\alpha^k = E_{1/2}$ and $E_{3/2}$. Corresponding to these two Bloch states, the Cooper pair wave function has two different representations:

$$\bar{P}^k = \begin{cases} A_{1g} + A_{1u} + E_u & (\bar{\lambda}_\alpha^k = E_{1/2}), \\ A_{1g} + 2A_{1u} + A_{2u} & (\bar{\lambda}_\alpha^k = E_{3/2}), \end{cases} \quad (4.3.2)$$

which have been decomposed into IRs of point group $D_{3d} = C_{3v} + IC_{3v}$. Then, \bar{P}^k can be induced to the point group D_{6h} with the help of the Frobenius reciprocity theorem [45]. The induced representations $\bar{P}^k \uparrow D_{6h}$ are summarized in the following equations:

$$\bar{P}^k \uparrow D_{6h} = \begin{cases} A_{1g} + B_{2g} + A_{1u} + B_{2u} + E_{1u} + E_{2u} & (\bar{\lambda}_\alpha^k = E_{1/2}), \\ A_{1g} + B_{2g} + 2A_{1u} + A_{2u} + B_{1u} + 2B_{2u} & (\bar{\lambda}_\alpha^k = E_{3/2}). \end{cases} \quad (4.3.3)$$

From Eq. (4.3.3), the E_{2u} superconducting gap opens for the $E_{1/2}$ normal Bloch state, while point nodes appear for $E_{3/2}$. Thus, the gap structure indeed depends on the angular momentum of Bloch states. In this case, the classification by the Sigrist-Ueda method breaks down since it has taken into account only the pseudospin degree of freedom $s = 1/2$.

From the viewpoint of topology, furthermore, Tables 4.3(b1) and 4.3(b2) shows that the topological classifications for an ${}^{1,2}E_u$ order parameter indeed depend on the angular momentum:

$$0 \oplus \mathbb{Z} \text{ for } \alpha = \pm 1/2, \quad (4.3.4a)$$

$$\mathbb{Z} \oplus \mathbb{Z} \text{ for } \alpha = \pm 3/2. \quad (4.3.4b)$$

However, in this case, the topological classification is slightly different from the gap classification by symmetry. For one of the $\alpha = \pm 1/2$ states, the gap opens while the gap closes for the other state. Which one is gapped depends on the C_3 eigenvalue of the order parameter. The inconsistency is due to the fact that the spontaneous TRS breaking is taken into account in the topological argument although it is not in the symmetry analysis. In this case the topological classification predicts a correct gap structure.

In the following, we demonstrate the nontrivial j_z -dependent gap structure by analyzing a microscopic model.

4.3.3 Model and normal Bloch state

Here we introduce the microscopic model of UPt₃, and we clarify the band structure on the *K*-*H* line. First, we introduce the BdG Hamiltonian for a two-sublattice model [13, 123],

$$H_{\text{BdG}} = \frac{1}{2} \sum_{\mathbf{k}} \mathbf{C}^\dagger(\mathbf{k}) \begin{pmatrix} \hat{H}_n(\mathbf{k}) & \hat{\Delta}(\mathbf{k}) \\ \hat{\Delta}(\mathbf{k})^\dagger & -\hat{H}_n(-\mathbf{k})^T \end{pmatrix} \mathbf{C}(\mathbf{k}), \quad (4.3.5)$$

with

$$\mathbf{C}^\dagger(\mathbf{k}) = (c_{a\uparrow}^\dagger(\mathbf{k}), c_{a\downarrow}^\dagger(\mathbf{k}), c_{b\uparrow}^\dagger(\mathbf{k}), c_{b\downarrow}^\dagger(\mathbf{k}), c_{a\uparrow}(-\mathbf{k}), c_{a\downarrow}(-\mathbf{k}), c_{b\uparrow}(-\mathbf{k}), c_{b\downarrow}(-\mathbf{k})), \quad (4.3.6)$$

where \mathbf{k} , $m = a, b$, and $s = \uparrow, \downarrow$ are the index of momentum, sublattice, and spin, respectively. The BdG Hamiltonian matrix is described by the normal-state Hamiltonian,

$$\hat{H}_n(\mathbf{k}) = \begin{pmatrix} \xi(\mathbf{k})s_0 + \alpha \mathbf{g}(\mathbf{k}) \cdot \mathbf{s} & a(\mathbf{k})s_0 \\ a(\mathbf{k})^*s_0 & \xi(\mathbf{k})s_0 - \alpha \mathbf{g}(\mathbf{k}) \cdot \mathbf{s} \end{pmatrix}, \quad (4.3.7)$$

and the order-parameter part $\hat{\Delta}(\mathbf{k}) = [\Delta(\mathbf{k})]_{ms, m's'}$. Here s_i represents the Pauli matrix in spin space. Taking into account the crystal structure of UPt₃ illustrated in Fig. 4.3, we adopt an intra-sublattice kinetic energy,

$$\xi(\mathbf{k}) = 2t \sum_{i=1,2,3} \cos \mathbf{k}_\parallel \cdot \mathbf{e}_i + 2t_z \cos k_z - \mu, \quad (4.3.8)$$

and an inter-sublattice hopping term,

$$a(\mathbf{k}) = 2t' \cos \frac{k_z}{2} \sum_{i=1,2,3} e^{i\mathbf{k}_\parallel \cdot \mathbf{r}_i}, \quad (4.3.9)$$

with $\mathbf{k}_\parallel = (k_x, k_y)$. The basis translation vectors in two dimensions are $\mathbf{e}_1 = (1, 0)$, $\mathbf{e}_2 = (-\frac{1}{2}, \frac{\sqrt{3}}{2})$, and $\mathbf{e}_3 = (-\frac{1}{2}, -\frac{\sqrt{3}}{2})$. The inter-layer neighboring vectors projected onto the *x*-*y* plane are given by $\mathbf{r}_1 = (\frac{1}{2}, \frac{1}{2\sqrt{3}})$, $\mathbf{r}_2 = (-\frac{1}{2}, \frac{1}{2\sqrt{3}})$, and $\mathbf{r}_3 = (0, -\frac{1}{\sqrt{3}})$. These 2D vectors are illustrated in Fig. 4.3.

Although the crystal point group symmetry is centrosymmetric, D_{6h} , the local point group symmetry at uranium ions is D_{3h} lacking inversion symmetry. Then, Kane-Mele ASOC [129] with a \mathbf{g} vector [130],

$$\mathbf{g}(\mathbf{k}) = \hat{z} \sum_{i=1,2,3} \sin \mathbf{k}_\parallel \cdot \mathbf{e}_i, \quad (4.3.10)$$

is allowed by symmetry. The coupling constant is staggered between the two sublattices, so as to preserve the global D_{6h} point group symmetry [129, 131, 132].

In order to identify the Bloch state, we calculate the normal energy bands on the *K*-*H* line from the normal part Hamiltonian [Eq. (4.3.7)]. Although the band originally has fourfold degeneracy arising from the two sublattices and two spin degrees of freedom, this splits into twofold + twofold degenerate bands due to the effect of the ASOC term. The band structures are schematically shown

in Figs. 4.5(a) and 4.5(b). When the coupling constant of the ASOC term α is positive,⁵ $|a, \uparrow\rangle$ and $|b, \downarrow\rangle$ states cross the Fermi level on the K - H line, while $|b, \uparrow\rangle$ and $|a, \downarrow\rangle$ states cross on the K' - H' line [Fig. 4.5(a)]. On the other hand, the spin state on the Fermi level changes as shown in Fig. 4.5(b), when the α is negative. Note that the pure sublattice-based representations construct the basis of energy bands, since the inter-sublattice hopping term Eq. (4.3.9) vanishes on the K - H and K' - H' lines. This vanishing has been proved by the symmetry analysis [133, 134].

We have investigated the energy band structures of the normal state in the above discussion. In order to identify superconducting gap structures, therefore, we should solve the following question: Which representation does the band crossing the Fermi level belong to, $E_{1/2}$ or $E_{3/2}$? The difference between these two representations is the total angular momentum j_z ($= \pm 1/2$ or $\pm 3/2$) of the Bloch state. In the next subsection, we show that j_z contains an *effective orbital angular momentum* arising from the permutation of sites, as well as the pure orbital angular momentum and the spin angular momentum.

4.3.4 Effective orbital angular momentum

Here we investigate the total angular momentum j_z of the Bloch state, and we show that j_z includes an effective orbital angular momentum λ_z arising from a Bloch phase of each site, in addition to the pure orbital and spin angular momentum. Furthermore, we clarify that j_z of the Bloch states crossing the Fermi level depends on the sign of the ASOC α .

First, recalling the quantum mechanics, j_z should contain the orbital angular momentum l_z and the spin angular momentum s_z . In our two-sublattice single-orbital model [Eq. (4.3.7)], the orbital degree of freedom is neglected, and then, $l_z = 0$. Since electrons are spin-1/2 fermions, the spin angular momentum is $s_z = \pm 1/2$. Therefore, we might consider that $j_z = l_z + s_z = \pm 1/2$ in this model. However, this is not right, as we show below.

In order to correctly calculate j_z , we have to take into account the effective orbital angular momentum λ_z due to the permutation of sites. The Bloch state has a phase factor (plane-wave part) $e^{i\mathbf{k}\cdot\mathbf{r}}$ depending on the site [133, 134], which is illustrated in Fig. 4.6 for the K -point Bloch state [$\mathbf{k} = (4\pi/3, 0, 0)$]. By operating threefold rotation on the K -point Bloch state, the a sublattice obtains the phase value $e^{+i2\pi/3}$ (red arrows), while the b sublattice gets $e^{-i2\pi/3}$ (blue arrows). These phase factors, which correspond to $e^{i\lambda_z\theta}$ ($\theta = 2\pi/3$), indicate that the sublattices a and b possess an effective orbital angular momentum $\lambda_z = +1$ and -1 , respectively. The Bloch state at the K' point has a complex conjugate phase factor to that on the K -point, which results in $\lambda_z = -1$ (+1) for the a (b) sublattice. For a more general argument, the effective orbital angular momentum can be calculated by analyzing the space-group transformation of the Bloch state (see Appendix B.2).

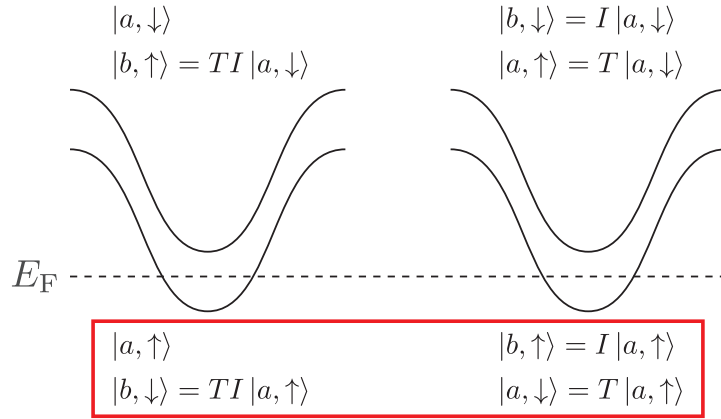
Using the above discussion, we calculate the total angular momentum of the Bloch state by $j_z = l_z + s_z + \lambda_z$. For example, in the $|a, \uparrow\rangle$ state on the K - H line [see Fig. 4.5(a)], $l_z = 0$, $s_z = +1/2$,

⁵Here, we dub the ASOC coupling constant as α according to the convention. Although the symbol is the same as that of the normal Bloch state, the difference is obvious from the context.

(a) $\alpha > 0$

K - H line

K' - H' line



(b) $\alpha < 0$

K - H line

K' - H' line

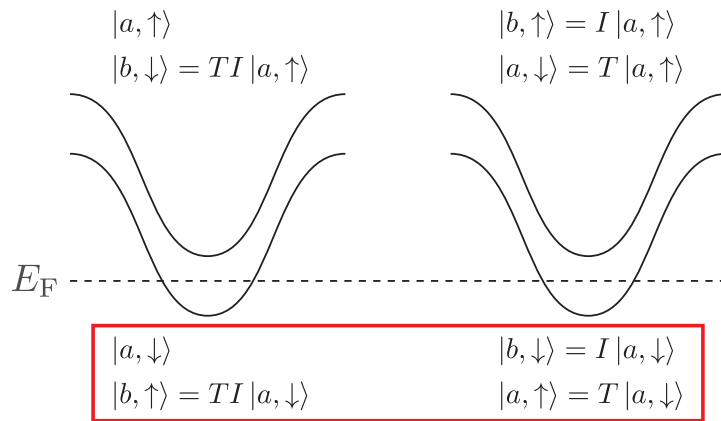


Figure 4.5: Schematic band structures on the K - H and K' - H' lines for (a) the ASOC $\alpha > 0$ and (b) $\alpha < 0$. The wave function of Bloch states crossing the Fermi level is shown in the red frame. The wave function of the upper band is shown above the band.

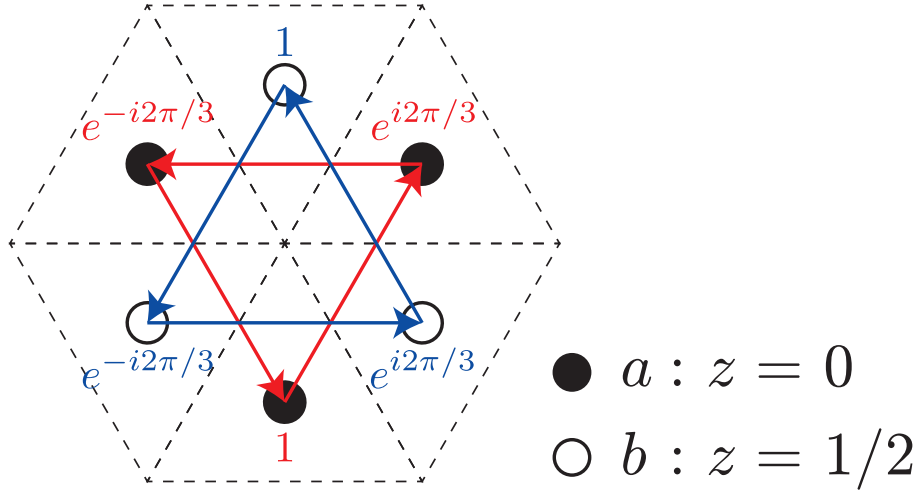


Figure 4.6: The phase factor $e^{ik \cdot r}$ on sites for the K -point Bloch state. The sublattices a and b obtain different phase values by threefold rotation.

$\lambda_z = +1$, so that we obtain $j_z = +3/2$. The total angular momenta of all states are summarized in Table 4.5. From Figs. 4.5(a) and 4.5(b), and Table 4.5, we identify the representations of the Bloch states crossing the Fermi level as follows.

(a) $\alpha > 0$: $E_{3/2}$ representation, because

$$|a, \uparrow\rangle = |j_z = +\frac{3}{2}\rangle, \quad |b, \downarrow\rangle = |j_z = -\frac{3}{2}\rangle,$$

on the K - H line, and

$$|b, \uparrow\rangle = |j_z = +\frac{3}{2}\rangle, \quad |a, \downarrow\rangle = |j_z = -\frac{3}{2}\rangle,$$

on the K' - H' line.

(b) $\alpha < 0$: $E_{1/2}$ representation, because

$$|a, \downarrow\rangle = |j_z = +\frac{1}{2}\rangle, \quad |b, \uparrow\rangle = |j_z = -\frac{1}{2}\rangle,$$

on the K - H line, and

$$|b, \downarrow\rangle = |j_z = +\frac{1}{2}\rangle, \quad |a, \uparrow\rangle = |j_z = -\frac{1}{2}\rangle,$$

on the K' - H' line.

Assuming the E_{2u} superconducting order parameter, therefore, the gap classification theory indicates that point nodes emerge on the K - H (K' - H') line when $\alpha > 0$, while the gap opens otherwise [see Eq. (4.3.3)]. In the next subsection, we demonstrate such unusual gap structures by a numerical analysis of the microscopic model.

Table 4.5: The total angular momentum of the Bloch state.

K-H line				K'-H' line				
l_z	s_z	λ_z	j_z	l_z	s_z	λ_z	j_z	
$ a, \uparrow\rangle$	0	+1/2	+1	+3/2	0	+1/2	-1	-1/2
$ a, \downarrow\rangle$	0	-1/2	+1	+1/2	0	-1/2	-1	-3/2
$ b, \uparrow\rangle$	0	+1/2	-1	-1/2	0	+1/2	+1	+3/2
$ b, \downarrow\rangle$	0	-1/2	-1	-3/2	0	-1/2	+1	+1/2

4.3.5 Gap structures depending on Bloch-state angular momentum

Now we demonstrate unconventional j_z -dependent gap structures using the numerical calculation of the microscopic model. To investigate the superconducting gap structures, we consider the two-component order parameters in the E_{2u} IR of point group D_{6h} :

$$\hat{\Delta}(\mathbf{k}) = \eta_1 \hat{\Gamma}_1^{E_{2u}} + \eta_2 \hat{\Gamma}_2^{E_{2u}}. \quad (4.3.11)$$

The two-component order parameters are parameterized as

$$(\eta_1, \eta_2) = \Delta(1, i\eta) / \sqrt{1 + \eta^2}, \quad (4.3.12)$$

with a real variable η . The basis functions $\hat{\Gamma}_1^{E_{2u}}$ and $\hat{\Gamma}_2^{E_{2u}}$ are admixtures of some harmonics. Adopting the neighboring Cooper pairs in the crystal lattice of uranium ions, we obtain the basis functions

$$\begin{aligned} \hat{\Gamma}_1^{E_{2u}} = & \left[\delta_1 \{ p_x^{(\text{intra})}(\mathbf{k}) s_x - p_y^{(\text{intra})}(\mathbf{k}) s_y \} \sigma_0 \right. \\ & + \delta_2 \{ p_x^{(\text{inter})}(\mathbf{k}) s_x - p_y^{(\text{inter})}(\mathbf{k}) s_y \} \frac{\sigma_+}{2} + \delta_2 \{ p_x^{(\text{inter})}(\mathbf{k})^* s_x - p_y^{(\text{inter})}(\mathbf{k})^* s_y \} \frac{\sigma_-}{2} \\ & \left. + f_{(x^2-y^2)z}(\mathbf{k}) s_z \sigma_x - d_{yz}(\mathbf{k}) s_z \sigma_y \right] i s_y, \end{aligned} \quad (4.3.13)$$

$$\begin{aligned} \hat{\Gamma}_2^{E_{2u}} = & \left[\delta_1 \{ p_y^{(\text{intra})}(\mathbf{k}) s_x + p_x^{(\text{intra})}(\mathbf{k}) s_y \} \sigma_0 \right. \\ & + \delta_2 \{ p_y^{(\text{inter})}(\mathbf{k}) s_x + p_x^{(\text{inter})}(\mathbf{k}) s_y \} \frac{\sigma_+}{2} + \delta_2 \{ p_y^{(\text{inter})}(\mathbf{k})^* s_x + p_x^{(\text{inter})}(\mathbf{k})^* s_y \} \frac{\sigma_-}{2} \\ & \left. + f_{xyz}(\mathbf{k}) s_z \sigma_x - d_{xz}(\mathbf{k}) s_z \sigma_y \right] i s_y, \end{aligned} \quad (4.3.14)$$

which are composed of the intra-sublattice p -wave, inter-sublattice p -wave, and inter-sublattice $d + f$ -wave components given by

$$p_x^{(\text{intra})}(\mathbf{k}) = \sum_i e_i^x \sin \mathbf{k}_{\parallel} \cdot \mathbf{e}_i, \quad (4.3.15)$$

$$p_y^{(\text{intra})}(\mathbf{k}) = \sum_i e_i^y \sin \mathbf{k}_{\parallel} \cdot \mathbf{e}_i, \quad (4.3.16)$$

$$p_x^{(\text{inter})}(\mathbf{k}) = -i\sqrt{3} \cos \frac{k_z}{2} \sum_i r_i^x e^{i\mathbf{k}_{\parallel} \cdot \mathbf{r}_i}, \quad (4.3.17)$$

$$p_y^{(\text{inter})}(\mathbf{k}) = -i\sqrt{3} \cos \frac{k_z}{2} \sum_i r_i^y e^{i\mathbf{k}_{\parallel} \cdot \mathbf{r}_i}, \quad (4.3.18)$$

$$d_{xz}(\mathbf{k}) = -\sqrt{3} \sin \frac{k_z}{2} \text{Im} \sum_i r_i^x e^{i\mathbf{k}_{\parallel} \cdot \mathbf{r}_i}, \quad (4.3.19)$$

$$d_{yz}(\mathbf{k}) = -\sqrt{3} \sin \frac{k_z}{2} \text{Im} \sum_i r_i^y e^{i\mathbf{k}_{\parallel} \cdot \mathbf{r}_i}, \quad (4.3.20)$$

$$f_{xyz}(\mathbf{k}) = -\sqrt{3} \sin \frac{k_z}{2} \text{Re} \sum_i r_i^x e^{i\mathbf{k}_{\parallel} \cdot \mathbf{r}_i}, \quad (4.3.21)$$

$$f_{(x^2-y^2)z}(\mathbf{k}) = -\sqrt{3} \sin \frac{k_z}{2} \text{Re} \sum_i r_i^y e^{i\mathbf{k}_{\parallel} \cdot \mathbf{r}_i}. \quad (4.3.22)$$

Pauli matrices in the spin and sublattice space are denoted by s_i and σ_i , respectively. σ_+ and σ_- are defined by $\sigma_{\pm} = \sigma_x \pm i\sigma_y$.

A similar model was introduced to investigate the topological superconductivity in UPt₃ [13, 123], and it has recently been studied to show the polar Kerr effect [135] and the odd-frequency Cooper pairs [136]. In these previous studies, the inter-sublattice p -wave component was neglected. Here we take into account the inter-sublattice p -wave component and show that it actually plays an essential role for the j_z -dependent point node, because the other components vanish on the K - H line. We assume that the $d + f$ -wave component is dominant among all the order parameters since the purely f -wave state reproduces the multiple superconducting phase diagram illustrated in Fig. 4.2 [114–116, 118, 119]. On the other hand, an admixture of p -wave components allowed by symmetry changes the gap structure. Thus, we take into account small intra- and inter-sublattice p -wave components with $0 < |\delta_1| \ll 1$ and $0 < |\delta_2| \ll 1$, respectively.

Now we briefly review the multiple superconducting phases illustrated in Fig. 4.2 [114–116, 118, 119]. The A, B, and C phases are characterized by the ratio of two-component order parameters $\eta = \eta_2/i\eta_1$ summarized in Table 4.6. A pure imaginary ratio of η_1 and η_2 in the B phase implies the chiral superconducting state, which maximally gains the condensation energy. A recent theoretical study based on our two-sublattice model [135] has shown the polar Kerr effect consistent with the experiment [122]. Owing to the p -wave components, the B phase is a nonunitary state. It has been considered that the A and C phases are stabilized by weak symmetry breaking of hexagonal structure, possibly induced by weak antiferromagnetic order [118, 119, 137, 138]. We assume here that the A phase is the Γ_2 state ($\eta = \infty$), while the C phase is the Γ_1 state ($\eta = 0$), and we assume non-negative $\eta \geq 0$ without loss of generality.

Analyzing the BdG Hamiltonian Eq. (4.3.5) including the two-component order parameters Eqs. (4.3.11)–(4.3.14), we investigate the superconducting gap structures on the K - H line. Figures 4.7(a) and 4.7(b) represent the calculated quasiparticle energy dispersion in the A phase, which show that point nodes emerge in the positive α case, while the gap opens in the negative α case.

Table 4.6: Range of the parameter η in the A, B, and C phases of UPt₃.

A phase	$ \eta = \infty$
B phase	$0 < \eta < \infty$
C phase	$ \eta = 0$

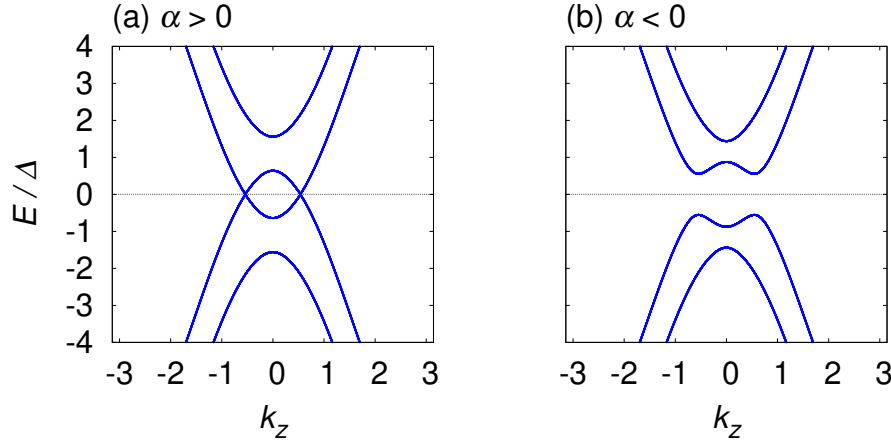


Figure 4.7: The quasiparticle energy dispersion on the K - H line for (a) the ASOC $\alpha = 0.2 > 0$ and (b) $\alpha = -0.2 < 0$. We assume the superconducting phase preserving TRS, namely A phase ($\eta = \infty$) or C phase ($\eta = 0$). The other parameters $(t, t_z, t', \mu, \Delta, \delta_1, \delta_2) = (1, -1, 0.4, -5.2, 0.5, 0.04, 0.2)$ are assumed so that the K -FSs of UPt₃ are reproduced.

Qualitatively the same results are obtained in the C phase. All the results are consistent with the gap classification in Eq. (4.3.3). Thus, it is confirmed that the gap structures depending on the Bloch-state angular momentum j_z are realized on the K -FSs of UPt₃.

Here we discuss the effects of SSB in the superconducting phase. As mentioned at the end of Sec. 4.3.2, *group-theoretical* gap classification does not take into account SSB of the ordered state. Therefore, the results of gap classification [Eq. (4.3.3)] cannot be applied to the SSB phase in a straightforward way. On the other hand, the spontaneous TRS breaking is taken into account in the *topological* gap classification [Eq. (4.3.4)], where C_3 rotation symmetry remains.

We also demonstrate such a TRS breaking case by using the effective model. The TRS breaking and C_3 preserving order parameter (1E_u or 2E_u) is realized for $|\eta| = 1$ (see the dashed line in Fig. 4.2), where a topological phase transition occurs [123]. Therefore we diagonalize the BdG Hamiltonian for $\eta = 1$, which results in the quasiparticle energy dispersion in Fig. 4.8. When the ASOC α is positive, both bands create nodes at the zero energy [Fig. 4.8(a)]. For a negative α , on the other hand, one band holds nodes but the other one is fully gapped [Fig. 4.8(b)], which indicates a *perfectly spin-polarized nonunitary state*. For both IRs, the nodes on the K - H line are topologically

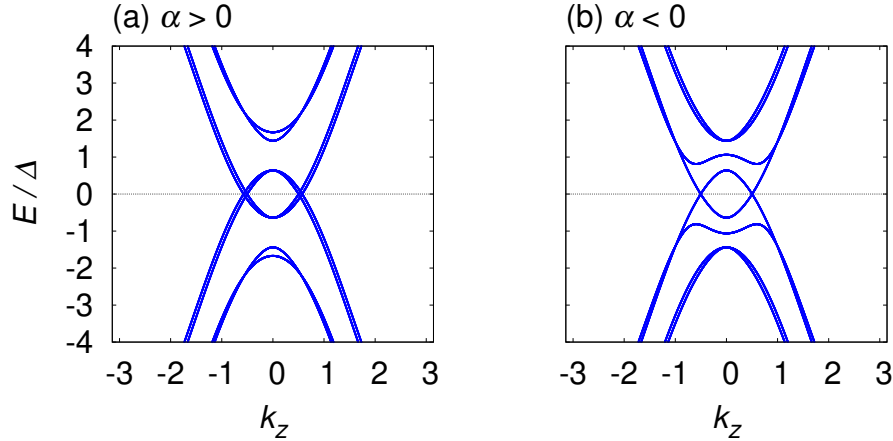


Figure 4.8: The quasiparticle energy dispersion on the K - H line for (a) the ASOC $\alpha = 0.2 > 0$ and (b) $\alpha = -0.2 < 0$. We assume the C_3 preserving and TRS breaking B phase ($\eta = 1$).

characterized by the number of occupied states of the block-diagonalized Hamiltonian, which is obtained by using the threefold rotation matrix $\hat{U}_{\text{BdG}}(C_3)$.

In this subsection, we have revealed the j_z -dependent point nodes or gap opening corresponding to the sign of the ASOC term in the effective model Eq. (4.3.5). The remaining question is which representation is realized in UPt₃. According to our first-principles band-structure calculation, the Bloch state on the K - H line belongs to the $E_{1/2}$ representation [139]. Combining this first-principles calculation and the gap classification theory, we conclude that the superconducting gap opens on the K - H line in UPt₃ except for the topologically-protected point nodes emerging in the B phase.

4.3.5.1 Application to Weyl superconductivity in B phase

We also calculate the nodal structure in the B phase for a general parameter $0 < \eta < \infty$. In the TRS breaking phase, there generally exists Weyl nodes characterized by a topological Weyl charge, which is defined by a monopole of Berry flux,

$$q_i = \frac{1}{2\pi} \oint_S d\mathbf{k} \cdot \mathbf{F}(\mathbf{k}). \quad (4.3.23)$$

Here, the Berry flux

$$F_i(\mathbf{k}) = -i\epsilon^{ijk} \sum_{E_n(\mathbf{k})<0} \partial_{k_j} \langle u_n(\mathbf{k}) | \partial_{k_k} u_n(\mathbf{k}) \rangle, \quad (4.3.24)$$

is integrated on a closed surface S surrounding an isolated point node. We identify Weyl nodes by calculating k_z -dependent Chern number,

$$v(k_z) = \frac{1}{2\pi} \int dk_x dk_y F_z(\mathbf{k}), \quad (4.3.25)$$

on a 2D k_x - k_y plane [140–142]. An n -th wave function and energy of Bogoliubov quasiparticles are denoted by $|u_n(\mathbf{k})\rangle$ and $E_n(\mathbf{k})$, respectively. By definition, when the Chern number jumps at k_z , its value is equal to the sum of Weyl charges at k_z :

$$\nu(k_z + 0) - \nu(k_z - 0) = \sum_i q_i. \quad (4.3.26)$$

Therefore we can identify Weyl charges by counting point nodes and comparing it with a jump in $\nu(k_z)$. Indeed, the previous study has reported the presence of many Weyl nodes on the Γ - and A -FSs [13].

By using the above method, we obtain the superconducting gap structures on the K -FS illustrated in Fig. 4.9. Weyl nodes (blue and red circles in Fig. 4.9) appear in the B phase, in addition to the symmetry-protected point nodes for the $j_z = \pm 3/2$ normal Bloch state [orange circles in Fig. 4.9(a)]. The former Weyl nodes are identified by jumps of the Chern number shown in Fig. 4.10. Figure 4.10(b1) shows that the Chern number jumps by ± 4 , and we find two point nodes on the K -FS at a certain k_z [Fig. 4.9(b), $\eta = 0.95$]. C_6 symmetry ensures that there also exists two point nodes on the K' -FS at the same k_z . Therefore the point nodes are identified as single Weyl nodes with a unit charge $q_i = \pm 1$. Through the above discussion, we determine the charge of Weyl nodes as depicted in Fig. 4.9.

It is shown that the position of Weyl nodes changes as a function of η , which indicates that the nodal structure significantly depends on the temperature and magnetic field in UPt₃. For $j_z = \pm 3/2$ bands, the A and C phases host symmetry-protected point nodes on the north and south pole of the FS [Fig. 4.9(a), $\eta < 0.2$ and $\eta > 5$]. With an influence from the gap zeros, Weyl nodes appear in the comparatively wide range of the B phase: $0.8 \lesssim \eta \lesssim 3$. On the other hand, there is no node in the A and C phases for $j_z = \pm 1/2$ bands [Fig. 4.9(b), $\eta < 0.9$ and $\eta > 1.5$]. Therefore the B phase hosts Weyl nodes only in the narrow region around the $\eta = 1$ line in Fig. 4.2: $0.95 \lesssim \eta \lesssim 1.1$. As a result, reflecting the angular momentum dependence of the gap classification on the C_{3v} -symmetric K - H line, the structures of Weyl nodes are obviously different between $j_z = \pm 3/2$ [Fig. 4.9(a)] and $j_z = \pm 1/2$ [Fig. 4.9(b)]. The nodal structure of Weyl superconductors may be clarified by the thermal Hall conductivity [143].

4.4 Surface nodes: SrPtAs (Space group: $P6_3/mmc$)

4.4.1 Background

SrPtAs is a pnictide superconductor with a hexagonal lattice characterized by the nonsymmorphic space group $P6_3/mmc$ (D_{6h}^4). First-principles studies using local density approximation show 2D FSs enclosing the Γ - A line, a 2D FS enclosing the K - H line, and a 3D FS crossing the K - H line [144–146]. The pairing symmetry of SrPtAs is still under debate because of the incompatibility of some experiments: for example, TRS breaking and a nodeless pairing gap suggested in a muon spin-rotation/relaxation measurement [147] are incompatible with a spin-singlet s -wave superconducting

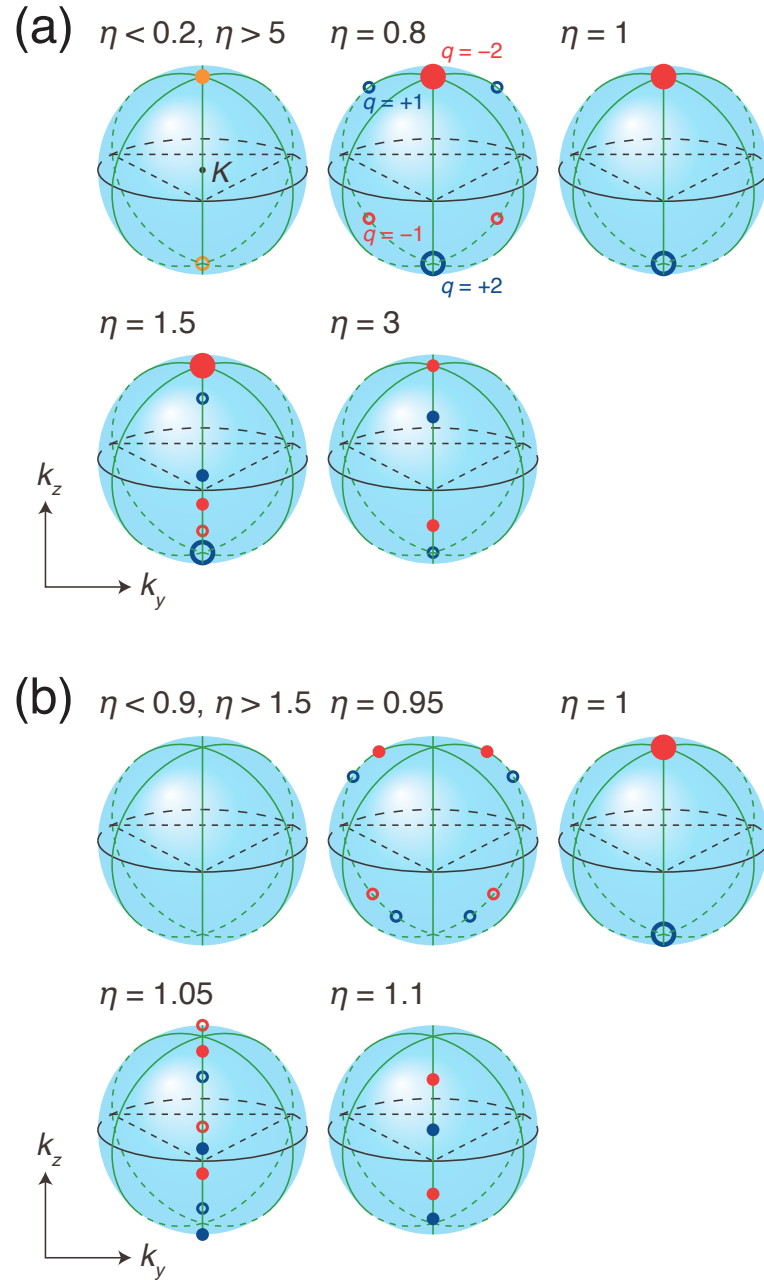


Figure 4.9: Illustration of pair creation and annihilation of Weyl nodes on the K -FS for (a) $j_z = \pm 3/2$ bands and (b) $j_z = \pm 1/2$ bands. Blue and red circles show single Weyl nodes with $q_i = 1$ and -1 , respectively. Large circles are double Weyl nodes with $q_i = \pm 2$. Orange circles are trivial point nodes protected by C_3 symmetry. Closed (open) circles represent nodes on the front (back) side of the FS.

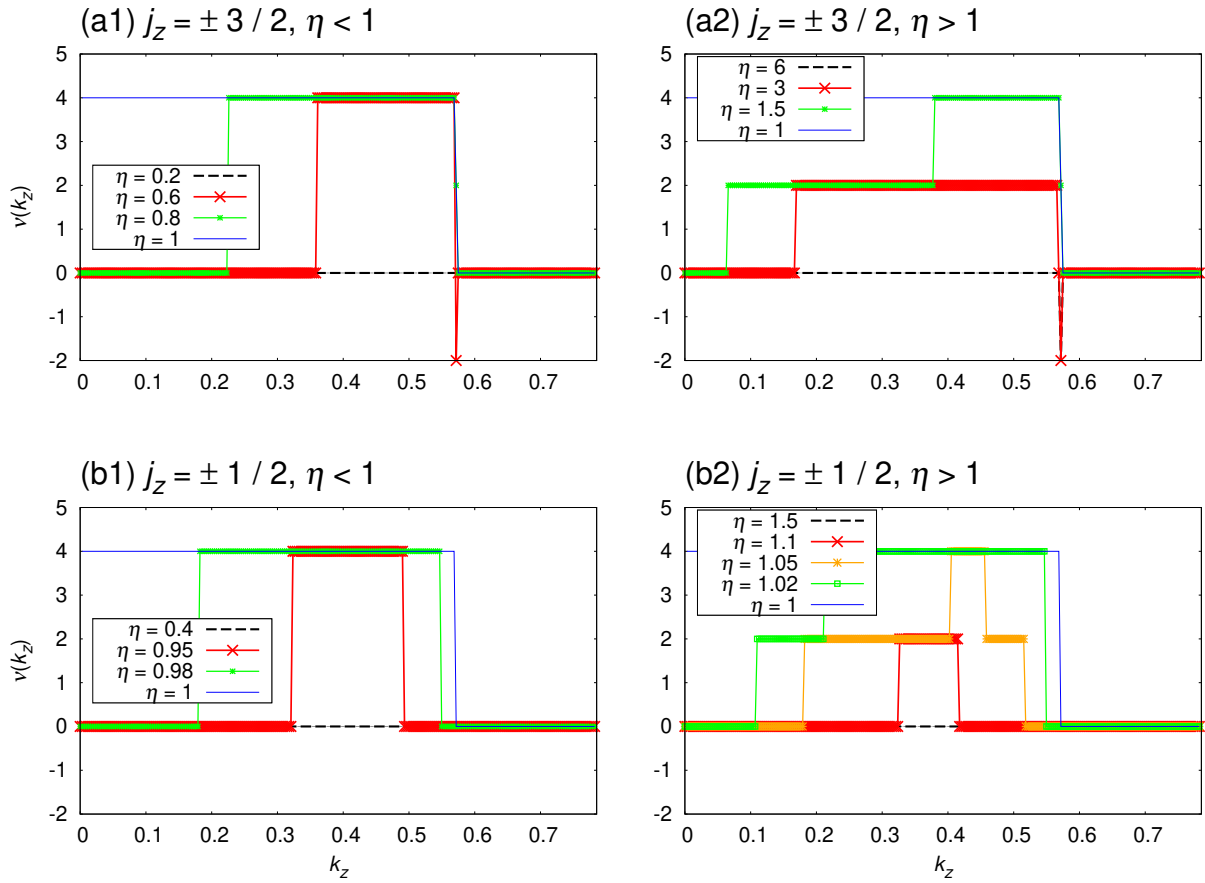


Figure 4.10: Chern number of the 2D BdG Hamiltonian parameterized by k_z for (a) $j_z = \pm 3/2$ bands and (b) $j_z = \pm 1/2$ bands on the K -FS reproduced by the parameter set $(t, t_z, t', \alpha, \mu, \Delta, \delta_1, \delta_2) = (1, -1, 0.4, \pm 0.2, -5.2, 0.1, 0.04, 0.2)$.

state with an isotropic gap indicated by recent ^{195}Pt -nuclear magnetic resonance (NMR) and ^{75}As -nuclear quadrupole (NQR) resonance measurements [148].

From the theoretical point of view, on the other hand, the E_{2g} state with a chiral d -wave pairing [149–151] and the B_{1u} state with an f -wave pairing [152, 153] have been proposed besides the fully-gapped A_{1g} order parameter suggested by the NMR measurement [148]. In the following discussion, we mainly assume the chiral E_{2g} state [149–151], which is consistent with broken TRS [147] and the decrease of spin susceptibility below T_c [148], but is incompatible with the nodeless gap structure [147, 148]. Especially, we focus on the gap structure on the C_{3v} -symmetric K - H line, since the presence of Weyl nodes [150] or Bogoliubov FSs [31, 57, 112] have been suggested on the line.

4.4.2 Classification on K - H line

Now we consider the gap structure on the K - H line with the C_{3v} symmetry, which has been already classified in Eq. (4.3.3). Since E_{2g} representation is not allowed for both $\bar{\lambda}_\alpha^k = E_{1/2}$ and $E_{3/2}$ in Eq. (4.3.3), the chiral d -wave state hosts nodes on the K - H line, which is incompatible with the nodeless gap structure. The B_{1u} state is consistent with the nodeless gap structure, if the Bloch state on the K - H line belongs to $E_{3/2}$, although this 1D representation is incompatible with broken TRS. The E_{1u} and E_{2u} superconducting states for the $E_{1/2}$ Bloch state are consistent with both nodeless gap and broken TRS. However, these odd-parity superconducting states are incompatible with NMR Knight shift measurement, which indicates the decrease of spin susceptibility below T_c [148].

Here, as an example, we discuss the topological classification of the E_{2g} pairing state. The compatibility relation reveals that E_{2g} of D_{6h} corresponds to E_g of D_{3d} . According to Table 4.2, E_g gap closes on the line irrespective of the angular momentum of normal Bloch states, as mentioned in the previous paragraph. However, Tables 4.3(b1) and 4.3(b2) shows the distinct topological classifications of such nodes depending on the angular momentum: $\mathbb{Z}_2 \oplus \mathbb{Z}$ for $\alpha = \pm 1/2$ and $\mathbb{Z} \oplus \mathbb{Z}$ for $\alpha = \pm 3/2$.

Next, we concretely identify the topological number. In the discussions below, we fix the superconducting order parameter to the 2E_g IR, which obtains the phase factor $+2\pi/3$ under a C_3 rotation:

$$C_3 \hat{\Delta}_+(\mathbf{k}) C_3^T = e^{+i2\pi/3} \hat{\Delta}_+(\mathbf{k}), \quad (4.4.1)$$

for \mathbf{k} on the C_3 -symmetric line. Some theoretical studies [149–151] have suggested such a TRS breaking chiral order parameter. Although only the PHS \mathfrak{C} is preserved in this TRS (CS) breaking superconducting state, the TRS \mathfrak{T} and the CS Γ recover by considering $\Delta_0 \rightarrow 0$ limit. Thus, in this limit, we can define the BdG Hamiltonian on the C_3 -symmetric line as Eq. (2.4.18) and

$$\mathbf{C}^\dagger(\mathbf{k}) = (c_{+1/2}^\dagger(\mathbf{k}), \mathfrak{T} c_{+1/2}^\dagger(\mathbf{k}) \mathfrak{T}^{-1}, \mathfrak{C} c_{+1/2}^\dagger(\mathbf{k}) \mathfrak{C}^{-1}, \Gamma c_{+1/2}^\dagger(\mathbf{k}) \Gamma^{-1}) \quad \text{for } \alpha = \pm 1/2, \quad (4.4.2)$$

$$\mathbf{C}^\dagger(\mathbf{k}) = (c_{+3/2}^\dagger(\mathbf{k}), \mathfrak{T} c_{+3/2}^\dagger(\mathbf{k}) \mathfrak{T}^{-1}, \mathfrak{C} c_{+3/2}^\dagger(\mathbf{k}) \mathfrak{C}^{-1}, \Gamma c_{+3/2}^\dagger(\mathbf{k}) \Gamma^{-1}) \quad \text{for } \alpha = \pm 3/2. \quad (4.4.3)$$

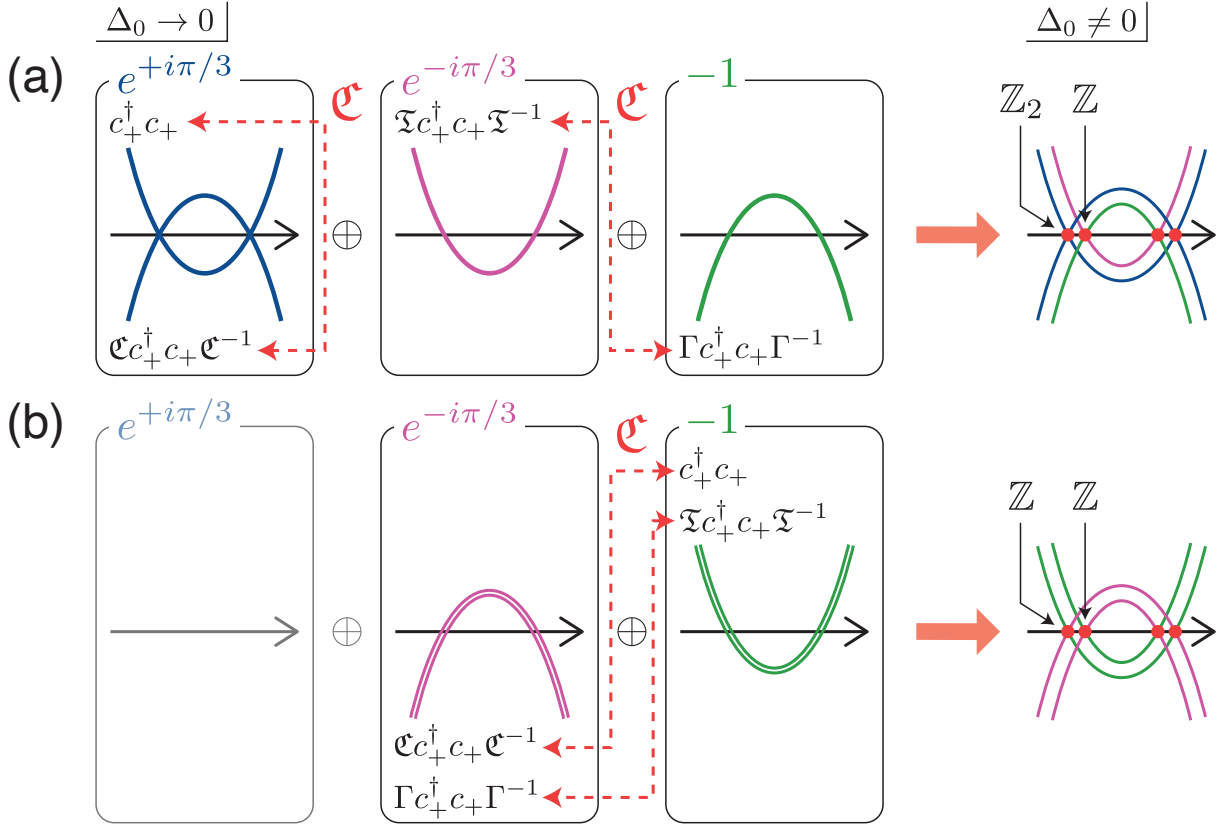


Figure 4.11: Band-theoretical picture of the 2E_g symmetric BdG Hamiltonian on a C_3 line for (a) $\alpha = \pm 1/2$ and (b) $\alpha = \pm 3/2$ normal Bloch states. c_+^\dagger in (a) and (b) is the abbreviated notation of $c_{+1/2}^\dagger(\mathbf{k})$ and $c_{+3/2}^\dagger(\mathbf{k})$, respectively. In the right panels, the red points represent nodes on the line. Although the particle bands and the hole bands for $\Delta_0 = 0$ are doubly degenerated, they split for a finite Δ_0 due to the TRS breaking in the superconducting state.

The BdG Hamiltonian matrix is written by the following effective single-band model:

$$\hat{H}_{\text{BdG}}(\mathbf{k}) = \begin{pmatrix} \xi(\mathbf{k})\sigma_0 - h(\mathbf{k})\Delta_0^2\sigma_z & \Delta_0\psi(\mathbf{k})i\sigma_y \\ (\Delta_0\psi(\mathbf{k})i\sigma_y)^\dagger & -(\xi(\mathbf{k})\sigma_0 - h(\mathbf{k})\Delta_0^2\sigma_z) \end{pmatrix}, \quad (4.4.4)$$

where $h(\mathbf{k})\Delta_0^2$ is the “pseudomagnetic” field representing the TRS breaking in the superconducting ordered state. The low-energy effective theory elucidates that such a field arises from the second-order perturbation of the *inter-band* pairing [36, 112], which cannot be generally neglected in real multiband systems. Note that the pseudomagnetic field does not break C_3 symmetry since it is parallel to the C_3 -symmetric axis.

Then, we discuss the topological numbers for $\alpha = \pm 1/2$ bands. Reflecting the C_3 symmetry, the BdG Hamiltonian matrix commutes with the threefold rotation matrix $\hat{U}_{\text{BdG}}(C_3)$:

$$[\hat{H}_{\text{BdG}}(\mathbf{k}), \hat{U}_{\text{BdG}}(C_3)] = 0, \quad (4.4.5)$$

which indicates that $\hat{H}_{\text{BdG}}(\mathbf{k})$ and $\hat{U}_{\text{BdG}}(C_3)$ are simultaneously block-diagonalized. There exists a unitary matrix \hat{V} such that

$$\hat{H}_{\text{BdG}}(\mathbf{k}) = \hat{V} \begin{pmatrix} \hat{H}_{e^{+i\pi/3}}(\mathbf{k}) & 0 & 0 \\ 0 & \hat{H}_{e^{-i\pi/3}}(\mathbf{k}) & 0 \\ 0 & 0 & \hat{H}_{-1}(\mathbf{k}) \end{pmatrix} \hat{V}^\dagger, \quad (4.4.6)$$

$$\hat{U}_{\text{BdG}}(C_3) = \hat{V} \begin{pmatrix} e^{+i\pi/3} \mathbf{1}_2 & 0 & 0 \\ 0 & e^{-i\pi/3} & 0 \\ 0 & 0 & -1 \end{pmatrix} \hat{V}^\dagger. \quad (4.4.7)$$

The block-diagonalized Hamiltonians $H_{e^{+i\pi/3}}(\mathbf{k})$, $H_{e^{-i\pi/3}}(\mathbf{k})$, and $H_{-1}(\mathbf{k})$ are written as follows:

$$H_{e^{+i\pi/3}}(\mathbf{k}) = \frac{1}{2} (c_{+1/2}^\dagger(\mathbf{k}), \mathfrak{C} c_{+1/2}^\dagger(\mathbf{k}) \mathfrak{C}^{-1}) \times \begin{pmatrix} \xi(\mathbf{k}) - h(\mathbf{k}) \Delta_0^2 & 0 \\ 0 & -(\xi(\mathbf{k}) - h(\mathbf{k}) \Delta_0^2) \end{pmatrix} \begin{pmatrix} c_{+1/2}(\mathbf{k}) \\ \mathfrak{C} c_{+1/2}(\mathbf{k}) \mathfrak{C}^{-1} \end{pmatrix}, \quad (4.4.8)$$

$$H_{e^{-i\pi/3}}(\mathbf{k}) = \frac{1}{2} \mathfrak{T} c_{+1/2}^\dagger(\mathbf{k}) \mathfrak{T}^{-1} (\xi(\mathbf{k}) + h(\mathbf{k}) \Delta_0^2) \mathfrak{T} c_{+1/2}(\mathbf{k}) \mathfrak{T}^{-1}, \quad (4.4.9)$$

$$H_{-1}(\mathbf{k}) = \frac{1}{2} \Gamma c_{+1/2}^\dagger(\mathbf{k}) \Gamma^{-1} (-\xi(\mathbf{k}) - h(\mathbf{k}) \Delta_0^2) \Gamma c_{+1/2}(\mathbf{k}) \Gamma^{-1}. \quad (4.4.10)$$

The band structures obtained by the Hamiltonian (4.4.6) are schematically shown in Fig. 4.11(a). For the $\Delta_0 \rightarrow 0$ limit, we can identify the eigenvalue of C_3 for each band by using the property of \mathfrak{T} , \mathfrak{C} , and Γ . Even when Δ_0 is finite, *i.e.*, the TRS \mathfrak{T} and the CS Γ are broken, the eigenvalues are not changed since the commutation relation Eq. (4.4.5) remains preserved. Then, the bands split due to the pseudomagnetic field $h(\mathbf{k}) \Delta_0^2$, and they create nodes at the zero energy because the *spin-singlet* 2E_g gap function cannot have offdiagonal components in the same eigenspace. The nodes corresponding to the $\alpha = -1/2$ particle band [the pink one in Fig. 4.11(a)] are obviously characterized by the \mathbb{Z} number,

$$\nu_- \equiv \#(\text{occupied states of } \hat{H}_{e^{-i\pi/3}}(\mathbf{k})) \in \mathbb{Z}. \quad (4.4.11)$$

On the other hand, the nodes corresponding to the $\alpha = +1/2$ particle band [the blue one in Fig. 4.11(a)] cannot be characterized by the filling, since there simultaneously exists the hole band belonging to the same eigenspace of C_3 . Instead, the PHS \mathfrak{C} with $\mathfrak{C}^2 = +E$ in the eigenspace ensures that these nodes are protected by the \mathbb{Z}_2 index [31, 54],

$$(-1)^{l_+} \equiv \text{sgn}[i^n \text{Pf}\{\hat{U}_{\mathfrak{C}, e^{+i\pi/3}} \hat{H}_{e^{+i\pi/3}}(\mathbf{k})\}] \in \mathbb{Z}_2, \quad (4.4.12)$$

with $n = \dim(\hat{H}_{e^{+i\pi/3}})/2$.

The topological numbers for $\alpha = \pm 3/2$ bands are obtained in the following. In this case, the BdG Hamiltonian matrix and the threefold rotation matrix are simultaneously block-diagonalized

as

$$\hat{H}_{\text{BdG}}(\mathbf{k}) = \hat{V} \begin{pmatrix} \hat{H}_{-1}(\mathbf{k}) & 0 \\ 0 & \hat{H}_{e^{-i\pi/3}}(\mathbf{k}) \end{pmatrix} \hat{V}^\dagger, \quad (4.4.13)$$

$$\hat{U}_{\text{BdG}}(C_3) = \hat{V} \begin{pmatrix} -\mathbf{1}_2 & 0 \\ 0 & e^{-i\pi/3} \mathbf{1}_2 \end{pmatrix} \hat{V}^\dagger, \quad (4.4.14)$$

where

$$H_{-1}(\mathbf{k}) = \frac{1}{2} (c_{+3/2}^\dagger(\mathbf{k}), \mathfrak{T} c_{+3/2}^\dagger(\mathbf{k}) \mathfrak{T}^{-1}) \times \begin{pmatrix} \xi(\mathbf{k}) - h(\mathbf{k}) \Delta_0^2 & 0 \\ 0 & \xi(\mathbf{k}) + h(\mathbf{k}) \Delta_0^2 \end{pmatrix} \begin{pmatrix} c_{+3/2}(\mathbf{k}) \\ \mathfrak{T} c_{+3/2}(\mathbf{k}) \mathfrak{T}^{-1} \end{pmatrix}, \quad (4.4.15)$$

$$H_{e^{-i\pi/3}}(\mathbf{k}) = \frac{1}{2} (\mathfrak{C} c_{+3/2}^\dagger(\mathbf{k}) \mathfrak{C}^{-1}, \Gamma c_{+3/2}^\dagger(\mathbf{k}) \Gamma^{-1}) \times \begin{pmatrix} -(\xi(\mathbf{k}) - h(\mathbf{k}) \Delta_0^2) & 0 \\ 0 & -(\xi(\mathbf{k}) + h(\mathbf{k}) \Delta_0^2) \end{pmatrix} \begin{pmatrix} \mathfrak{C} c_{+3/2}(\mathbf{k}) \mathfrak{C}^{-1} \\ \Gamma c_{+3/2}(\mathbf{k}) \Gamma^{-1} \end{pmatrix}. \quad (4.4.16)$$

Figure 4.11(b) shows the band structures obtained by the BdG Hamiltonian matrix (4.4.13). For both of the $\alpha = \pm 3/2$ particle bands [the green ones in Fig. 4.11(b)], the nodes on the C_3 -symmetric line are characterized by the \mathbb{Z} number,

$$\nu_\pm \equiv \#(\text{occupied states of } \hat{H}_{-1}(\mathbf{k})) \in \mathbb{Z}. \quad (4.4.17)$$

Irrespective of the IR of the normal band α , the TRS breaking even-parity 2E_g order parameter induces the band splitting and nodes on the C_3 -symmetric axis. These facts indicate that the nodes are parts of inflated Bogoliubov FSs, which are characterized by the Pfaffian of the antisymmetrized BdG Hamiltonian, $P(\mathbf{k}) \in \mathbb{Z}_2$, defined for all \mathbf{k} [31]. Indeed, the previous studies have suggested the existence of Bogoliubov FSs in SrPtAs [31, 57, 112]. In addition, our theory finds that the topological protection of the nodes on the high-symmetric line is differently defined in response to the IR α . Although the above intuitive discussions are based on the single-band model in the weak coupling limit, the topological protection ensures the stability of nodes against multiband effects.

4.5 Line nodes: CeCoIn₅ (Space group: $P4/mmm$)

4.5.1 Background

A Ce-based heavy-fermion compound CeCoIn₅ is a tetragonal lattice which is characterized by the space group $P4/mmm$ (D_{4h}^1). According to angle-resolved photoemission spectroscopy studies [154, 155], de Haas van Alphen (dHvA) measurements [156–159], and first-principles calculations [160, 161], the compound possesses 3D FSs crossing the high-symmetry Γ -Z line. CeCoIn₅

shows superconductivity at ambient pressure below 2.3 K [162]. Regarding the pairing symmetry in this compound, the presence of line nodes on the FS is indicated by specific heat and thermal conductivity measurement [163], and NQR relaxation rate $1/T_1$ [164]. Furthermore, scanning tunneling spectroscopy [165–167], field-angle-resolved measurements of thermal conductivity [39] and heat capacity [168], and torque magnetometry [169] strongly suggest that the superconducting order parameter possesses $d_{x^2-y^2}$ -wave (B_{1g}) symmetry.

4.5.2 Classification on Γ -Z line

We classify the gap structure on the Γ -Z line with the C_{4v} symmetry. According to the group-theoretical classification, the gap structure on the line is nodal for the $d_{x^2-y^2}$ -wave order parameter belonging to the B_{1g} IR of D_{4h} , irrespective of the angular momentum of the normal Bloch state (Table 4.2). The nodes on the axis are a part of a line node because of the following reason. In the BZ of D_{4h} , the Γ -Z-A-M plane is invariant under the diagonal mirror $M_{[110]}$. Therefore the combination of the compatibility relation

$$(B_{1g} \text{ of } D_{4h}) \downarrow C_{2h}^{[110]} = B_g, \quad (4.5.1)$$

and the gap classification on the plane (Table 3.1)

$$\bar{P}^k = A_g + 2A_u + B_u, \quad (4.5.2)$$

shows that a line node emerge on the [110] plane.⁶ The line node is protected by the 1D winding number $W_l \in \mathbb{Z}$ defined on a loop l encircling the nodal line [Eq. (3.2.10)], using the CS Γ [19, 55]. Thus the node is stable even when the mirror symmetry $M_{[110]}$ is broken as long as the CS exists. More generally, when the superconducting order parameter is even-parity and preserves TRS, nodes on a high-symmetry axis may be a part of (trivial) line nodes [see (L) in Table 4.3].

Table 4.3(g) shows that the topological classification for the B_{1g} order parameter is \mathbb{Z} . The orthogonality test for the CS Γ is $W_\alpha^\Gamma = 0$, which indicates that Γ changes the bases of the IR $\alpha = 1/2$ (3/2) to those of $\alpha' = 3/2$ (1/2). Therefore the \mathbb{Z} index is defined by the number of occupied states of the block-diagonalized Hamiltonian belonging to the IR α .

4.6 Point nodes: UCoGe (Space group: $Pnma$)

4.6.1 Background

UCoGe is a orthorhombic superconductor whose crystal structure belongs to the nonsymmorphic space group $Pnma$ (D_{2h}^{16}) [170]. In this material, superconductivity at ambient pressure coexists with ferromagnetism [171, 172], and therefore, odd-parity superconductivity is strongly suggested.

⁶The same result is obtained for the [1–10] plane.

The high-pressure superconducting phase [171–177] (S_2 phase in Ref. [174]), where TRS recovers by the vanishing ferromagnetic moments [173–175, 178], is also expected to be odd-parity superconductivity, since it is continuously connected to the FM superconducting phase [173–177].

Although the symmetry of superconductivity in UCoGe is still under debate, recent studies have suggested the possibility of topological crystalline superconductivity, which is characterized by \mathbb{Z}_4 and/or \mathbb{Z}_2 indices, for all odd-parity IRs (A_u , B_{1u} , B_{2u} , and B_{3u}) of the superconducting order parameter [110, 179]. Especially, when the order parameter belongs to the B_{1u} IR of D_{2h} , point nodes emerge on the Γ -Z line [110]. In the following discussion, therefore, we focus on the B_{1u} order parameter as a candidate of the odd-parity superconducting order.

4.6.2 Classification on Γ -Z line

Considering the paramagnetic high-pressure superconducting phase, we classify the gap structure on the Γ -Z line which has C_{2v} symmetry. Since the group-theoretical classification of C_{2v} -symmetric line is $\bar{P}^k = A_g + A_u + B_{2u} + B_{3u}$ (Table 4.2), point nodes appear on the line in the B_{1u} superconducting state. Note that the gap classification results on the other eleven C_{2v} -symmetric lines in the BZ are changed due to the nonsymmorphic symmetry of $Pnma$ [110]. According to Table 4.3(e), the point nodes are characterized by the \mathbb{Z}_2 topological number.

Now we identify the \mathbb{Z}_2 topological number. First, the IR of the little cogroup C_{2v} is written by

$$\bar{\gamma}_{1/2}^k(E) = \sigma_0, \quad (4.6.1a)$$

$$\bar{\gamma}_{1/2}^k(C_{2z}) = -i\sigma_z, \quad (4.6.1b)$$

$$\bar{\gamma}_{1/2}^k(\mathcal{M}_y) = -i\sigma_y, \quad (4.6.1c)$$

$$\bar{\gamma}_{1/2}^k(\mathcal{M}_x) = -i\sigma_x, \quad (4.6.1d)$$

where the bases [$c_{\pm i}^\dagger(\mathbf{k})$] are the eigenstates of C_{2z} with the eigenvalues $\pm i$. Thus the minimal BdG Hamiltonian is expressed by the four bases, $c_{\pm i}^\dagger(\mathbf{k})$ and $\mathfrak{C} c_{\pm i}^\dagger(\mathbf{k}) \mathfrak{C}^{-1}$. Here, we remark that the PHS \mathfrak{C} changes the eigenvalue of C_{2z} since \mathfrak{C} is an antiunitary operator with $[\mathfrak{C}, C_{2z}] = 0$ in the B_{1u} superconducting state. Furthermore, Eq. (4.6.1) shows that the mirror operator \mathcal{M}_y also changes the eigenvalue of C_{2z} . Therefore a new PHS operator $\tilde{\mathfrak{C}} \equiv \mathfrak{C} \mathcal{M}_y$ preserves the eigenvalue of C_{2z} , and it has the following relation,

$$\tilde{\mathfrak{C}}^2 = \mathfrak{C}^2 \mathcal{M}_y^2 = +E, \quad (4.6.2)$$

where we use $[\mathfrak{C}, \mathcal{M}_y] = 0$ for the B_{1u} order parameter. As a result the BdG Hamiltonian matrix $\hat{H}_{\text{BdG}}(\mathbf{k})$ are decomposed by C_{2z} eigen-sectors $\hat{H}_\pm(\mathbf{k})$, each of which has the PHS-like operator $\tilde{\mathfrak{C}}$. Due to the symmetry, the \mathbb{Z}_2 number can be defined in each sector [31, 54]:

$$(-1)^{l_\pm} \equiv \text{sgn}[i^n \text{Pf}\{\hat{U}_{\tilde{\mathfrak{C}}, \pm} \hat{H}_\pm(\mathbf{k})\}] \in \mathbb{Z}_2, \quad (4.6.3)$$

with $n = \dim(\hat{H}_\pm)/2$.

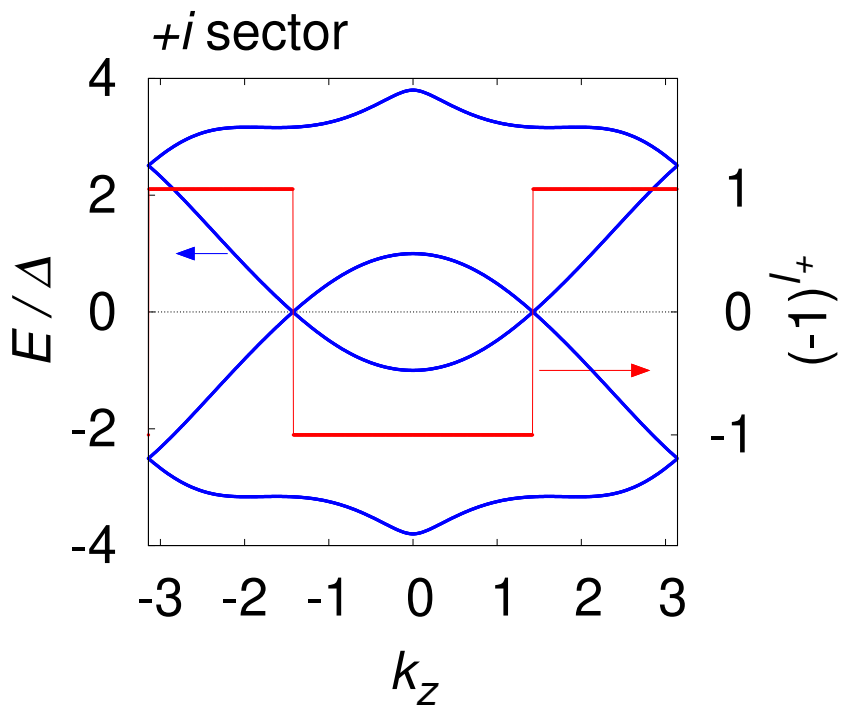


Figure 4.12: The quasiparticle energy dispersion (blue lines) and the \mathbb{Z}_2 topological number (red line) on the Γ -Z line for the $+i$ sector of the block-diagonalized BdG Hamiltonian. The result for the $-i$ sector is the same as the $+i$ case. We adopt the effective model in Refs. [110, 179]. The parameters $(t_1, t_2, t_3, t_{ab}, t'_{ab}, \mu, t'_1, \alpha) = (1, 0.2, 0.1, 0.5, 0.1, -0.5, 0.1, 0.3)$ are assumed so that the Γ -FSs of UCoGe are reproduced.

We demonstrate the topological crystalline point nodes by using the effective four-sublattice single-orbital model introduced in Refs. [110, 179]. Figure 4.12 shows the eigenvalues of the BdG Hamiltonian and the \mathbb{Z}_2 index for the $+i$ eigen-sector on the Γ - Z line. Obviously, we find that the \mathbb{Z}_2 topological number $(-1)^{l_+}$ changes at the point nodes.

4.7 MoS₂ (Space group: $P6_3/mmc$)

4.7.1 Background

MoS₂ is a member of the group-VI transition-metal dichalcogenides MX_2 ($M = \text{Mo, W}$; $X = \text{S, Se, Te}$). Superconductivity of MoS₂ has been observed in the ion-gated atomically thin 2D system [130, 180–183], and in the bulk intercalated system [184, 185]. In these electron-doped systems, Mo- d_{z^2} orbitals contribute to the spin-split lowest conduction bands, which form FSs around the K point [186]. However, the FSs do not cross the K - H line, because the lowest conduction bands are almost dispersionless along this line due to the absence of the nearest inter-layer hopping [133]. On the other hand, $d_{x^2-y^2} \pm id_{xy}$ orbitals of Mo ions contribute to the spin-split top valence bands [186], which have sizable dispersion on the K - H line in the 2H stacking structure [133]. Thus, these top valence bands may form FSs crossing the K - H line in a hole-doped MoS₂.

4.7.2 Classification on K - H line

In the material characterized by the hexagonal space group $P6_3/mmc$, the superconducting gap on the K - H line is classified by Eq. (4.3.3). The result of the gap classification in each material is discussed below.

Although the symmetry of superconductivity in MoS₂ has not been determined, a recent theoretical study [187] suggests the conventional BCS state (A_{1g}) in the paramagnetic regime, and the pair-density-wave (PDW) state (B_{2u}) under the external magnetic field. Since Eq. (4.3.3) contains A_{1g} and B_{2u} representations for both $\bar{\lambda}_\alpha^k = E_{1/2}$ and $E_{3/2}$, the superconducting gap opens on the K - H line irrespective of the Bloch-state angular momentum. The A_{1g} symmetry is supported by recent first-principle calculations, which take into account electron-phonon interactions [188–190]. On the other hand, topological superconductivity in electron-doped [191] and hole-doped [192] monolayer MoS₂ has been theoretically proposed, where the pairing symmetry is classified into A_1 or E representation of the point group C_{3v} . Assuming that the pairing symmetry in bulk MoS₂ is the same as that in monolayer MoS₂, these representations are induced to D_{6h} as

$$A_1 \uparrow D_{6h} = A_{1g} + B_{2g} + A_{2u} + B_{1u}, \quad (4.7.1)$$

$$E \uparrow D_{6h} = E_{1g} + E_{2g} + E_{1u} + E_{2u}. \quad (4.7.2)$$

Table 4.7: Gap structure on the K - H line in bulk MoS₂ where the pairing symmetry belongs to A_1 or E representation of C_{3v} . “PS” in the first and second columns represents pairing symmetry.

PS in C_{3v}	PS in D_{6h}	Bloch state	Gap structure
A_1	A_{1g}	$E_{1/2}, E_{3/2}$	Gap
	B_{2g}	$E_{1/2}, E_{3/2}$	Gap
	A_{2u}	$E_{1/2}$	Point node
		$E_{3/2}$	Gap
	B_{1u}	$E_{1/2}$	Point node
		$E_{3/2}$	Gap
E	E_{1g}	$E_{1/2}, E_{3/2}$	Point node
	E_{2g}	$E_{1/2}, E_{3/2}$	Point node
	E_{1u}	$E_{1/2}$	Gap
		$E_{3/2}$	Point node
	E_{2u}	$E_{1/2}$	Gap
		$E_{3/2}$	Point node

Therefore, the presence or absence of point nodes on the K - H line depends on the choice of the basis function of the A_1 or E representation, which is summarized in Table 4.7. The superconducting gap structure depends on the effective angular momentum j_z when the pairing symmetry is A_{2u} , B_{1u} , E_{1u} , or E_{2u} .

4.8 UBe₁₃ (Space group: $Fm\bar{3}c$)

4.8.1 Background

Although superconductivity in UBe₁₃ was discovered in 1983 [193], the nature and the symmetry of superconductivity are still under debate. A point-nodal p -wave [194] and line-nodal [195] superconductivity have been proposed, while recent angle-resolved heat-capacity measurements have suggested a fully opened superconducting gap [196]. Furthermore, another mystery about UBe₁₃ is the emergence of a second phase transition in the superconducting state when a small amount of U atoms are replaced by Th [197, 198]; μ SR [199] and thermal-expansion [200] experiments have reported the existence of four superconducting phases.

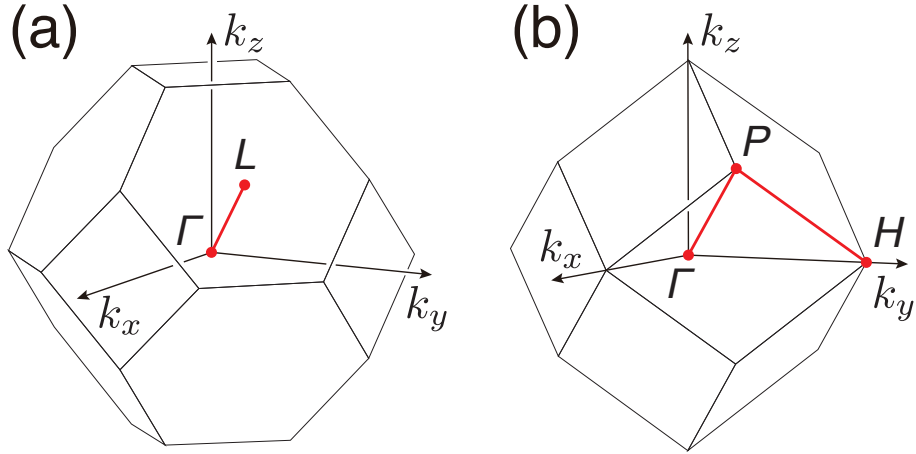


Figure 4.13: The first BZ of (a) face-centered cubic lattice and (b) body-centered cubic lattice. The red lines show threefold rotation symmetric axes.

4.8.2 Classification on Γ -L line

The space group of UBe₁₃ is face-centered cubic $Fm\bar{3}c$, where the BZ has a threefold rotation axis Γ -L [see Fig. 4.13(a)]. Although first-principle calculations show only a tiny FS crossing the Γ -L line [201, 202], such a FS structure has not been confirmed by experiments. Thus, we carry out the gap classification on the Γ -L line, assuming the existence of FSs in the [111] direction. The little group on the Γ -L line has C_{3v} symmetry, which results in the two distinct representations of the Cooper pair wave function given by Eq. (4.3.2), corresponding to two representations $\bar{\lambda}^k = E_{1/2}$ and $E_{3/2}$. Inducing \bar{P}^k to the original crystal point group O_h , we obtain the induced representation $\bar{P}^k \uparrow O_h$ summarized in the following equations:

$$\bar{P}^k \uparrow O_h = \begin{cases} A_{1g} + T_{2g} + A_{1u} + E_u + T_{1u} + 2T_{2u} & (\bar{\lambda}^k = E_{1/2}), \\ A_{1g} + T_{2g} + 2A_{1u} + A_{2u} + T_{1u} + 2T_{2u} & (\bar{\lambda}^k = E_{3/2}). \end{cases} \quad (4.8.1)$$

For UBe₁₃, the E_u state [203, 204] and the accidental $A_{1u} + A_{2u}$ mixed state [203] have been proposed, consistent with the double transition in $U_{1-x}Th_xBe_{13}$. In the former E_u state, j_z -dependent point nodes emerge: the superconducting gap opens for $\bar{\lambda}^k = E_{1/2}$, while point nodes appear for $\bar{\lambda}^k = E_{3/2}$ [see Eq. (4.8.1)]. Previous studies based on the E_u scenario simply assumed the $E_{1/2}$ Bloch state and obtained the full gap superconducting state in the TRS preserving A and C phases [203]. Their results are not valid when the FS crossing the Γ -L line is formed by the $E_{3/2}$ Bloch state. In the accidentally mixed state, on the other hand, the A_{1u} component makes the gap open irrespective of the angular momentum of the Bloch state. The A_{2u} component gives rise to the gap only for the $E_{3/2}$ Bloch state. In both E_u and $A_{1u} + A_{2u}$ scenarios, it is necessary to identify the angular momentum of Bloch states in order to relate the symmetry and gap structure of superconductivity. The experimental data should be carefully interpreted by taking into account this fact.

4.9 PrOs₄Sb₁₂ (Space group: $Im\bar{3}$)

4.9.1 Background

PrOs₄Sb₁₂ is a heavy-fermion superconductor with the filled skutterudite structure RT_4X_{12} (R = rare earth or U; T = Fe, Ru, Os; X = P, As, Sb). Many studies have reported the manifestation of unconventional superconductivity in PrOs₄Sb₁₂ [205, 206]. For example, multiple superconducting phases have been suggested by specific-heat [207, 208] and thermal transport [209] measurements. However, the superconducting pairing symmetry in PrOs₄Sb₁₂ remains unclear even now: a point-nodal superconductivity has been suggested by some NQR [210], penetration depth [211], and specific heat [207, 208] studies, while other thermal conductivity [212], μ SR [213], and NQR [214] measurements have proposed a fully gapped FS. Furthermore, several experiments have observed TRS breaking in the low-temperature and low-magnetic-field superconducting phase (B phase) [215, 216].

4.9.2 Classification on Γ - P and P - H lines

Here we carry out a group-theoretical analysis for the gap structure of PrOs₄Sb₁₂. PrOs₄Sb₁₂ has a body-centered cubic space group $Im\bar{3}$, where the BZ has threefold rotation axes Γ - P and P - H [see Fig. 4.13(b)]. The FS topology of PrOs₄Sb₁₂ has been confirmed by the combination of dHvA experiment and first-principles calculation [217]. The determined FS consists of three parts, two of which cross the Γ - P line and the other does the P - H line. Therefore, the gap structure on these lines is worth considering. The little group on the Γ - P and P - H lines has C_3 symmetry, which results in two representations $\bar{\lambda}^k = E_{1/2}$ and $2B_{3/2}$, given by Table 4.1(b). Corresponding to these two Bloch states, the Cooper pair wave function has two nonequivalent representations as shown in Table 4.2. Thus, the induced representation $\bar{P}^k \uparrow T_h$ is obtained in the following equations:

$$\bar{P}^k \uparrow T_h = \begin{cases} A_g + T_g + A_u + E_u + 3T_u & (\bar{\lambda}^k = E_{1/2}), \\ A_g + T_g + 3A_u + 3T_u & (\bar{\lambda}^k = 2B_{3/2}). \end{cases} \quad (4.9.1)$$

Theoretical studies have suggested various possibilities of the pairing symmetry in PrOs₄Sb₁₂ [218–223]. For example, the 3D T_g and T_u states [218], the mixed $A_g + E_g$ state with a $s + g$ -wave pairing [219], and that with a $s + id$ -wave pairing [221] have been proposed. In these cases, the superconducting gap opens on the Γ - P and P - H lines irrespective of the angular momentum of the Bloch state. However, the j_z -dependent point nodes may emerge, if the order parameter belongs to the E_u representation [see Eq. (4.9.1)].

Chapter 5

Conclusion

In this thesis, we investigate the gap structures in various unconventional superconductors with spin-orbit coupling and multi-degrees of freedom, by using the modern classification theory of superconducting gap nodes.

In Chapter 2, we present the recently developed classification methods of superconducting gap, from both aspects of group theory and topology [18–21]. The methods take into account space group symmetry and higher-spin normal Bloch states, which enables us to reveal novel types of nodal structures beyond the order parameter analysis by the Sigrist-Ueda method. Moreover, the combination of group-theoretical and topological classifications offers the complementary understanding of nodes appearing in unconventional superconductors: the group-theoretical analysis helps us to easily search symmetry-protected superconducting nodes, while the property of topological number tells us the stability of such nodes. Our classification theory motivates the research community to reacknowledge the importance of such complementary studies, and to expect that all crystal symmetry-protected nodes are protected by topology.

In Chapter 3, we completely classify gap structures on high-symmetry planes (mirror- or glide-invariant planes) in the Brillouin zone [20]. When the system has symmetry including non-primitive translation parallel to a twofold axis, the Cooper pair wave functions on the basal plane and the zone face, which are perpendicular to the twofold axis, have different representations as a consequence of the nonsymmorphic symmetry. In this case, therefore, line nodes (or a gap opening) protected by nonsymmorphic symmetry may emerge on the Brillouin zone boundary. We classified the gap structure of all the centrosymmetric space groups. From the list of space groups, we may understand the symmetry-protected line node for each crystal, magnetic, and superconducting symmetries. Furthermore, we have established the relationship between such symmetry-protected line nodes and Majorana flat bands using a topological argument [19]. The zero-dimensional topological number not only reflects the group theoretical results, but also relates to the one-dimensional topological number that ensures the existence of Majorana flat bands. By analyzing the relationship between the two topological numbers, we can categorize the symmetry-protected line nodes into three distinct classes. Each class is distinguished by the Majorana flat bands and the symmetry-protected line

nodes may be distinguished through surface sensitive experiments such as tunneling conductance measurements. Finally, as an example, we suggest the nonsymmorphic symmetry-protected gap structures in the $-++-$ (magnetic octupole) state of Sr_2IrO_4 [18]. We confirmed the symmetry-based classification results by the realistic model for Sr_2IrO_4 .

In Chapter 4, on the basis of the symmetry and topology we classified superconducting gap structure on high-symmetry n -fold lines in the Brillouin zone [20, 21]. First, we execute the comprehensive group-theoretical classification; on threefold and sixfold axes, the gap classification depends on the total angular momentum of the normal Bloch state j_z , while that is unique on twofold and fourfold axes. Next, we find that the topological analysis completely corresponds with the above group-theoretical classification; all nodes shown by group theory are characterized by a zero-dimensional \mathbb{Z} or \mathbb{Z}_2 index. Thus the symmetry-protected nodes are topologically protected. Such *topological crystalline superconducting nodes* on the high-symmetry axes are classified into three types: point nodes, a part of line nodes, and a part of surface nodes (Bogoliubov Fermi surfaces). Furthermore, we applied such classification to various candidate superconductors: UPt_3 , SrPtAs , CeCoIn_5 , UCoGe , MoS_2 , UBe_{13} , and $\text{PrOs}_4\text{Sb}_{12}$. Especially, we showed that the structure of Weyl nodes also depends on the angular momentum of the normal Bloch state in the time-reversal symmetry breaking B phase of UPt_3 , reflecting the j_z -dependent gap structure on the C_{3v} -symmetric K - H line.

This thesis offers almost complete classification of superconducting gap nodes on high-symmetry regions in the Brillouin zone. However, there are several remaining issues to be uncovered. First, gap classification on high-symmetry lines may be changed by taking *nonsymmorphic* symmetry into account, although only symmorphic symmetry is considered in Chapter 4. Indeed, Ref. [110] shows gap classification for the nonsymmorphic magnetic space group $Pnma1'$, which gives nontrivial gap structures on C_{2v} -symmetric hinges of the Brillouin zone with *glide symmetry*. Secondly, it may be interesting to investigate the relationship among more than one topological numbers characterizing nodes on high-symmetry axes. In time-reversal symmetry breaking superconductors, for example, it may be possible to reveal such relationship between a two-dimensional Chern number and a zero-dimensional topological number, which enables us to understand the stability of the Weyl nodes and the corresponding surface Majorana arc states. Finally, our classification theory can be extended to lower-dimensional superconductors and/or spin-orbit decoupled superconductors; such classification may be useful in determining superconducting symmetry of a twisted bilayer graphene, which has recently attracted much attention. The above ideas are interesting problems and have the potential to find new physical phenomena in future.

Appendix A

Representation theory

A.1 Wigner criterion

We review the method and meaning of the Wigner criterion used in Secs. 2.1 and 2.3. For detailed proofs of the criterion, see Refs. [38, 48].

A.1.1 Formulation

We first suppose that H is a unitary group and α is a certain d_α -dimensional IR of H , which has the basis functions ψ_i ($i = 1, 2, \dots, d_\alpha$). ψ_i transforms under the symmetry operation $h \in H$ as

$$h\psi_i = \sum_{j=1}^{d_\alpha} \psi_j [D_\alpha(h)]_{ji}, \quad (1.1.1)$$

where D_α is a representation matrix of the IR α . Then, we consider whether the degeneracy of the representation increases or not by adding an antiunitary operator a to the group: $H + aH$. The problem can be solved by the Wigner criterion [38, 48]:

$$W_\alpha^a \equiv \frac{1}{|H|} \sum_{h \in H} \omega(ah, ah) \chi[D_\alpha((ah)^2)] = \begin{cases} 1 & (\text{a}), \\ -1 & (\text{b}), \\ 0 & (\text{c}). \end{cases} \quad (1.1.2)$$

Here, $\{\omega(h_1, h_2)\} \in Z^2(H + aH, U(1)_\phi)$ is a factor system arising in a representation

$$\omega(h_1, h_2) U_{h_1 h_2} = \begin{cases} U_{h_1} U_{h_2} & (\phi(h_1) = 1), \\ U_{h_1} U_{h_2}^* & (\phi(h_1) = -1), \end{cases} \quad (1.1.3)$$

where $\phi : H + aH \rightarrow \mathbb{Z}_2 = \{\pm 1\}$ is an indicator for unitary/antiunitary symmetry. The meanings of the cases (a), (b), and (c) are shown in the following.

1. There is no additional degeneracy due to the presence of the antiunitary operator a , because $\{\psi_i\}$ and $\{a\psi_i\}$ are not independent.
2. The presence of the operator a gives rise to additional degeneracy, because $\{a\psi_i\}$ is linearly independent of $\{\psi_i\}$ although they belong to the same IR α .
3. The degeneracy is doubled by applying a , because the basis $\{a\psi_i\}$ belongs to a representation α' inequivalent to α .

A.1.2 Example: C_3 symmetry

As an example of the Wigner criterion, we see the rotational property of the basis of spin angular momentum $\psi = |s_z\rangle$. In a continuous space, $|s_z\rangle$ transforms under the θ rotation $C(\theta)$ around the z axis as

$$C(\theta) |s_z\rangle = e^{i\theta s_z} |s_z\rangle. \quad (1.1.4)$$

Next, we discuss threefold-rotational symmetric system $H = \{E, C_3, (C_3)^2\}$. In this symmetry, the continuous rotational symmetry $C(\theta)$ is restricted to discrete symmetries: $\theta = 0, 2\pi/3$, and $4\pi/3$. Now we investigate the additional degeneracy by imposing the TRS \mathcal{T} on the system for $s_z = +3/2$ and $+1/2$.

2. $s_z = +3/2$ case.

The eigenvalues $e^{i\theta s_z}$ in Eq. (1.1.4), namely the 1D IR matrices $D_{+3/2}$ with the basis $|+\frac{3}{2}\rangle$, are given by

$$D_{+3/2}(E) = 1, \quad (1.1.5a)$$

$$D_{+3/2}(C_3) = -1, \quad (1.1.5b)$$

$$D_{+3/2}((C_3)^2) = 1. \quad (1.1.5c)$$

Then, by adding the TRS \mathcal{T} , the Wigner criterion leads to

$$\begin{aligned} W_{+3/2}^{\mathcal{T}} &= \frac{1}{3} \sum_{h \in H} \omega(\mathcal{T}h, \mathcal{T}h) \chi[D_{+3/2}((\mathcal{T}h)^2)] \\ &= \frac{1}{3}(-1 - 1 - 1) = -1. \end{aligned} \quad (1.1.6)$$

Note that \mathcal{T} commutes with all operators in H , and $\mathcal{T}^2 = (C_3)^3 = -E$. Eq. (1.1.6) indicates that $\mathcal{T}|+\frac{3}{2}\rangle \propto |- \frac{3}{2}\rangle$ has the same rotational property as $|+\frac{3}{2}\rangle$:

$$D_{-3/2}(E) = 1, \quad (1.1.7a)$$

$$D_{-3/2}(C_3) = -1, \quad (1.1.7b)$$

$$D_{-3/2}((C_3)^2) = 1, \quad (1.1.7c)$$

therefore,

$$D_{-3/2} \equiv D_{+3/2}. \quad (1.1.8)$$

In other words, the basis functions $|+\frac{3}{2}\rangle$ and $|-\frac{3}{2}\rangle$ belong to the same IR. However, the presence of the TRS \mathcal{T} gives rise to additional degeneracy, since the basis $|-\frac{3}{2}\rangle$ is linearly independent of $|+\frac{3}{2}\rangle$.

3. $s_z = +1/2$ case.

From Eq. (1.1.4), the 1D IR matrices $D_{+1/2}$ with the basis $|+\frac{1}{2}\rangle$ are written by

$$D_{+1/2}(E) = 1, \quad (1.1.9a)$$

$$D_{+1/2}(C_3) = e^{+i\pi/3}, \quad (1.1.9b)$$

$$D_{+1/2}((C_3)^2) = e^{+i2\pi/3}. \quad (1.1.9c)$$

Thus the Wigner criterion for the TRS \mathcal{T} is calculated by

$$\begin{aligned} W_{+1/2}^{\mathcal{T}} &= \frac{1}{3} \sum_{h \in H} \omega(\mathcal{T}h, \mathcal{T}h) \chi[D_{+1/2}((\mathcal{T}h)^2)] \\ &= \frac{1}{3}(-1 - e^{i2\pi/3} + e^{i\pi/3}) = 0. \end{aligned} \quad (1.1.10)$$

Equation (1.1.10) indicates that $\mathcal{T}|+\frac{1}{2}\rangle \propto |-\frac{1}{2}\rangle$ has the nonequivalent rotational property to $|+\frac{1}{2}\rangle$:

$$D_{-1/2}(E) = 1, \quad (1.1.11a)$$

$$D_{-1/2}(C_3) = e^{-i\pi/3}, \quad (1.1.11b)$$

$$D_{-1/2}((C_3)^2) = e^{-i2\pi/3}, \quad (1.1.11c)$$

therefore,

$$D_{-1/2} \neq D_{+1/2}. \quad (1.1.12)$$

Due to the bases of nonequivalent IRs $|+\frac{1}{2}\rangle$ and $|-\frac{1}{2}\rangle$, the degeneracy is doubled by applying the TRS \mathcal{T} .

A.2 Orthogonality test

We explain the formulation of the orthogonality test for CS, used in Sec. 2.3. First, let H a (unitary) crystal point group and α is a certain d_α -dimensional IR of H which has the basis functions ψ_i ($i = 1, 2, \dots, d_\alpha$). ψ_i transforms under the symmetry operation $h \in H$ as

$$h\psi_i = \sum_{j=1}^{d_\alpha} \psi_j [D_\alpha(h)]_{ji}, \quad (1.2.1)$$

where D_α is a representation matrix of the IR α . Then, we consider the situation that the system has additional CS Γ : $H + \Gamma H$. Let $\{\omega(h_1, h_2)\} \in Z^2(H + \Gamma H, U(1))$ be a factor system of $H + \Gamma H$. The orthogonality between $\{\psi_i\}$ and $\{\Gamma\psi_i\}$ is investigated in the following.

The basis $\Gamma\psi_i$ is transformed by $h \in H$ as

$$\begin{aligned} h(\Gamma\psi_i) &= \Gamma(\Gamma^{-1}h\Gamma)\psi_i \\ &= \sum_{j=1}^{d_\alpha} (\Gamma\psi_j)\omega(\Gamma^{-1}, h\Gamma)\omega(h, \Gamma)[D_\alpha(\Gamma^{-1}h\Gamma)]_{ji}, \\ &= \sum_{j=1}^{d_\alpha} (\Gamma\psi_j) \frac{\omega(h, \Gamma)}{\omega(\Gamma, \Gamma^{-1}h\Gamma)} [D_\alpha(\Gamma^{-1}h\Gamma)]_{ji}, \end{aligned} \quad (1.2.2)$$

where we use the 2-cocycle condition

$$\omega(h_1, h_2)\omega(h_1h_2, h_3) = \omega(h_1, h_2h_3)\omega(h_2, h_3), \quad (1.2.3)$$

for $h_1, h_2, h_3 \in H + \Gamma H$. We remark that H is not changed under the CS: $\Gamma^{-1}H\Gamma = H$. In other words, the representation matrix of H with the bases $\{\Gamma\psi_i\}$ is given by $\frac{\omega(h, \Gamma)}{\omega(\Gamma, \Gamma^{-1}h\Gamma)} D_\alpha(\Gamma^{-1}h\Gamma)$. Next, we recall the orthogonality relation between two IR matrices D_α and D_β [38, 48],

$$\frac{1}{|H|} \sum_{h \in H} [D_\alpha(h)]_{ij} [D_\beta(h)^*]_{kl} = \frac{1}{d_\alpha} \delta_{\alpha\beta} \delta_{ik} \delta_{jl}. \quad (1.2.4)$$

By taking $i = j$ and $k = l$, we calculate the summation of Eq. (1.2.4) over i and k :

$$\begin{aligned} \frac{1}{|H|} \sum_{h \in H} \sum_{i=1}^{d_\alpha} [D_\alpha(h)]_{ii} \sum_{k=1}^{d_\beta} [D_\beta(h)^*]_{kk} &= \frac{\delta_{\alpha\beta}}{d_\alpha} \sum_{i=1}^{d_\alpha} \sum_{k=1}^{d_\alpha} \delta_{ik}, \\ \therefore \frac{1}{|H|} \sum_{h \in H} \chi[D_\alpha(h)] \chi[D_\beta(h)^*] &= \delta_{\alpha\beta}. \end{aligned} \quad (1.2.5)$$

Finally, Eqs. (1.2.2) and (1.2.5) lead to the orthogonality test between $\{\psi_i\}$ and $\{\Gamma\psi_i\}$,

$$\begin{aligned} \frac{1}{|H|} \sum_{h \in H} \frac{\omega(h, \Gamma)^*}{\omega(\Gamma, \Gamma^{-1}h\Gamma)^*} \chi[D_\alpha(h)] \chi[D_\alpha(\Gamma^{-1}h\Gamma)^*] \\ = \begin{cases} 1 & (\{\psi_i\} \text{ and } \{\Gamma\psi_i\} \text{ are equivalent}), \\ 0 & (\{\psi_i\} \text{ and } \{\Gamma\psi_i\} \text{ are nonequivalent}), \end{cases} \end{aligned} \quad (1.2.6)$$

which is nothing but Eq. (2.3.4).

Appendix B

Other remarks

B.1 Sr_2IrO_4

B.1.1 Accidental gap of A_{1g} state at $k_y = \pi/a$ in $-+ +-$ state

Gap classification using the space group symmetry reveals that the A_{1g} gap functions in the $-+ +-$ state possess vertical line nodes on the ZF $k_y = \pi/a$, although the A_{1g} representation is allowed on the BP $k_y = 0$. In our numerical calculation, however, a small gap appears in the excitation spectrum on the ZF although the magnitude of the gap is smaller than that on BP (see Fig. B.1). That is because single-particle states are accidentally fourfold degenerate all over the ZF $k_y = \pi/a$ in our model. This fourfold degeneracy is not protected by symmetry except for on some high-symmetry lines (Sec. B.1.2). The group theoretical analysis of gap classification can be applied only to the intra-band gap, which are diagonal components of the band-based order parameter matrix [13, 15, 16]. In ordinary cases, intra-band gap is equivalent to the excitation gap since inter-band gap (offdiagonal components of the band-based order parameter matrix) hardly affects the energy spectrum near $E = 0$. In the presence of (nearly) fourfold degeneracy, however, inter-band gap may induce excitation gap [13]. Then, the gap nodes expected from the gap classification can be lost. Indeed, such a gap opening changes the nodal line to nodal loops in UPt_3 [13]. In many cases including UPt_3 , however, the inter-band gap appears only on the high-symmetry lines, and the dimension of nodes is not altered. Our tight-binding model accidentally has fourfold degeneracy on the plane, and therefore, we obtain the excitation gap on the ZF $k_y = \pi/a$. We believe that the gap at $k_y = \pi/a$ is lifted by taking into account all the spin-orbit couplings allowed by the symmetry.

B.1.2 Symmetry-protected Dirac line nodes on BZ boundary in $-+ +-$ state

We show the symmetry protection of the fourfold degeneracy on the BZ boundary in $-+ +-$ state. The fourfold degeneracy appears at $U-R$, $R-T$, $T-Y$, and $Y-S$ lines in the first BZ (Fig. B.2). Using the little group on each line, we prove the presence of the degeneracy by symmetry.

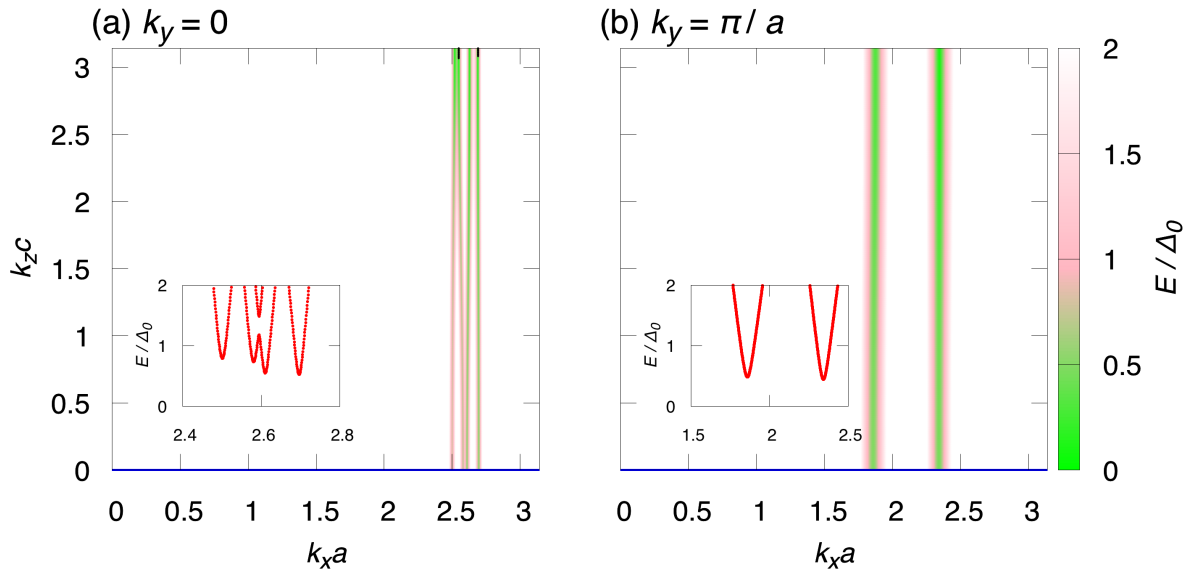


Figure B.1: (Color online) The contour plot of quasiparticle energy dispersion E in the s -wave superconducting state normalized by the order parameter Δ_0 on (a) $k_y = 0$ and (b) $k_y = \pi/a$. The insets in (a) and (b) show the dispersion E / Δ_0 along the respective blue line. (a) On the BP $k_y = 0$, quasiparticle in almost whole region except for on the BZ boundary $k_z = \pi/c$ are gapped. This is consistent with the gap classification. (b) On the ZF $k_y = \pi/a$, line nodes vanish in disagreement with the gap classification.

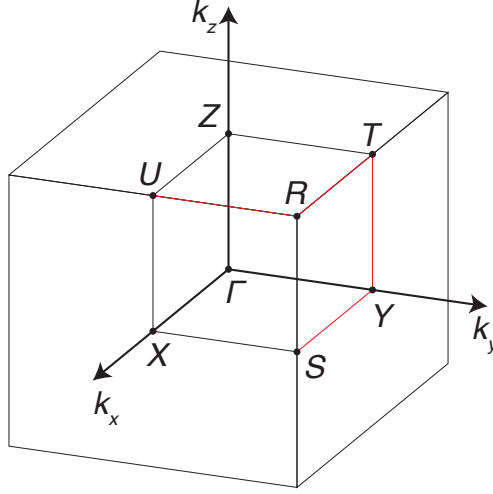


Figure B.2: (Color online) The first BZ for primitive orthorhombic lattice. Single particle states are fourfold degenerate on the red lines.

On the U - R line ($k_y = \pi/a$ and $k_z = \pi/c$), the magnetic little group is given by

$$\mathcal{M}^k = \mathcal{G}^k + \mathfrak{T}\mathcal{G}^k, \quad (2.1.1)$$

$$\mathcal{G}^k = \{E|\mathbf{0}\}\mathbb{T} + \{M_z|\frac{\hat{x}}{2} + \frac{\hat{z}}{2}\}\mathbb{T} + \{M_x|\frac{\hat{z}}{2}\}\mathbb{T} + \{C_{2y}|\frac{\hat{x}}{2}\}\mathbb{T}, \quad (2.1.2)$$

where $\mathfrak{T} = \{TI|\frac{\hat{x}}{2} + \frac{\hat{y}}{2} + \frac{\hat{z}}{2}\}$. The fourfold degeneracy is proven from algebra, $(\{C_{2y}|\frac{\hat{x}}{2}\})^2 = -1$, $\{\{C_{2y}|\frac{\hat{x}}{2}\}, \{M_x|\frac{\hat{z}}{2}\}\} = 0$, and $\{\{C_{2y}|\frac{\hat{x}}{2}\}, \mathfrak{T}\} = 0$ [13, 224, 225]. Because of the rotation symmetry $\{C_{2y}|\frac{\hat{x}}{2}\}$, the normal part Hamiltonian on the U - R line is block diagonalized and decomposed into the $\pm i$ subsectors. The \mathfrak{T} symmetry is preserved in each subsector as ensured by the anticommutation relation between $\{C_{2y}|\frac{\hat{x}}{2}\}$ and \mathfrak{T} . Thus, Kramers pairs are formed in each subsector. The anticommutation relation between $\{C_{2y}|\frac{\hat{x}}{2}\}$ and $\{M_x|\frac{\hat{z}}{2}\}$ ensures that a Kramers pair in the i subsector is degenerate with another Kramers pair in the $-i$ subsector. Thus, the fourfold degeneracy is protected by symmetry.

On the other lines, the fourfold degeneracy is proved in a similar way. On the R - T and Y - S lines, we use the relations, $(\{C_{2x}|\frac{\hat{z}}{2}\})^2 = -1$, $\{\{C_{2x}|\frac{\hat{z}}{2}\}, \{M_y|\frac{\hat{x}}{2}\}\} = 0$, and $\{\{C_{2x}|\frac{\hat{z}}{2}\}, \mathfrak{T}\} = 0$. Finally on the T - Y line, the fourfold degeneracy is proved by the relations, $(\{M_y|\frac{\hat{x}}{2}\})^2 = -1$, $\{\{M_y|\frac{\hat{x}}{2}\}, \{C_{2z}|\frac{\hat{x}}{2} + \frac{\hat{z}}{2}\}\} = 0$, and $\{\{M_y|\frac{\hat{x}}{2}\}, \mathfrak{T}\} = 0$.

B.2 Effective orbital angular momentum due to site permutation

In Sec. B.2, we introduced the effective orbital angular momentum λ_z due to the permutation of uranium sites. Here, we provide a general formulation for this angular momentum considering the transformation of the Bloch state wave function. First, we introduce a creation operator of a Bloch state in a sublattice-based representation denoted by $c_{m\zeta}^\dagger(\mathbf{k})$, where m and $\zeta = l_z + s_z$ are the indices of the sublattice and angular momentum, respectively. Fourier transformation of the Bloch state is defined as

$$c_{m\zeta}^\dagger(\mathbf{k}) = \sum_{\mathbf{R}} e^{-i\mathbf{k}\cdot\mathbf{R}} c_\zeta^\dagger(\mathbf{R} + \mathbf{r}_m), \quad (2.2.1)$$

where \mathbf{R} represents the position for the unit cell (lattice vector) and \mathbf{r}_m is the relative position of the m sublattice in a unit cell. Using this equation, the creation operator is transformed by a space group operation $g = \{p|\mathbf{a}\}$ as

$$\begin{aligned} gc_{m\zeta}^\dagger(\mathbf{k})g^{-1} &= \sum_{\mathbf{R}} e^{-i\mathbf{k}\cdot\mathbf{R}} gc_\zeta^\dagger(\mathbf{R} + \mathbf{r}_m)g^{-1} \\ &= \sum_{\mathbf{R}} e^{-i\mathbf{k}\cdot\mathbf{R}} \sum_{\zeta'} c_{\zeta'}^\dagger(p(\mathbf{R} + \mathbf{r}_m) + \mathbf{a}) D_{\zeta'\zeta}^{(\tilde{j})}(p). \end{aligned}$$

Defining $\mathbf{R}' + \mathbf{r}_{pm} \equiv p(\mathbf{R} + \mathbf{r}_m) + \mathbf{a}$, we have

$$\begin{aligned} &= \sum_{\mathbf{R}'} e^{-i\mathbf{k}\cdot[p^{-1}(\mathbf{R}' + \mathbf{r}_{pm} - \mathbf{a} - p\mathbf{r}_m)]} \sum_{\zeta'} c_{\zeta'}^\dagger(\mathbf{R}' + \mathbf{r}_{pm}) D_{\zeta'\zeta}^{(\tilde{j})}(p) \\ &= e^{ip\mathbf{k}\cdot\mathbf{a}} \sum_{\zeta'} \left(\sum_{\mathbf{R}'} e^{-ip\mathbf{k}\cdot\mathbf{R}'} c_{\zeta'}^\dagger(\mathbf{R}' + \mathbf{r}_{pm}) \right) e^{-ip\mathbf{k}\cdot(\mathbf{r}_{pm} - p\mathbf{r}_m)} D_{\zeta'\zeta}^{(\tilde{j})}(p) \\ &= e^{ip\mathbf{k}\cdot\mathbf{a}} \sum_{\zeta'} c_{pm,\zeta'}^\dagger(p\mathbf{k}) e^{-ip\mathbf{k}\cdot(\mathbf{r}_{pm} - p\mathbf{r}_m)} D_{\zeta'\zeta}^{(\tilde{j})}(p) \\ &= e^{ip\mathbf{k}\cdot\mathbf{a}} \sum_{m'} \sum_{\zeta'} c_{m'\zeta'}^\dagger(p\mathbf{k}) [D_{(\text{perm})}(p, \mathbf{k})]_{m'm} D_{\zeta'\zeta}^{(\tilde{j})}(p), \end{aligned} \quad (2.2.2)$$

where $D^{(\tilde{j})}(p)$ is a representation matrix of p in $\tilde{j} = l + s$ space. From Eq. (2.2.2), we define a representation matrix indicating the permutation of sites as

$$[D_{(\text{perm})}(p, \mathbf{k})]_{m'm} = e^{-ip\mathbf{k}\cdot(\mathbf{r}_{pm} - p\mathbf{r}_m)} \delta_{m', pm}. \quad (2.2.3)$$

The phase factor in this matrix corresponds to the effective orbital angular momentum λ_z . For example, a threefold rotation in UPt_3 is represented by

$$D_{(\text{perm})}(C_3, \mathbf{k}) = \begin{pmatrix} a & b \\ b & a \end{pmatrix} \begin{pmatrix} e^{+i2\pi/3} & 0 \\ 0 & e^{-i2\pi/3} \end{pmatrix}, \quad (2.2.4)$$

on the K point $\mathbf{k} = (4\pi/3, 0, 0)$. This phase factor gives the effective angular momentum $\lambda_z = \pm 1$ as we demonstrated in Sec. 4.3.4.

Bibliography

- [1] G. E. Volovik and L. P. Gor'kov, Pis'ma Zh. Eksp. Teor. Fiz. **39**, 550 (1984).
- [2] G. E. Volovik and L. P. Gor'kov, Zh. Eksp. Teor. Fiz. **88**, 1412 (1985).
- [3] P. W. Anderson, Phys. Rev. B **30**, 4000 (1984).
- [4] M. Sigrist and K. Ueda, Rev. Mod. Phys. **63**, 239 (1991).
- [5] V. G. Yarzhemsky and E. N. Murav'ev, J. Phys.: Condens. Matter **4**, 3525 (1992).
- [6] M. R. Norman, Phys. Rev. B **52**, 15093 (1995).
- [7] V. G. Yarzhemsky, Phys. Status Solidi B **209**, 101 (1998).
- [8] V. G. Yarzhemsky, Int. J. Quant. Chem. **80**, 133 (2000).
- [9] V. G. Yarzhemsky, AIP Conf. Proc. **678**, 343 (2003).
- [10] V. G. Yarzhemsky, J. Opt. Adv. Mater. **10**, 1759 (2008).
- [11] T. Micklitz and M. R. Norman, Phys. Rev. B **80**, 100506(R) (2009).
- [12] S. Kobayashi, Y. Yanase, and M. Sato, Phys. Rev. B **94**, 134512 (2016).
- [13] Y. Yanase, Phys. Rev. B **94**, 174502 (2016).
- [14] T. Nomoto and H. Ikeda, Phys. Rev. Lett. **117**, 217002 (2016).
- [15] T. Micklitz and M. R. Norman, Phys. Rev. B **95**, 024508 (2017).
- [16] T. Nomoto and H. Ikeda, J. Phys. Soc. Jpn. **86**, 023703 (2017).
- [17] T. Micklitz and M. R. Norman, Phys. Rev. Lett. **118**, 207001 (2017).
- [18] S. Sumita, T. Nomoto, and Y. Yanase, Phys. Rev. Lett. **119**, 027001 (2017).
- [19] S. Kobayashi, S. Sumita, Y. Yanase, and M. Sato, Phys. Rev. B **97**, 180504(R) (2018).

- [20] S. Sumita and Y. Yanase, Phys. Rev. B **97**, 134512 (2018).
- [21] S. Sumita, T. Nomoto, K. Shiozaki, and Y. Yanase, Phys. Rev. B **99**, 134513 (2019).
- [22] J. Bardeen, L. N. Cooper, and J. R. Schrieffer, Phys. Rev. **108**, 1175 (1957).
- [23] P. Fulde and R. A. Ferrell, Phys. Rev. **135**, A550 (1964).
- [24] A. I. Larkin and Y. N. Ovchinnikov, Zh. Eksp. Teor. Fiz. **47**, 1136 (1964), [Sov. Phys. JETP **20**, 762 (1965)].
- [25] Y. Matsuda and H. Shimahara, J. Phys. Soc. Jpn. **76**, 051005 (2007).
- [26] Phys. Rep. **387**, 1 (2003).
- [27] Y. Matsuda, K. Izawa, and I. Vekhter, J. Phys.: Condens. Matter **18**, R705 (2006).
- [28] T. Sakakibara, S. Kittaka, and K. Machida, Rep. Prog. Phys. **79**, 094002 (2016).
- [29] T. Nomoto, K. Hattori, and H. Ikeda, Phys. Rev. B **94**, 174513 (2016).
- [30] P. M. R. Brydon, L. Wang, M. Weinert, and D. F. Agterberg, Phys. Rev. Lett. **116**, 177001 (2016).
- [31] D. F. Agterberg, P. M. R. Brydon, and C. Timm, Phys. Rev. Lett. **118**, 127001 (2017).
- [32] C. Timm, A. P. Schnyder, D. F. Agterberg, and P. M. R. Brydon, Phys. Rev. B **96**, 094526 (2017).
- [33] L. Savary, J. Ruhman, J. W. F. Venderbos, L. Fu, and P. A. Lee, Phys. Rev. B **96**, 214514 (2017).
- [34] I. Boettcher and I. F. Herbut, Phys. Rev. Lett. **120**, 057002 (2018).
- [35] H. Kim, K. Wang, Y. Nakajima, R. Hu, S. Ziemak, P. Syers, L. Wang, H. Hodovanets, J. D. Denlinger, P. M. R. Brydon, D. F. Agterberg, M. A. Tanatar, R. Prozorov, and J. Paglione, Sci. Adv. .
- [36] J. W. F. Venderbos, L. Savary, J. Ruhman, P. A. Lee, and L. Fu, Phys. Rev. X **8**, 011029 (2018).
- [37] L. D. Landau and E. M. Lifshitz, *Statistical Physics Part 1*, 3rd ed., Course of Theoretical Physics, Vol. 5 (Elsevier, Oxford, 2013).
- [38] T. Inui, Y. Tanabe, and Y. Onodera, *Group theory and its applications in physics*, Springer Series in Solid-State Sciences, Vol. 78 (Springer-Verlag Berlin Heidelberg, Berlin, Heidelberg, 1990).

- [39] K. Izawa, H. Yamaguchi, Y. Matsuda, H. Shishido, R. Settai, and Y. Onuki, Phys. Rev. Lett. **87**, 057002 (2001).
- [40] K. Izawa, H. Yamaguchi, Y. Matsuda, T. Sasaki, R. Settai, and Y. Onuki, J. Phys. Chem. Solids **63**, 1055 (2002).
- [41] E. I. Blount, Phys. Rev. B **32**, 2935 (1985).
- [42] S. Fujimoto, J. Phys. Soc. Jpn. **75**, 083704 (2006).
- [43] Y. Wan and Q.-H. Wang, Europhys. Lett. **85**, 57007 (2009).
- [44] C. J. Bradley and B. L. Davies, Rev. Mod. Phys. **40**, 359 (1968).
- [45] C. J. Bradley and A. P. Cracknell, *The Mathematical Theory of Symmetry in Solids* (Oxford University Press, Oxford, 1972).
- [46] E. P. Wigner, *Group Theory and its Application to the Quantum Mechanics of Atomic Spectra* (Academic Press, New York, 1959).
- [47] C. Herring, Phys. Rev. **52**, 361 (1937).
- [48] K. Shiozaki, M. Sato, and K. Gomi, arXiv:1802.06694 .
- [49] C. J. Bradley and B. L. Davies, J. Math. Phys. **11**, 1536 (1970).
- [50] G. W. Mackey, Am. J. Math. **75**, 387 (1953).
- [51] Y. Izyumov, V. Laptev, and V. Syromyatnikov, Int. J. Mod. Phys. B **3**, 1377 (1989).
- [52] M. R. Zirnbauer, J. Math. Phys. **37**, 4986 (1996).
- [53] A. Altland and M. R. Zirnbauer, Phys. Rev. B **55**, 1142 (1997).
- [54] P. Ghosh, J. D. Sau, S. Tewari, and S. Das Sarma, Phys. Rev. B **82**, 184525 (2010).
- [55] S. Kobayashi, K. Shiozaki, Y. Tanaka, and M. Sato, Phys. Rev. B **90**, 024516 (2014).
- [56] Y. X. Zhao, A. P. Schnyder, and Z. D. Wang, Phys. Rev. Lett. **116**, 156402 (2016).
- [57] T. Bzdušek and M. Sigrist, Phys. Rev. B **96**, 155105 (2017).
- [58] A. P. Schnyder, S. Ryu, A. Furusaki, and A. W. W. Ludwig, Phys. Rev. B **78**, 195125 (2008).
- [59] A. P. Schnyder, S. Ryu, A. Furusaki, and A. W. W. Ludwig, AIP Conf. Procc **1134**, 10 (2009).
- [60] A. Kitaev, AIP Conf. Proc. **1134**, 22 (2009).

- [61] S. Ryu, A. P. Schnyder, A. Furusaki, and A. W. W. Ludwig, New J. Phys. **12**, 065010 (2010).
- [62] C.-K. Chiu, H. Yao, and S. Ryu, Phys. Rev. B **88**, 075142 (2013).
- [63] T. Morimoto and A. Furusaki, Phys. Rev. B **88**, 125129 (2013).
- [64] S. Ryu and Y. Hatsugai, Phys. Rev. Lett. **89**, 077002 (2002).
- [65] M. Sato, Y. Tanaka, K. Yada, and T. Yokoyama, Phys. Rev. B **83**, 224511 (2011).
- [66] Y. Tanaka, Y. Mizuno, T. Yokoyama, K. Yada, and M. Sato, Phys. Rev. Lett. **105**, 097002 (2010).
- [67] Y. Tanaka, M. Sato, and N. Nagaosa, J. Phys. Soc. Jpn. **81**, 011013 (2012).
- [68] R. S. K. Mong, A. M. Essin, and J. E. Moore, Phys. Rev. B **81**, 245209 (2010).
- [69] A. M. Turner, Y. Zhang, R. S. K. Mong, and A. Vishwanath, Phys. Rev. B **85**, 165120 (2012).
- [70] A. M. Essin and V. Gurarie, Phys. Rev. B **85**, 195116 (2012).
- [71] S. Miyakoshi and Y. Ohta, Phys. Rev. B **87**, 195133 (2013).
- [72] T. Yoshida, R. Peters, S. Fujimoto, and N. Kawakami, Phys. Rev. B **87**, 085134 (2013).
- [73] P. Baireuther, J. M. Edge, I. C. Fulga, C. W. J. Beenakker, and J. Tworzydło, Phys. Rev. B **89**, 035410 (2014).
- [74] R.-X. Zhang and C.-X. Liu, Phys. Rev. B **91**, 115317 (2015).
- [75] F. Bègue, P. Pujol, and R. Ramazashvili, Phys. Lett. A **381**, 1268 (2017).
- [76] P. M. R. Brydon, A. P. Schnyder, and C. Timm, Phys. Rev. B **84**, 020501 (2011).
- [77] K. Yada, M. Sato, Y. Tanaka, and T. Yokoyama, Phys. Rev. B **83**, 064505 (2011).
- [78] A. P. Schnyder, P. M. R. Brydon, and C. Timm, Phys. Rev. B **85**, 024522 (2012).
- [79] B. J. Kim, H. Jin, S. J. Moon, J.-Y. Kim, B.-G. Park, C. S. Leem, J. Yu, T. W. Noh, C. Kim, S.-J. Oh, J.-H. Park, V. Durairaj, G. Cao, and E. Rotenberg, Phys. Rev. Lett. **101**, 076402 (2008).
- [80] Y. K. Kim, O. Krupin, J. D. Denlinger, A. Bostwick, E. Rotenberg, Q. Zhao, J. F. Mitchell, J. W. Allen, and B. J. Kim, Science **345**, 187 (2014).
- [81] Y. J. Yan, M. Q. Ren, H. C. Xu, B. P. Xie, R. Tao, H. Y. Choi, N. Lee, Y. J. Choi, T. Zhang, and D. L. Feng, Phys. Rev. X **5**, 041018 (2015).

- [82] I. Battisti, K. M. Bastiaans, V. Fedoseev, A. d. l. Torre, N. Iliopoulos, A. Tamai, E. C. Hunter, R. S. Perry, J. Zaanen, F. Baumberger, and M. P. Allan, Nat. Phys. **13**, 21 (2017).
- [83] Y. K. Kim, N. H. Sung, J. D. Denlinger, and B. J. Kim, Nat. Phys. **12**, 37 (2016).
- [84] F. Wang and T. Senthil, Phys. Rev. Lett. **106**, 136402 (2011).
- [85] H. Watanabe, T. Shirakawa, and S. Yunoki, Phys. Rev. Lett. **110**, 027002 (2013).
- [86] Y. Yang, W.-S. Wang, J.-G. Liu, H. Chen, J.-H. Dai, and Q.-H. Wang, Phys. Rev. B **89**, 094518 (2014).
- [87] Z. Y. Meng, Y. B. Kim, and H.-Y. Kee, Phys. Rev. Lett. **113**, 177003 (2014).
- [88] B. J. Kim, H. Ohsumi, T. Komesu, S. Sakai, T. Morita, H. Takagi, and T. Arima, Science **323**, 1329 (2009).
- [89] S. Boseggia, H. C. Walker, J. Vale, R. Springell, Z. Feng, R. S. Perry, M. M. Sala, H. M. Rønnow, S. P. Collins, and D. F. McMorrow, J. Phys. Condens. Matter **25**, 422202 (2013).
- [90] J. P. Clancy, A. Lupascu, H. Gretarsson, Z. Islam, Y. F. Hu, D. Casa, C. S. Nelson, S. C. LaMarra, G. Cao, and Y.-J. Kim, Phys. Rev. B **89**, 054409 (2014).
- [91] C. Dhital, T. Hogan, Z. Yamani, C. de la Cruz, X. Chen, S. Khadka, Z. Ren, and S. D. Wilson, Phys. Rev. B **87**, 144405 (2013).
- [92] F. Ye, X. Wang, C. Hoffmann, J. Wang, S. Chi, M. Matsuda, B. C. Chakoumakos, J. A. Fernandez-Baca, and G. Cao, Phys. Rev. B **92**, 201112 (2015).
- [93] L. Zhao, D. H. Torchinsky, H. Chu, V. Ivanov, R. Lifshitz, R. Flint, T. Qi, G. Cao, and D. Hsieh, Nat. Phys. **12**, 32 (2016).
- [94] S. Di Matteo and M. R. Norman, Phys. Rev. B **94**, 075148 (2016).
- [95] Q. Huang, J. Soubeyroux, O. Chmaissem, I. N. Sora, A. Santoro, R. J. Cava, J. J. Krajewski, and W. F. Peck Jr., J. Solid State Chem. **112**, 355 (1994).
- [96] M. K. Crawford, M. A. Subramanian, R. L. Harlow, J. A. Fernandez-Baca, Z. R. Wang, and D. C. Johnston, Phys. Rev. B **49**, 9198 (1994).
- [97] N. A. Spaldin, M. Fiebig, and M. Mostovoy, J. Phys. Condens. Matter **20**, 434203 (2008).
- [98] Y. Yanase, J. Phys. Soc. Jpn. **83**, 014703 (2014).
- [99] T. Hitomi and Y. Yanase, J. Phys. Soc. Jpn. **83**, 114704 (2014).

- [100] S. Hayami, H. Kusunose, and Y. Motome, Phys. Rev. B **90**, 024432 (2014).
- [101] S. Hayami, H. Kusunose, and Y. Motome, Phys. Rev. B **90**, 081115 (2014).
- [102] S. Hayami, H. Kusunose, and Y. Motome, J. Phys. Soc. Jpn. **84**, 064717 (2015).
- [103] L. Fu, Phys. Rev. Lett. **115**, 026401 (2015).
- [104] T. Hitomi and Y. Yanase, J. Phys. Soc. Jpn. **85**, 124702 (2016).
- [105] Y. Kuramoto, H. Kusunose, and A. Kiss, J. Phys. Soc. Jpn. **78**, 072001 (2009).
- [106] C. Schwartz, Phys. Rev. **97**, 380 (1955).
- [107] Z. Zhong, A. Tóth, and K. Held, Phys. Rev. B **87**, 161102 (2013).
- [108] Y. Yanase, J. Phys. Soc. Jpn. **82**, 044711 (2013).
- [109] G. Herzberg, *Molecular Spectra and Molecular Structure*, Vol. 3 (Van Nostrand, New York, 1966).
- [110] T. Yoshida, A. Daido, N. Kawakami, and Y. Yanase, Phys. Rev. B **99**, 235105 (2019).
- [111] Bilbao Crystallographic Server, Point Group Tables, <http://www.cryst.ehu.es/rep/point>.
- [112] P. M. R. Brydon, D. F. Agterberg, H. Menke, and C. Timm, Phys. Rev. B **98**, 224509 (2018).
- [113] G. R. Stewart, Z. Fisk, J. O. Willis, and J. L. Smith, Phys. Rev. Lett. **52**, 679 (1984).
- [114] R. A. Fisher, S. Kim, B. F. Woodfield, N. E. Phillips, L. Taillefer, K. Hasselbach, J. Flouquet, A. L. Giorgi, and J. L. Smith, Phys. Rev. Lett. **62**, 1411 (1989).
- [115] G. Bruls, D. Weber, B. Wolf, P. Thalmeier, B. Lüthi, A. de Visser, and A. Menovsky, Phys. Rev. Lett. **65**, 2294 (1990).
- [116] S. Adenwalla, S. W. Lin, Q. Z. Ran, Z. Zhao, J. B. Ketterson, J. A. Sauls, L. Taillefer, D. G. Hinks, M. Levy, and B. K. Sarma, Phys. Rev. Lett. **65**, 2298 (1990).
- [117] H. Tou, Y. Kitaoka, K. Ishida, K. Asayama, N. Kimura, Y. Ōnuki, E. Yamamoto, Y. Haga, and K. Maezawa, Phys. Rev. Lett. **80**, 3129 (1998).
- [118] J. A. Sauls, Advances in Physics **43**, 113 (1994).
- [119] R. Joynt and L. Taillefer, Rev. Mod. Phys. **74**, 235 (2002).

- [120] J. D. Strand, D. J. Bahr, D. J. Van Harlingen, J. P. Davis, W. J. Gannon, and W. P. Halperin, *Science* **328**, 1368 (2010).
- [121] G. M. Luke, A. Keren, L. P. Le, W. D. Wu, Y. J. Uemura, D. A. Bonn, L. Taillefer, and J. D. Garrett, *Phys. Rev. Lett.* **71**, 1466 (1993).
- [122] E. R. Schemm, W. J. Gannon, C. M. Wishne, W. P. Halperin, and A. Kapitulnik, *Science* **345**, 190 (2014).
- [123] Y. Yanase and K. Shiozaki, *Phys. Rev. B* **95**, 224514 (2017).
- [124] D. A. Walko, J.-I. Hong, T. V. Chandrasekhar Rao, Z. Wawrzak, D. N. Seidman, W. P. Halperin, and M. J. Bedzyk, *Phys. Rev. B* **63**, 054522 (2001).
- [125] L. Taillefer and G. G. Lonzarich, *Phys. Rev. Lett.* **60**, 1570 (1988).
- [126] M. R. Norman, R. C. Albers, A. M. Boring, and N. E. Christensen, *Solid State Communications* **68**, 245 (1988).
- [127] N. Kimura, R. Settai, Y. Ōnuki, H. Toshima, E. Yamamoto, K. Maezawa, H. Aoki, and H. Harima, *J. Phys. Soc. Jpn.* **64**, 3881 (1995).
- [128] G. J. McMullan, P. M. C. Rourke, M. R. Norman, A. D. Huxley, N. Doiron-Leyraud, J. Flouquet, G. G. Lonzarich, A. McCollam, and S. R. Julian, *New Journal of Physics* **10**, 053029 (2008).
- [129] C. L. Kane and E. J. Mele, *Phys. Rev. Lett.* **95**, 226801 (2005).
- [130] Y. Saito, Y. Nakamura, M. S. Bahramy, Y. Kohama, J. Ye, Y. Kasahara, Y. Nakagawa, M. Onga, M. Tokunaga, T. Nojima, Y. Yanase, and Y. Iwasa, *Nat. Phys.* **12**, 144 (2016).
- [131] M. H. Fischer, F. Loder, and M. Sigrist, *Phys. Rev. B* **84**, 184533 (2011).
- [132] D. Maruyama, M. Sigrist, and Y. Yanase, *J. Phys. Soc. Jpn.* **81**, 034702 (2012).
- [133] R. Akashi, M. Ochi, S. Bordács, R. Suzuki, Y. Tokura, Y. Iwasa, and R. Arita, *Phys. Rev. Applied* **4**, 014002 (2015).
- [134] R. Akashi, Y. Iida, K. Yamamoto, and K. Yoshizawa, *Phys. Rev. B* **95**, 245401 (2017).
- [135] Z. Wang, J. Berlinsky, G. Zwicknagl, and C. Kallin, *Phys. Rev. B* **96**, 174511 (2017).
- [136] C. Triola and A. M. Black-Schaffer, *Phys. Rev. B* **97**, 064505 (2018).
- [137] G. Aeppli, E. Bucher, C. Broholm, J. K. Kjems, J. Baumann, and J. Hufnagl, *Phys. Rev. Lett.* **60**, 615 (1988).

- [138] S. M. Hayden, L. Taillefer, C. Vettier, and J. Flouquet, Phys. Rev. B **46**, 8675 (1992).
- [139] J. Ishizuka, S. Sumita, and Y. Yanase, in preparation.
- [140] D. J. Thouless, M. Kohmoto, M. P. Nightingale, and M. den Nijs, Phys. Rev. Lett. **49**, 405 (1982).
- [141] M. Kohmoto, Ann. Phys. (NY) **160**, 405 (1985).
- [142] T. Fukui, Y. Hatsugai, and H. Suzuki, J. Phys. Soc. Jpn. **74**, 1674 (2005).
- [143] H. Sumiyoshi and S. Fujimoto, J. Phys. Soc. Jpn. **82**, 023602 (2013).
- [144] I. R. Shein and A. L. Ivanovskii, Physica C **471**, 594 (2011).
- [145] S. J. Youn, M. H. Fischer, S. H. Rhim, M. Sigrist, and D. F. Agterberg, Phys. Rev. B **85**, 220505(R) (2012).
- [146] S. J. Youn, S. H. Rhim, D. F. Agterberg, M. Weinert, and A. J. Freeman, arXiv:1202.1604 .
- [147] P. K. Biswas, H. Luetkens, T. Neupert, T. Stürzer, C. Baines, G. Pascua, A. P. Schnyder, M. H. Fischer, J. Goryo, M. R. Lees, H. Maeter, F. Brückner, H.-H. Klauss, M. Nicklas, P. J. Baker, A. D. Hillier, M. Sigrist, A. Amato, and D. Johrendt, Phys. Rev. B **87**, 180503(R) (2013).
- [148] K. Matano, K. Arima, S. Maeda, Y. Nishikubo, K. Kudo, M. Nohara, and G.-q. Zheng, Phys. Rev. B **89**, 140504(R) (2014).
- [149] J. Goryo, M. H. Fischer, and M. Sigrist, Phys. Rev. B **86**, 100507(R) (2012).
- [150] M. H. Fischer, T. Neupert, C. Platt, A. P. Schnyder, W. Hanke, J. Goryo, R. Thomale, and M. Sigrist, Phys. Rev. B **89**, 020509(R) (2014).
- [151] M. H. Fischer and J. Goryo, J. Phys. Soc. Jpn. **84**, 054705 (2015).
- [152] W.-S. Wang, Y. Yang, and Q.-H. Wang, Phys. Rev. B **90**, 094514 (2014).
- [153] F. Brückner, R. Sarkar, M. Günther, H. Kühne, H. Luetkens, T. Neupert, A. P. Reyes, P. L. Kuhns, P. K. Biswas, T. Stürzer, D. Johrendt, and H.-H. Klauss, Phys. Rev. B **90**, 220503(R) (2014).
- [154] A. Koitzsch, I. Opahle, S. Elgazzar, S. V. Borisenko, J. Geck, V. B. Zabolotnyy, D. Inosov, H. Shiozawa, M. Richter, M. Knupfer, J. Fink, B. Büchner, E. D. Bauer, J. L. Sarrao, and R. Follath, Phys. Rev. B **79**, 075104 (2009).

- [155] A. Koitzsch, T. K. Kim, U. Treske, M. Knupfer, B. Büchner, M. Richter, I. Opahle, R. Follath, E. D. Bauer, and J. L. Sarrao, Phys. Rev. B **88**, 035124 (2013).
- [156] D. Hall, E. C. Palm, T. P. Murphy, S. W. Tozer, Z. Fisk, U. Alver, R. G. Goodrich, J. L. Sarrao, P. G. Pagliuso, and T. Ebihara, Phys. Rev. B **64**, 212508 (2001).
- [157] R. Settai, H. Shishido, S. Ikeda, Y. Murakawa, M. Nakashima, D. Aoki, Y. Haga, H. Harima, and Y. Onuki, J. Phys.: Condens. Matter **13**, L627 (2001).
- [158] H. Shishido, R. Settai, D. Aoki, S. Ikeda, H. Nakawaki, N. Nakamura, T. Iizuka, Y. Inada, K. Sugiyama, T. Takeuchi, K. Kindo, T. C. Kobayashi, Y. Haga, H. Harima, Y. Aoki, T. Namiki, H. Sato, and Y. Ōnuki, J. Phys. Soc. Jpn. **71**, 162 (2002).
- [159] S. Elgazzar, I. Opahle, R. Hayn, and P. M. Oppeneer, Phys. Rev. B **69**, 214510 (2004).
- [160] H. C. Choi, B. I. Min, J. H. Shim, K. Haule, and G. Kotliar, Phys. Rev. Lett. **108**, 016402 (2012).
- [161] T. Nomoto and H. Ikeda, Phys. Rev. B **90**, 125147 (2014).
- [162] C. Petrovic, P. G. Pagliuso, M. F. Hundley, R. Movshovich, J. L. Sarrao, J. D. Thompson, Z. Fisk, and P. Monthoux, J. Phys.: Condens. Matter **13**, L337 (2001).
- [163] R. Movshovich, M. Jaime, J. D. Thompson, C. Petrovic, Z. Fisk, P. G. Pagliuso, and J. L. Sarrao, Phys. Rev. Lett. **86**, 5152 (2001).
- [164] Y. Kohori, Y. Yamato, Y. Iwamoto, T. Kohara, E. D. Bauer, M. B. Maple, and J. L. Sarrao, Phys. Rev. B **64**, 134526 (2001).
- [165] A. Akbari, P. Thalmeier, and I. Eremin, Phys. Rev. B **84**, 134505 (2011).
- [166] M. P. Allan, F. Massee, D. K. Morr, J. Van Dyke, A. W. Rost, A. P. Mackenzie, C. Petrovic, and J. C. Davis, Nat. Phys. **9**, 468 (2013).
- [167] B. B. Zhou, S. Misra, E. H. da Silva Neto, P. Aynajian, R. E. Baumbach, J. D. Thompson, E. D. Bauer, and A. Yazdani, Nat. Phys. **9**, 474 (2013).
- [168] K. An, T. Sakakibara, R. Settai, Y. Onuki, M. Hiragi, M. Ichioka, and K. Machida, Phys. Rev. Lett. **104**, 037002 (2010).
- [169] H. Xiao, T. Hu, C. C. Almasan, T. A. Sayles, and M. B. Maple, Phys. Rev. B **78**, 014510 (2008).
- [170] F. Canepa, P. Manfrinetti, M. Pani, and A. Palenzona, J. Alloys Compd. **234**, 225 (1996).

- [171] N. T. Huy, A. Gasparini, D. E. de Nijs, Y. Huang, J. C. P. Klaasse, T. Gortenmulder, A. de Visser, A. Hamann, T. Görlach, and H. v. Löhneysen, Phys. Rev. Lett. **99**, 067006 (2007).
- [172] D. Aoki and J. Flouquet, J. Phys. Soc. Jpn. **83**, 061011 (2014).
- [173] E. Hassinger, D. Aoki, G. Knebel, and J. Flouquet, J. Phys. Soc. Jpn. **77**, 073703 (2008).
- [174] E. Slooten, T. Naka, A. Gasparini, Y. K. Huang, and A. de Visser, Phys. Rev. Lett. **103**, 097003 (2009).
- [175] G. Bastien, D. Braithwaite, D. Aoki, G. Knebel, and J. Flouquet, Phys. Rev. B **94**, 125110 (2016).
- [176] A. K. C. Cheung and S. Raghu, Phys. Rev. B **93**, 134516 (2016).
- [177] V. P. Mineev, Phys. Rev. B **95**, 104501 (2017).
- [178] M. Manago, K. Ishida, and D. Aoki, Phys. Rev. B **97**, 075130 (2018).
- [179] A. Daido, T. Yoshida, and Y. Yanase, Phys. Rev. Lett. **122**, 227001 (2019).
- [180] J. T. Ye, Y. J. Zhang, R. Akashi, M. S. Bahramy, R. Arita, and Y. Iwasa, Science **338**, 1193 (2012).
- [181] J. M. Lu, O. Zheliuk, I. Leermakers, N. F. Q. Yuan, U. Zeitler, K. T. Law, and J. T. Ye, Science **350**, 1353 (2015).
- [182] W. Shi, J. Ye, Y. Zhang, R. Suzuki, M. Yoshida, J. Miyazaki, N. Inoue, Y. Saito, and Y. Iwasa, Sci. Rep. **5**, 12534 (2015).
- [183] D. Costanzo, S. Jo, H. Berger, and A. F. Morpurgo, Nat. Nanotechnol. **11**, 339 (2016).
- [184] J. A. Woollam and R. B. Somoano, Materials Science and Engineering **31**, 289 (1977).
- [185] R. Zhang, I.-L. Tsai, J. Chapman, E. Khestanova, J. Waters, and I. V. Grigorieva, Nano Lett. **16**, 629 (2016).
- [186] G.-B. Liu, D. Xiao, Y. Yao, X. Xu, and W. Yao, Chem. Soc. Rev. **44**, 2643 (2015).
- [187] Y. Nakamura and Y. Yanase, Phys. Rev. B **96**, 054501 (2017).
- [188] Y. Ge and A. Y. Liu, Phys. Rev. B **87**, 241408 (2013).
- [189] M. Rösner, S. Haas, and T. O. Wehling, Phys. Rev. B **90**, 245105 (2014).
- [190] T. Das and K. Dolui, Phys. Rev. B **91**, 094510 (2015).

- [191] N. F. Q. Yuan, K. F. Mak, and K. T. Law, Phys. Rev. Lett. **113**, 097001 (2014).
- [192] Y.-T. Hsu, A. Vaezi, M. H. Fischer, and E.-A. Kim, Nat. Commun. **8**, 14985 (2017).
- [193] H. R. Ott, H. Rudigier, Z. Fisk, and J. L. Smith, Phys. Rev. Lett. **50**, 1595 (1983).
- [194] H. R. Ott, H. Rudigier, T. M. Rice, K. Ueda, Z. Fisk, and J. L. Smith, Phys. Rev. Lett. **52**, 1915 (1984).
- [195] D. E. MacLaughlin, C. Tien, W. G. Clark, M. D. Lan, Z. Fisk, J. L. Smith, and H. R. Ott, Phys. Rev. Lett. **53**, 1833 (1984).
- [196] Y. Shimizu, S. Kittaka, T. Sakakibara, Y. Haga, E. Yamamoto, H. Amitsuka, Y. Tsutsumi, and K. Machida, Phys. Rev. Lett. **114**, 147002 (2015).
- [197] J. L. Smith, Z. Fisk, J. O. Willis, A. L. Giorgi, R. B. Roof, H. R. Ott, H. Rudigier, and E. Felder, Physica B **135**, 3 (1985).
- [198] H. R. Ott, H. Rudigier, Z. Fisk, and J. L. Smith, Phys. Rev. B **31**, 1651 (1985).
- [199] R. H. Heffner, J. L. Smith, J. O. Willis, P. Birrer, C. Baines, F. N. Gygax, B. Hitti, E. Lippelt, H. R. Ott, A. Schenck, E. A. Knetsch, J. A. Mydosh, and D. E. MacLaughlin, Phys. Rev. Lett. **65**, 2816 (1990).
- [200] F. Kromer, R. Helfrich, M. Lang, F. Steglich, C. Langhammer, A. Bach, T. Michels, J. S. Kim, and G. R. Stewart, Phys. Rev. Lett. **81**, 4476 (1998).
- [201] K. Takegahara and H. Harima, Physica B **281-282**, 764 (2000).
- [202] T. Maehira, A. Higashiya, M. Higuchi, H. Yasuhara, and A. Hasegawa, Physica B **312-313**, 103 (2002).
- [203] Y. Shimizu, S. Kittaka, S. Nakamura, T. Sakakibara, D. Aoki, Y. Homma, A. Nakamura, and K. Machida, Phys. Rev. B **96**, 100505 (2017).
- [204] K. Machida, J. Phys. Soc. Jpn. **87**, 033703 (2018).
- [205] M. B. Maple, N. A. Frederick, P.-C. Ho, W. M. Yuhasz, and T. Yanagisawa, J. Supercond. Novel Magn. **19**, 299 (2006).
- [206] Y. Aoki, T. Tayama, T. Sakakibara, K. Kuwahara, K. Iwasa, M. Kohgi, W. Higemoto, D. E. MacLaughlin, H. Sugawara, and H. Sato, J. Phys. Soc. Jpn. **76**, 051006 (2007).
- [207] M. B. Maple, P.-C. Ho, V. S. Zapf, N. A. Frederick, E. D. Bauer, W. M. Yuhasz, F. M. Woodward, and J. W. Lynn, J. Phys. Soc. Jpn. **71**, 23 (2002).

- [208] R. Vollmer, A. Faißt, C. Pfleiderer, H. v. Löhneysen, E. D. Bauer, P.-C. Ho, V. Zapf, and M. B. Maple, Phys. Rev. Lett. **90**, 057001 (2003).
- [209] K. Izawa, Y. Nakajima, J. Goryo, Y. Matsuda, S. Osaki, H. Sugawara, H. Sato, P. Thalmeier, and K. Maki, Phys. Rev. Lett. **90**, 117001 (2003).
- [210] K. Katayama, S. Kawasaki, M. Nishiyama, H. Sugawara, D. Kikuchi, H. Sato, and G.-q. Zheng, J Phys. Soc. Jpn. **76**, 023701 (2007).
- [211] E. E. M. Chia, M. B. Salamon, H. Sugawara, and H. Sato, Phys. Rev. Lett. **91**, 247003 (2003).
- [212] G. Seyfarth, J. P. Brison, M.-A. Méasson, D. Braithwaite, G. Lapertot, and J. Flouquet, Phys. Rev. Lett. **97**, 236403 (2006).
- [213] D. E. MacLaughlin, J. E. Sonier, R. H. Heffner, O. O. Bernal, B.-L. Young, M. S. Rose, G. D. Morris, E. D. Bauer, T. D. Do, and M. B. Maple, Phys. Rev. Lett. **89**, 157001 (2002).
- [214] H. Kotegawa, M. Yogi, Y. Imamura, Y. Kawasaki, G.-q. Zheng, Y. Kitaoka, S. Ohsaki, H. Sugawara, Y. Aoki, and H. Sato, Phys. Rev. Lett. **90**, 027001 (2003).
- [215] Y. Aoki, A. Tsuchiya, T. Kanayama, S. R. Saha, H. Sugawara, H. Sato, W. Higemoto, A. Koda, K. Ohishi, K. Nishiyama, and R. Kadono, Phys. Rev. Lett. **91**, 067003 (2003).
- [216] E. M. Levenson-Falk, E. R. Schemm, M. B. Maple, and A. Kapitulnik, arXiv:1609.07535 .
- [217] H. Sugawara, S. Osaki, S. R. Saha, Y. Aoki, H. Sato, Y. Inada, H. Shishido, R. Settai, Y. Ōnuki, H. Harima, and K. Oikawa, Phys. Rev. B **66**, 220504 (2002).
- [218] I. A. Sergienko and S. H. Curnoe, Phys. Rev. B **70**, 144522 (2004).
- [219] K. Maki, H. Won, P. Thalmeier, Q. Yuan, K. Izawa, and Y. Matsuda, Europhys. Lett. **64**, 496 (2003).
- [220] K. Maki, S. Haas, D. Parker, H. Won, K. Izawa, and Y. Matsuda, Europhys. Lett. **68**, 720 (2004).
- [221] J. Goryo, Phys. Rev. B **67**, 184511 (2003).
- [222] K. Miyake, H. Kohno, and H. Harima, J. Phys.: Condens. Matter **15**, L275 (2003).
- [223] M. Ichioka, N. Nakai, and K. Machida, J. Phys. Soc. Jpn. **72**, 1322 (2003).
- [224] Q.-F. Liang, J. Zhou, R. Yu, Z. Wang, and H. Weng, Phys. Rev. B **93**, 085427 (2016).
- [225] S. Sumita and Y. Yanase, Phys. Rev. B **93**, 224507 (2016).

Acknowledgment

I would like to thank Youichi Yanase for his support during my master and doctor courses. I am deeply grateful to him for providing me many opportunities to discuss condensed matter physics, giving me plenty of advice on the direction of my study, and teaching me about desired attitude to establish good researches. Without his guidance, I could not have done this work.

I would like to thank Takuya Nomoto, Shingo Kobayashi, Masatoshi Sato, and Ken Shiozaki, for many fruitful and stimulating discussions through collaborations on the topics of gap classification theory. I also appreciate Manfred Sigrist in ETH Zurich and Mark H. Fischer in University of Zurich, for fruitful discussions and supporting me during staying in Zurich.

I would like to thank the faculty in Condensed Matter Theory Group at Kyoto University, Norio Kawakami, Ryusuke Ikeda, Robert Peters, and Masaki Tezuka, for their support in various academic matters as well as fruitful discussions. I also have greatly benefited from my colleagues in the Condensed Matter Theory Group for everyday discussions on physics and other topics. Especially, I am grateful to Akito Daido for a lot of stimulating discussions and drinking parties.

I appreciate financial support I have received over the past three years from the Japan Society for the Promotion of Science.

Lastly, I am deeply grateful to my parents Toru and Emiko, whose encouragement and advice have been a great source of support in learning not only physics but also many other things.